2011

Laser-based thermophysical properties measurement and nanotructure diagnostics

Xiangwen Chen
Iowa State University

Laser-based thermophysical properties measurement and nanotructure diagnostics

by

Xiangwen Chen

A dissertation submitted to the graduate faculty

in partial fulfillment of the requirements for the degree of

DOCTOR OF PHILOSOPHY

Major: Mechanical Engineering

Program of Study Committee:
Xinwei Wang, Major Professor
Qingze Zou
Song Zhang
Sriram Sundararajan
Zhi Jian Wang

Iowa State University

Ames, Iowa

2011

TABLE OF CONTENTS

LIST OF TABLES

LIST OF FIGURES

ACKNOWLEDGEMENTS

First of all, I would like to express my appreciation to my major advisor, Professor Xinwei Wang for giving me the opportunity to study and do research in his laboratory. His guidance, encouragement, support and inspiration are inevitable during my road of grow-up.

I also want to thank other professors: Song Zhang, Qingze Zou, Sriram Sundararajan, Palaniappa A. Molian, Zhi Jian Wang, for their insightful and professional comments and advice on my research work. Especially thanks to Dr. Zhi Jian Wang, a scholarly mentor and beneficial friend, always displays enthusiasm and give out sagacious ideas. That is inspiring.

I am grateful to Dr. Yuping He and Dr. Yiping Zhao, both from Department of Physics and Astronomy, and Nanoscale Science and Engineering Center, University of Georgia, for providing various testing samples as well as chemical analysis in my project.

Many more thanks goes to my lab-mates and office-mates Xiaopeng Huang, Xuhui Feng, Liying Guo, Sobieslaw Gacek, Guoqing Liu, Dr. Wei Yu, Dr. Jianmei Wang, Nathan Van Velson, Xiaoduan Tang, Jingchao Zhang, Lin Liu, Ruben Flesner for their support and friendship, especially Yanan Yue for discussing Raman measuring, and Yufeng Wu for his help in SEM image.

Last, but not least, I feel in depth indebted to my family especially my wife Wuji Hou for believing in me and unconditional consistent support to my study and research, this work also embodies their sweat.

ABSTRACT

This dissertation first presents the work on measuring thermal properties of MgH_2 nanostructures at microscale by using laser-based method — photothermal technique. In order to investigate the thermal properties at nanoscale, a scanning photothermal microscopy (SPTM) system is proposed. In the SPTM, the most important part is the complex tip-laser interaction. Systematical work has been done to in this field. For the first part, the photothermal technique is used to measure the effective thermal conductivity and density of the vanadium-doped MgH_2 nanostructures which is extensively used in energy storage applications. A multilayer physical model is used to fit the experimental data. Our results show that the effective thermal conductivity of the hydrogenated V-doped Mg nanostructures is in the range of 1.16 – 2.40 W/(m·K), and the density falls in the range of 878 – 1320 kg/m^3. The measured density agrees well with the estimation from electron micrograph observation. Variation in the measurements indicates strong non-uniformity of the sample structure and thickness. Based on the measured density and effective thermal conductivity, the thermal conductivity of bulk V-doped Mg hydrides is also evaluated using Maxwell's correlation.

For the second part, scanning photothermal microscopy (SPTM) system is designed to diagnose the defects on sub-surface under nanoscale range. This system consists of a conventional AFM and an external laser. Due to the complex interaction between the sharp tip and the laser, the thermal response of tungsten tip was first studied. At first step, we systematically report on a study of highly enhanced optical field and its induced thermal transport in nanotips under laser irradiation. Our Poynting vectors study clearly shows when

a laser interacts with a metal tip, it is bent around the tip and concentrated under the apex, where extremely high field enhancement appears. This phenomenon is more like a liquid flow being forced/squeezed to go through a narrow channel. How the geometry of the tip, the tip-substrate distance, polarization angle and incident angle of laser affect the field enhancement are systematically presented. The thermal transport inside the nanoscale tungsten tips due to absorption of incident laser is also explored. As the polarization angle or apex radius increases, the peak apex temperature decreases. The peak apex temperature goes down as the cone angle increases, even though the mean laser intensity inside the tip increases, revealing a very strong effect of the cone angle on thermal transport.

Correspondingly, experimental work on the laser-tip interaction was reported. The temperature rise of an ordinary AFM silicon tip under laser irradiation was measured. Laser heated AFM tip can act as both thermal probe and thermal heating source in nanoscale thermal heating process. The elevated temperature of the tip can be acquired from the relationship between Raman shift vs. temperature, which, however, is different compared to the Raman shift-temperature curve for bulk Si. The influences of focal position and energy flux level on the Raman shift have been discussed intensively. We substantiate our Raman measurement by theoretically modeling the electric field distribution as well as the heating processing through finite element method and a one-dimensional model, respectively.

CHAPTER 1. INTRODUCTION

In recent decades, laser technology has been used widely in non-destructive thermal properties measurements. The methods include pulse heating method [1], laser-heated transient electrothermal technique (TET) [2], steady-state electro-Raman-thermal (SERT) [3], photoacoustic methods [4,5], as well as the photothermal method [6-12] introduced in this work fall into this category. Photothermal techniques have been used extensively to investigate the thermal properties of materials. In this work a fast, non-destructive and non-contact photothermal technique is present. This technique is based on periodically time-dependent heating at a point on one surface, using, for example, modulated laser beam, and measuring the phase shift of the thermal wave compared to the excitation laser signal. It was successfully used by our group to measure the thermophysical properties of nanostructures, such as high aligned multiwall carbon nanotubes [13,14], TiO_2 nanotube arrays [15], and hybride organic-inorganic films [16]. Here, the nanostructure of magnesium hydride, MgH_2, which is a competitive form of energy storage (in terms of hydrogen), is investigated, and the density, thermal conductivity are also measured in a photothermal system.

The photothermal technique mainly measures thermal properties at microscale. Investigating the thermal properties at nanoscale is still a challenge. Since the invention of scanning probe microscope (SPM) technologies such as scanning tunneling microscopy (STM) and atomic force microscopy (AFM) in 1980's [17], their high resolution has brought the focus to nanoscale at relatively low cost. It also opened a window for the nanoscale thermal analysis. In recent decades, the interaction of a SPM tip with an external illuminating laser has

motivated considerable new exciting developments. The marriage of laser and SPM gave birth to the near-field scanning optical microscopy (NSOM/SNOM) [18-20] — a distinct imaging method based on near-field enhancement at coated, pulled capillaries has extended the optical microscopy technology beyond the diffraction limit that constrains the resolution no finer than ~ $l/2$ (l: light wavelength). Later, apertureless NSOM was realized [20-24]. Combined with the near-field technique, surface enhanced Raman scattering (SERS) [25-28] and tip enhanced Raman scattering (TERS) [29-32] prove promising and powerful tools for material analyzing at nanoscale. Despite the early TERS-related work [33-35], the term TERS came into use after 2000.

The use of laser-illuminated metal tips for near-field imaging has been studied by many groups [36-39]. Combined with infrared [40-42], the AFM can be used to measure thermal properties with the resolution as small as 50 nm, this technique, however, since the laser irradiates sample not the tip from the backside of the sample, it should has special requirements for substrate. Similarly, Scattering SNOM (s-SNOM) was introduced [43-46]. On the strength of the highly confined tip near-field which permits unltrahigh optical resolution less than 20 nm with visible and midinfrared illumination, the measurement of local elastic light scattering can access to the infrared fingerprint signature, and finally assign the chemical composition at nanoscale.

Akin to s-SNOM, a canning photothermal microscopy (SPTM) system to diagnose the thermal properties on sub-surface under nanoscale range is proposed in this work. The SPTM is also combination of external laser and SPM. A polarized lateral external laser is used to

illuminate the tip. The polarization component along the tip axis would induce a strong surface charge density at the tip end, giving rise to the field enhancement effect [37]. The enhanced electric field will heat up the substrate, and in turn induce thermal expansion. The surface expansion can be detected with AFM scanning mode. This technique is different from scanning thermal microscopy (SThM) [47-50], in which heat transfer rate between the tip and substrate is measured to assign thermal properties of the sample. Using modulated laser in the SPTM, the phase-shift signal which contains the information of thermal diffusivity can be extracted.

To study the SPTM, the complex interaction between a sharp tip and laser needs to be studied first. The temperature increase as well as thermal expansion was calculated theoretically; then the temperature rise in Si AFM tip was experimentally investigated. The temperature rise of Si substrate under a sharp tip illuminated by laser was also measured in our lab [51].

1.1 Energy Storage in MgH_2 Nanostructrures

Hydrogen is a promising alternative energy source for fossil fuel. The practical use of hydrogen depends largely on on-board storage techniques [52]. Storing hydrogen as compressed gas in pressurized vessels or in the form of liquid in cryogenic tanks is the usual approach, and it requires high energy consumption and needs high-level safety precautions [53,54]. Storing H_2 in solid state materials is the safest and most promising method [54]. In the pursuit of metal hydrides as solid state hydrogen storage media, magnesium hydride (MgH_2) is considered a good candidate due to its lightweight, low manufacturing cost, and

high theoretical hydrogen storage capacity (~7.66% by weight, and ~150 kg H_2/m^3 by volume) [55,56]. However, since the enthalpy of MgH_2 formation is very high (−76 kJ/mol H_2), it requires temperatures in excess of 573 K to decompose it into H_2 and bulk Mg [57]. Additionally, the kinetics of MgH_2 formation are slow [58,59]. To solve these two problems, it has been reported that doping Mg with a transition metal (catalyst) can weaken the Mg-H bond and reduce the stability of the hydride, thus promoting the hydrogenation/dehydrogenation performance of Mg [57,60-64]. Ball-milling is one of the primary methods to fabricate catalyst doped Mg structures. The hydrogen storage properties of ball milled nanocrystalline MgH_2 + 5 at.% Tm (Tm = Ti, V, Mn, Fe and Ni) were evaluated by Liang *et al.* [65]. Their results revealed that the composite containing Ti or V exhibited the most rapid desorption kinetics at a temperature above 523 K, and rapid absorption kinetics at temperatures as low as 302 K. Schulz *et al.* [66] reported that V and Ti were better catalysts than Ni for hydrogen absorption and desorption in transition metal doped-MgH_2. Pozzo and Alfe [57] investigated a wide range of transition metal dopants including Ti, Zr, V, Fe, Ru, Co, Rh, Ni, Pd, Cu and Ag. Their results showed that Ti, V, Zr together with Ru could eliminate the Mg-H dissociation barrier. Bobet *et al*. used chemical fluid deposition in supercritical fluids (SCF) to fabricate doped metal hydrides [67]. Besides keeping the same sorption properties as those fabricated by the ball-milling method, the materials fabricated by SCF had significantly improved cyclability. For ball-milling samples, the catalytic effect of metal decreased after 100 hydrogenation/dehydrogenation cycles, while for the SCF sample, it almost stayed constant [67]. Other fabrication methods for doped metal hydrides, including chemical fluid deposition in supercritical fluids (SCF) [67], sol-gel [68], ion implantation [69], ultrasound radiation [70], electrodeposition [71], chemical vapor

deposition [72], and hybrid growth techniques [73] have also been reported. Recently, we have successfully applied an oblique angle co-deposition technique (OACD) to fabricate Ti-doped and V-doped Mg nanorod arrays in a high vacuum physical vapor deposition system. These nanostructures have shown better hydrogen sorption kinetics compared to those fabricated by the ball milling technique [74-77].

For H_2 storage in metal hydrides, the hydrogenation and dehydrogenation processes are always accompanied with heat generation and release. During the hydrogenation process, the hydrogen molecules are dissociated, the hydrogen atoms are captured in the interstitial space between metal atoms, and heat is generated. During the dehydrogenation process, external heat is needed [78]. Thus, heat has to be removed for the exothermic formation process and added for the endothermic decomposition process. As a result, heat transfer properties of metal hydrides are very important for determining the hydrogen sorption kinetics. In addition, the thermal transport will influence the rate of reaction. Insufficient thermal transport will reduce the hydrogenation and dehydrogenation rate of metal hydrides and in the worst case, bring the metal hydride formation to a stop [79]. Consequently, the thermal conductivity of metal hydrides is needed for the design of its practical layout. Hahne and Kallweit adopted a transient hot wire method to determine the effective thermal conductivity of a powdery material [52]. The effects of hydrogen pressure, temperature, and hydrogen-to-metal concentration on the thermal conductivity for $LaNi_{4.7}Al_{0.3}H_x$ were investigated. Kapischke and Hapke applied a transient technique to characterize the effective thermal conductivity of a MgH_2 bed in a high temperature range of $573 - 673$ K and for a hydrogen pressure atmosphere up to 5 MPa [80]. They also introduced an oscillating heating method to measure

the effective thermal conductivity of MgH_2 produced by fine-grained Mg powder in a non-permeated packed cylinder bed reactor in a temperature range of 523 – 653 K [78]. Recently, many numerical models accompanied with experimental validations were introduced to predict the mechanism of heat transfer in metal hydride beds [81-84]. According to the simulation done by Førde *et al*., the effective thermal conductivity was found to be one of the most important parameters during hydrogen reaction in porous beds [81]. Asakuma *et al*. applied a homogenization method to estimate the effective thermal conductivity of a metal hydride bed by considering the microstructure of the reaction bed [85]. So far, most of the investigations on thermal properties are for micro-powder MgH_2. However, the thermal transport properties depend not only on the bulk material properties, but also on microstructures, especially nanostructures. Nanostructure can significantly change the thermal transport property of the same material, thus it could greatly influence the hydrogen sorption dynamics of metal hydrides. Nevertheless, so far, there have been almost no studies on how the thermal transport properties of nanostructured metal hydrides, especially nanostructured MgH_2, are affected by their specific structure and composition. This is mainly due to the lack of a systematic fabrication technique to create metal hydride nanostructures.

1.2 Structure Diagnostics with SPTM at Nanoscale

When an isotropic homogeneous semi-infinite solid is irradiated by a modulated laser, its surface is subjected to periodic heating. The local temperature and thermal expansion which are determined by the local heat transfer, which in turn is directly related to the local properties (thermal conductivity, specific heat, and density), will change periodically. The thermal conductivity is tightly related to the local material structure (defect and crystallinity).

The density can be used to reflect the level of sub-surface nanoscale porosity. These thermophysical properties provide the signature of the local material structure and defect levels. If structural defect (e.g. nanopores) exists below the surface, the local thermal conductivity will be very much reduced. As a consequence, the local heat transfer will be slowed down in comparison with that in good areas. This will lead to a higher surface temperature rise and result in a higher surface displacement (thermal expansion). In order to acquire the difference in surface displacement, a customized atomic force microscopy (AFM) called scanning photothermal microscopy (SPTM) is used to detect the defects in the sample. Unlike the piezoelectric (PZ) detection, in which the laser-induced thermal expansion of a sample is sensed by piezoelectric transducer in contact with the sample, and large scale of non-uniform deformation caused by inhomogenoeous temperature rise, the thermal expansion of the surface is sensed by the nanotip and reflected on the amplitude of the tip. As a result, nanometer scale resolution can be achieved.

The fundamental principle of the SPTM technology is described in Figure 1.1. In this new technology, nanoscale (~10 nm) surface heating will be achieved using the near-field effect with a periodically modulated laser-assisted AFM. When a metal tip is under the illumination of a laser, the polarization component along the tip axis would induce a strong field enhancement. The intensity enhancement factor can be as high as 3000 over the incident light [37]. In the zone near the antenna (tip), the distribution of electric and magnetic fields strongly depend on the tip geometry as well as electrodynamic properties of the surrounding region [86]. This enhanced optical field only exists in a small region less than 10 nm, and will be used to heat up the sample. Under periodical surface heating, the sample surface local

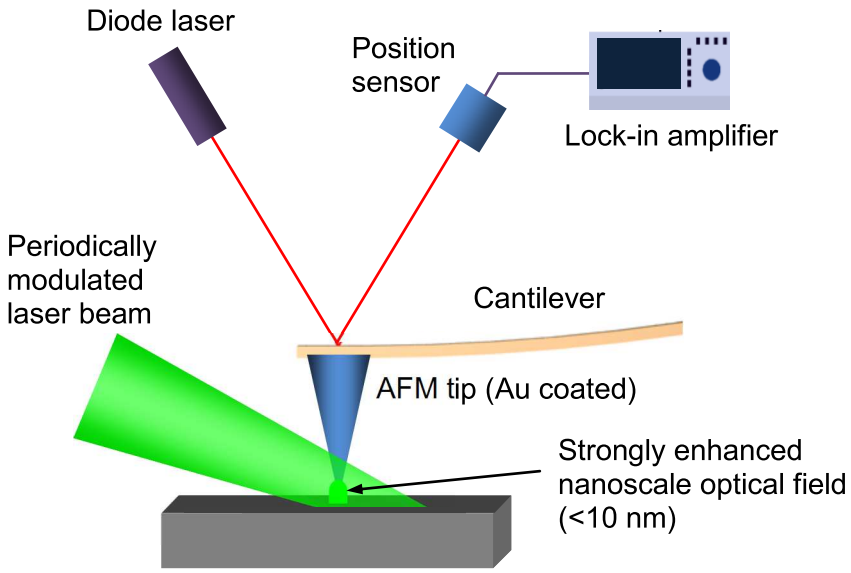

Figure 1.1 Schematic of the SPTM technology. A periodically modulated laser beam is used to irradiate the AFM tip and generate a strong nanoscale optical field below the tip. This strongly enhanced optical field will heat up the substrate and result in periodical change of local surface.

temperature will change periodically. As a result, a local periodically varying surface displacement (thermal expansion) will arise. This nanoscale surface displacement will be sensed by measuring the dynamic response of cantilever in the frequency domain using the AFM tip as shown in the figure. Specifically, using a lock-in amplifier, we will measure the amplitude and phase shift of the surface displacement. The amplitude and phase shift image will give characteristic signatures of the sub-surface structural defects following the physical principle outlined below. Comparatively, most of these technologies as well as scanning thermal microscopy (SThM) [47-50], which maps the local temperature and thermal conductivity of an interface, are focused on characterizing surface properties. Very little information can be collected about the sub-surface structure defect while such information is always critical for evaluating the quality of surface nanomanufactruing and micro/nanometer

scale materials.

As mentioned above, the surface displacement is the signal to be detected. In the SPTM, this signal is reflected as the amplitude of the vibrating cantilever as shown in Figure 1.1. As for the phase shift, there will be a larger phase lag between the surface displacement and the excitation laser. Therefore, the amplitude and phase shift of the surface displacement can be used to characterize the sub-surface structural defects. By varying the modulation frequency of the laser beam, we could detect the structural defect at different depth under the surface. This is because at a modulation frequency f of the laser beam, the surface displacement will be affected by the heat transfer as deep as $(\pi\alpha/f)^{1/2}$. Therefore, structural defect as deep as $(\pi\alpha/f)^{1/2}$ will have effect on the measured amplitude and phase shift of the surface displacement.

1.3 Current State of Knowledge with Laser-SPM interaction

The phenomenon of optical field enhancement has been theoretically reported over the years. An analytical solution for a sphere under laser illumination has been developed by using the Mie scattering theory [87]. To solve the electromagnetic field distribution for a specific geometry, many methods have been used. Examples of such methods include multiple multipole method (MMP) [24,30,37], Green's function method [88], method of moment [89], boundary element method [32,90], generalized field propagator technique [36,91], finite element time domain [92], finite difference time domain (FDTD) method [31,93-98], and The finite element method (FEM) [31,99-105]. The last two modeling techniques are the most popular ones in computational electrodynamics, and both are user-friendly

commercially available. However, FDTD possesses intrinsic limitations for solving the electromagnetic problem at boundaries [106]. The FEM has been proved fruitful for solving electromagnetic problems especially for tip-substrate systems.

Another aspect of interest is the temperature in the tip due to the laser induced heating. When an external laser illuminates a nanoscale tip, heating effect arises from absorption of light. This thermal phenomenon happens in near-field scanning optical microscopy (NSOM) [107-111], apertureless NSOM [96], TERS [112], laser assisted STM/AFM-assisted surface modification and nanofactracation [95,113,114], and high density data storage [115-117].

In aperture NSOM, as the process of passing light through the aperture, a large portion of the incident laser is trapped in the tip area, causing tip heating [107,108]. As heat accumulating near the tip apex, the probe could be damaged as a result of thermal stress caused by different thermal expansions of the fiber and aluminum coating of the coaxial tip [109-111,118-121]. The temperature profiles along aluminum-coated fiber tip due to local heating have been calculated or measured by several groups in the mid 1990s [110,111,118-121]. The heating was shown strongly depending on the cone angle of the tip: decreasing with increasing cone angle [111,121]. The temperature coefficients varied from 20 K/(m·W) for a tip with large cone angle to 60 K/(m·W) for the narrow one [111]. The measured temperature increase at a distance of 70 μm from the aperture (apex) was linear with the input light power until the coating was damaged [111,118]. La Rosa also measured two-time-constant tip expansion in later work [122]. Miskovsky *et al*. [123] solved the heat conduction equation by using the Green function formalism and got the transient temperature distribution for axial symmetric

illumination of the tip.

For apertureless tip, a very strong electromagnetic field is created in the vicinity of the tip apex, which may cause nanoscale heating effects in the tip. The temperature in tungsten tip can rise by about one hundred degrees [99,123]. Maximal tip temperature as high as 650 K was also reported by Ukraintsev and Yates [124]. Mamin and Rugar first used a laser-heated AFM tip and cantilever to create a series of 100 nm depth pits on polymer substrates [115]. Hamann *et al*. used a laser-heated AFM tip magnetic recording method, which is beyond traditional limits, to heat a magnetic material and write less than 40 nm pits, corresponding to a data density of 400 Gbit/in.^{2} [117]. The heated tip can be used as a sharp, nanoscale knife [125-127]. Tarun *et al*. cut CNTs using heated silicon tip which is as high as 1400 K as a nanoscal heat source [127]. Heat flow between the contacted tip and substrate was also investigated in the past [128,129]. Since the heat will transfer to the substrate under the tip, thermal response and thermal expansion were usually coupled in tip-substrate systems come into the category of research [99,124,130-132]. Temperature in thin and semi-infinite metallic sample was also compared [133,134].

In the experimental work introduced above, the exact local temperature hard to measure, which, however, is important for control the results, like the depth and width of the nanoscale pits in nanosurface modification. Even in TERS, the heated then thermal expanded tip will affect the results. An annealing effect triggered by a local temperature rise of 20 – 30 K in the substrate would cause the Au surface smoother, and irreversible Raman signal loss [112]. The only control approach is to tune the input laser intensity to control the temperature of the

tip in a reasonable range, which in turn determines the thermal expansion for specific materials. Usually, the heating need to be controlled to ensure the tip does not adversely affect the sample, especially in probing biological and polymetric materials.

In fact, most of the technologies introduced above did not measure the exact temperature. The temperatures were usually calculated through the interaction of the laser and tip. Specifically, the temperature models [95,114,133,135] as well as thermal expansion [95,125,135-139] for the thermal tips have been reported extensively. Thermal expansion of tips was usually measured under STM mode, for the tip-substrate distance is readily to be calculated thorough tunneling current-gap relationship [139]. Also, theoretical calculation of the temperature rise [37] or temperature distribution [96,112,113,133] provides powerful inspection for laser heated tips. Gerstner *et al*. [99] investigated the temperature distribution along tip axis and thermal expansion of a scanning tunneling microscope (STM) tip by the finite element method. The calculation indicated that the tip-bending due to asymmetric laser heating was of the same order as thermal expansion. The temperature distribution in tungsten was also calculated by the boundary element method (BEM) [133]. The calculations showed that the maximal temperature of the thin metallic film is one order of magnitude larger than for the thick sample [134]. Geshev *et al*. [135] developed a mathematical model for the temperature of a STM tip, based on the averaged one-dimensional heat conduction equation. In this model, the tip is heated by two parts: enhanced field incident on the tip and laser light spot focused on lateral tip boundary. The latter is the main contribution to the thermal expansion of the tungsten STM tip. Downes *et al*. [96] calculated the temperature distribution in the tip-substrate system for a variety of tip and substrate materials, and for air and aqueous

environments under steady state conditions.

Experimental work for measuring heated tips due to laser absorption was mainly done through Raman spectroscopy [113,116,127]. McCarthy *et al*. [116] designed an experimental procedure, based on Raman scattering, for measuring the apex temperature of a laser heated probe tip, and presented a closed-form analytical expression that accurately modeled the heating process. Recently, Milner *et al*. [140] demonstrated a method to determine the tip temperature under laser illumination by observing the shift of the silicon Raman line scattered from the tip and by monitoring the mechanical resonance frequency shift of the probe. Resonance frequency shift method was introduced to investigate the temperature of both AFM tip and cantilever under lateral laser illumination [113]. This latter one, though less accurate, is amenable for practically all standard AFMs.

CHAPTER 2. THERMOPHYSICAL PROPERTIES OF HYDROGENATED VANADIUM-DOPED MAGNESIUM PROSOUS NANOSTRUCTURES

In this chapter, a unique glancing angle co-deposition technique is used to fabricate V-doped Mg nanorod arrays [141]. The samples are hydrogenated and dehydrogenated for 21 cycles. We apply the photothermal technique and a multilayer physical model [16] to characterize the effective thermal conductivity and density of V-doped Mg hydrides nanostructures. The density of the V-doped Mg hydrides is also evaluated by electron micrograph observation, and the two measurement results are compared. The thermal conductivity of bulk V-doped Mg hydrides is also derived based on the measured values.

2.1 Principle and Experimental Setup for the Photothermal Experiment

Figure 2.1 shows the principle of the photothermal experiment. The sample, take MgH_2 for example as shown in the figure, is grown on a silicon substrate. Before experiment, a thin

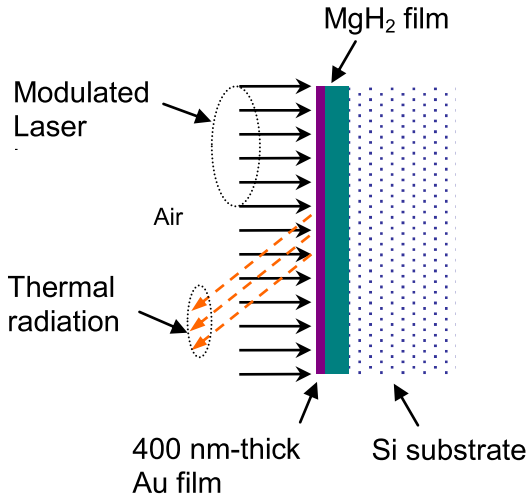

Figure 2.1 Principle of the photothermal experiment.

film with high thermal conductivity like Cr or Au is coated on the sample. A modulated laser beam (λ = 809 nm) is irradiated on the thin-film coated sample. Consequently, a periodic temperature variation arises at the coating surface due to absorption of the modulated laser. The heat from the coating is conducted into the sample layer vertically, as well as the silicon substrate. The radiation signal from the coating is collected by a system, and compared with the incident laser signal. The delay of the radiation signal compared to the incident laser signal is measured in terms of phase shift and used to determine the thermal properties of the sample. The signals of incident laser and radiation under a certain frequency, saying 100 Hz, are shown in Figure 2.2 to illustrate the principle of the photothermal technique.

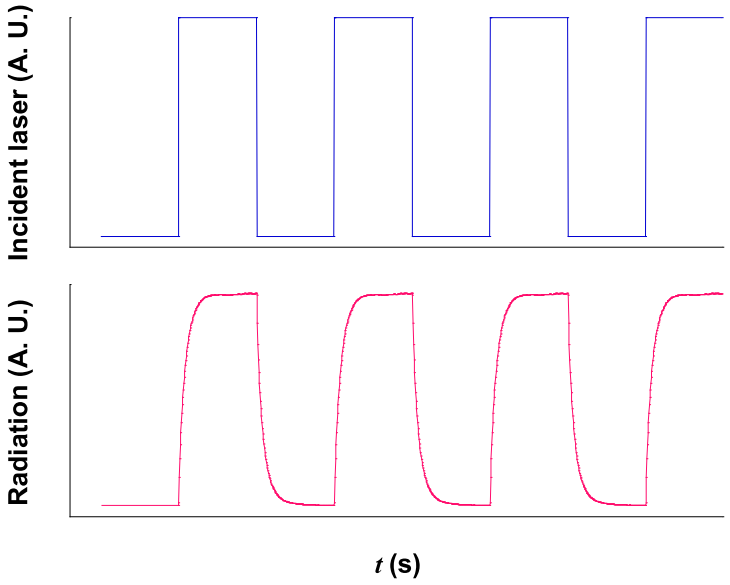

Figure 2.2 The modulated incident laser and the radiation signal from the coating surface under the laser excitation

The schematic of the photothermal experimental setup is shown in Figure 2.3, and the details can be found in our previous work [13,16]. An infrared diode laser (B & W TEK: BWF-2,

809 nm wavelength) modulated by a function generator is used as the heating source. The output laser power is set to be 219 mW, which will induce sufficient thermal radiation signal from the sample. After the laser beam is reflected and focused, it is directed to the sample

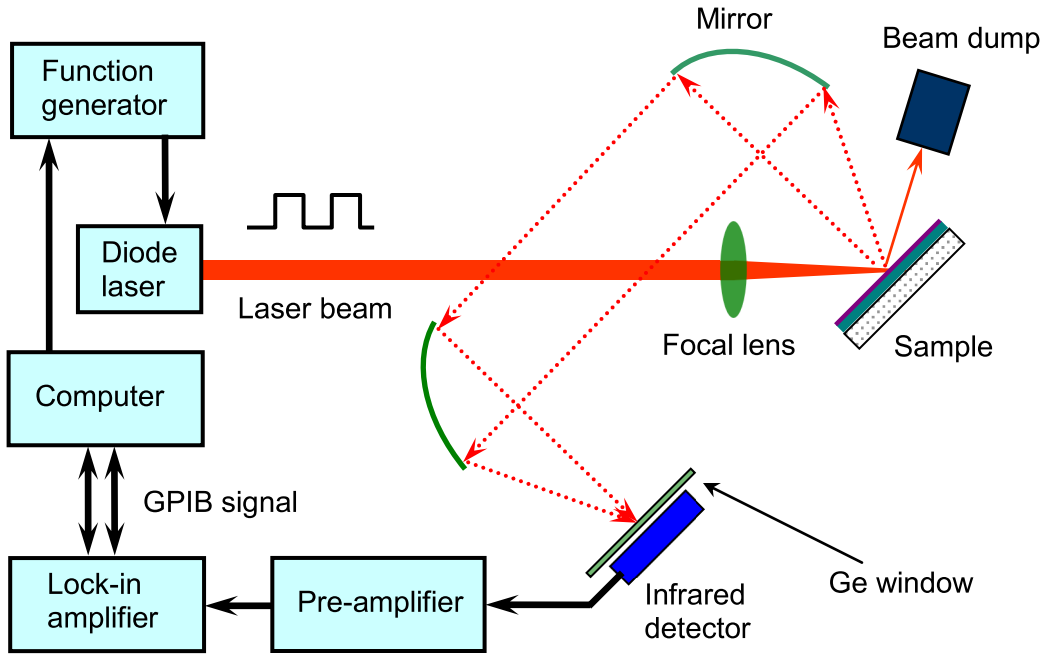

Figure 2.3 Schematic of photothermal experimental setup.

surface, which is angled in approximately 45° relative to the incoming laser beam. At this angle, most of the mirror reflection that should be avoided during experiments is collected by a beam dump. The laser beam follows the Gaussian distribution, and the heating spot size of the laser on the sample surface is approximately 0.7 mm × 1.4 mm [13]. As the heating spot size is much larger than the thermal diffusion depth in the lateral direction of the sample, we can take the beam as a uniformly distributed incident beam. Thus, the thermal conduction in the Au and MgH_2 layers can be treated as one-dimensional (1-D). The specular reflection of the laser beam from the Au film is collected by a beam dump. The thermal emission from the Au film is collected by two off-axis paraboloidal mirrors and is directed into an infrared

detector (Judson Technology: J15D12). A Ge window which only allows the thermal emission to pass through is placed in front of the detector to filter the diffuse reflection. Signal from the infrared detector is transferred to a pre-amplifier, and measured by a lock-in amplifier (Stanford Research: SR830) which is controlled by a PC for data acquisition.

For a multilayer 1-D diffusion problem as shown in Figure 2.4, the thermal diffusion equation in Layer i can be expressed as [5]:

$$\frac{\partial^2 \theta_i}{\partial x^2} = \frac{1}{\alpha_i}\frac{\partial \theta_i}{\partial t} - \frac{\beta_i I_0}{2k_i}\exp\left(\sum_{m=i+1}^{N} -\beta_m L_m\right) \times e^{\beta_i (x-l_i)}\left(1+e^{j\omega t}\right), \tag{1.1}$$

where $\theta_i = T_i - T_{amb}$ and $L_i = l_i - l_{i-1}$ are the modified temperature and thickness of Layer i, respectively, and T_{amb} is the ambient temperature. α_i, β_i, and k_i are the thermal diffusivity,

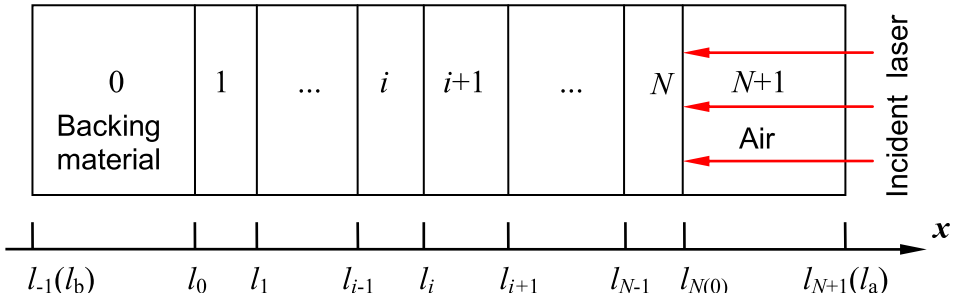

Figure 2.4 Schematic of N-layer model ([5]).

optical absorption and thermal conductivity of Layer i, espectively. The solution θ_i to the equation consists of three parts: the transient component $\theta_{i,t}$, the steady DC component $\bar{\theta}_{i,s}$, and the steady AC component $\theta_{i,s}$. Only the AC component $\tilde{\theta}_{i,s}$ needs to be evaluated and can be picked up by the lock-in amplifier. Details of the photothermal principles and solution can be found in Refs. [5,13,16].

2.2 Experimental Details

2.2.1 Sample preparation

The V-doped Mg nanostructures are fabricated using a unique, custom designed electron-beam evaporation system (Pascal Technology) equipped with a glove box to prevent the sample from exposure to air during the post-fabrication handling. Details of the experimental setup are described elsewhere [141]. The chamber is evacuated to a base pressure of 10^{-8} Torr. Layers of 1 μm thick Ti film (vapor incident angle $\alpha = 10°$ with respect to the substrate normal) and 0.5 μm thick Ti nanorods ($\alpha = 70°$) are evaporated subsequently onto a Si substrate at a deposition rate of 0.1 nm/s. Both the Ti film and Ti nanorod arrays are used as a diffusion barrier to prevent Mg alloying with Si; and V dopoant is adopted to catalyze the formation and decomposition of MgH_2 during hydrogen absorption/desorption cycling [142]. The V-doped Mg nanostructures are then deposited on the nanostructured Ti barrier coated Si substrate by a co-evaporation of both Mg (0.5 nm/s) and V (~0.015nm/s) at $\alpha = 70°$ until the quartz crystal microbalance (QCMs positioned to receive the near-normal deposited atoms) reads 20 μm for Mg and 600 nm for V, resulting in a ~4.6 at.% V-doped Mg nanostructure array. The porus structure is expected to enhance the hydrogen sorption kinetics due to large surface area. The as-deposited samples are cut into 0.5″ × 0.5″ pieces and installed in a PCT Sievert's-type apparatus (Hy-Energy: PCTPro-2000) for H-absorption (under 10-bar H-pressure) and desorption (under vacuum) measurement. After 21 cycles of hydrogenation and dehydrogenation, the hydrogenated samples are taken out for morphological and thermal conductivity characterization.

The morphology of the V-doped Mg nanostructures before and after hydrogenation are characterized by a field emission scanning electron microscopy (SEM, FEI Inspect F), and the representative SEM images are shown in Figure 2.5. From the top view [Figure 2.5(a)] and cross-sectional view [Figure 2.5(b)] SEM images, the as-deposited V doped Mg sample shows an aligned and tilted nanorod-like array structure with an average height of ~8.4 μm and rod diameter of ~300 nm. This array structure is tilting away from the substrate normal at an angle of barrier layer, consisting of a 0.5-μm Ti nanorod array and a 1-μm Ti film, is

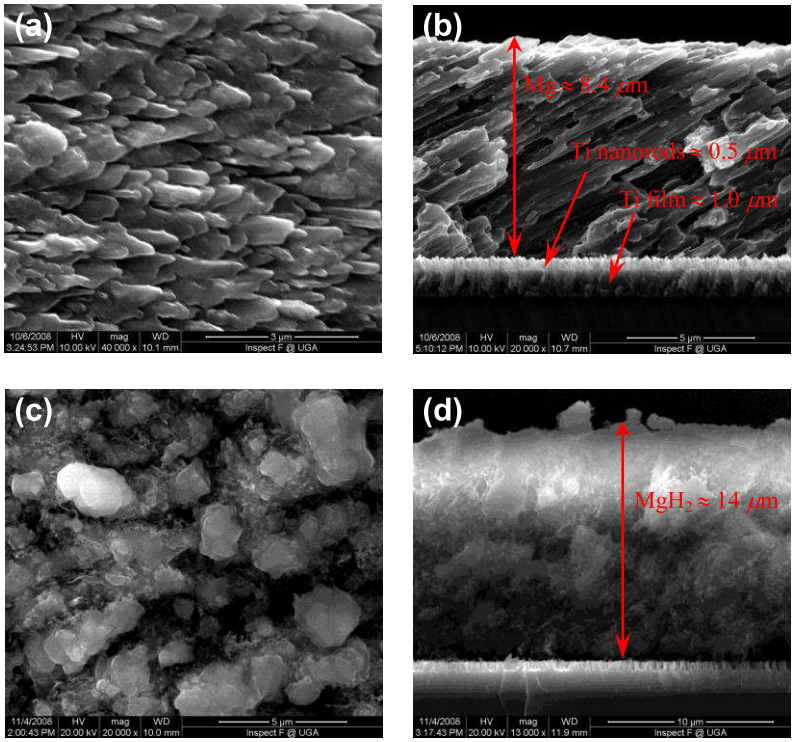

Figure 2.5 Representative top-view (a) and cross sectional (b) SEM images of the as-deposited 4.6% V-doped Mg nanorod sample; representative top-view (c) and cross sectional (d) SEM images of the 4.6% V-doped MgH_2 nanorod sample after the 21st hydrogenation. Figures are provided by Yiping Zhao's group.

visible between the Mg layer and Si substrate, which appears to remain almost unchanged after 21 cycles of H-absorption/desorption [Figure 2.5(b, d)], indicating that such a unique structure of a Ti nanorod array on a Ti film can work quite well as the diffusion barrier between Mg and Si [142]. However, a significant morphology change occurs to the hydrogenated V doped Mg: the original rod structure is totally distorted to form aggregates of sphere-like particles, as shown by the SEM images in Figure 2.5(c, d), and the sample height increases to ~14 μm, corresponding to a height or volume expansion of 67%.

2.2.2 Experimental details for thermal conductivity measurement

A non-contact photothermal technique is used to measure the thermal conductivity of the hydrogenated V-doped Mg nanostructures on Ti coated Si substrates. Note that, after hydrogenation, the metal Mg, V, and Ti become their hydrides MgH_2, $VH_{0.81}$, and TiH_2 according to X-ray diffraction (XRD) as shown in Figure 2.6 [77]. The principles of the experiment are shown in Figure 2.1 in chapter 1. The samples are first sputtering coated with a 200 nm-thick Au film on top of the MgH_2 layer. A modulated laser is used to irradiate the surface of the Au film. As the Au film absorbs the laser, the temperature of the Au layer goes up due to laser heating, which will also be affected by the thermal conductivity of the MgH_2 underlayer. Thus, when the periodically modulated laser light gets absorbed by the Au layer, a periodic temperature variation at the Au surface will occur. However, due to the thermal transport in the underlayer, this temperature variation will have a phase shift with respect to the original modulated laser. Therefore, by measuring the phase shift between the thermal radiation from the Au surface and the original laser beam, one can determine the thermo-

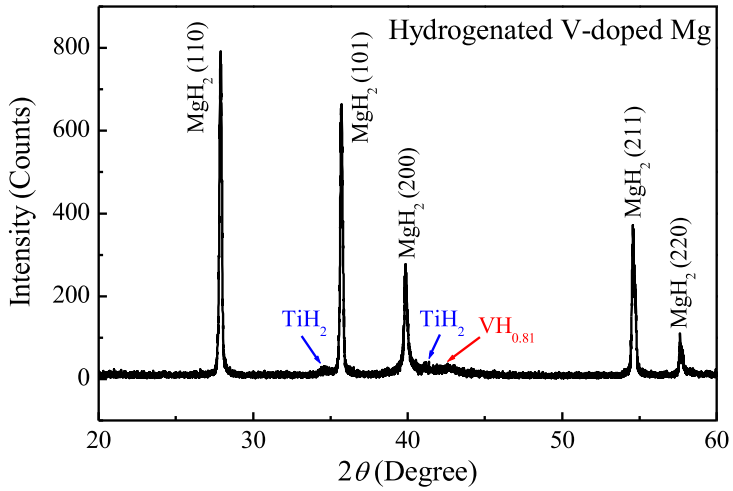

Figure 2.6 XRD pattern of the hydrogenated (in 21st cycle) V-doped Mg nanostructures. It shows that, after hydrogenation, the metal Mg (host), V (dopant), and Ti (barrier layer) become their hydrides MgH_2, $VH_{0.81}$, and TiH_2.

physical properties of the MgH_2 layer. Au is chosen for the surface coating due to its high thermal conductivity and the availability of metal selection in our sputtering coating system (Denton: Desk V).

2.3 Results and Discussion

2.3.1 System calibration

The phase shift between the thermal radiation and the modulated laser is the parameter we want to measure for calculating the thermophysical properties of the samples. The experimental system, however, will inevitably have a systematic phase shift during the operation. This phase shift can be determined by measuring the phase shift (calibration data) between the reflected laser beam from the sample and the original laser beam. If the experimental setup is perfect, the phase shift should be 0. This system phase shift is ruled out

by subtracting the calibration phase shift from the measured phase shift at the corresponding frequencies [5,16] in real measurement. Figure 2.7 shows the measured phase shift of the reflected laser beam at the modulation frequency range from 17 to 400 Hz. The calibration phase shift induced by the experimental system can be calculated in the form of time lag as $\phi_{cal}/360/f$, where ϕ_{cal} and f are the calibration phase shift and modulation frequency, respectively. The phase shift as well as the time lag of the experimental setup is shown in Figure 2.7. The system time lag is 1.5 – 190 μs, which could be induced by the irregularity of the wave shape from the function generator.

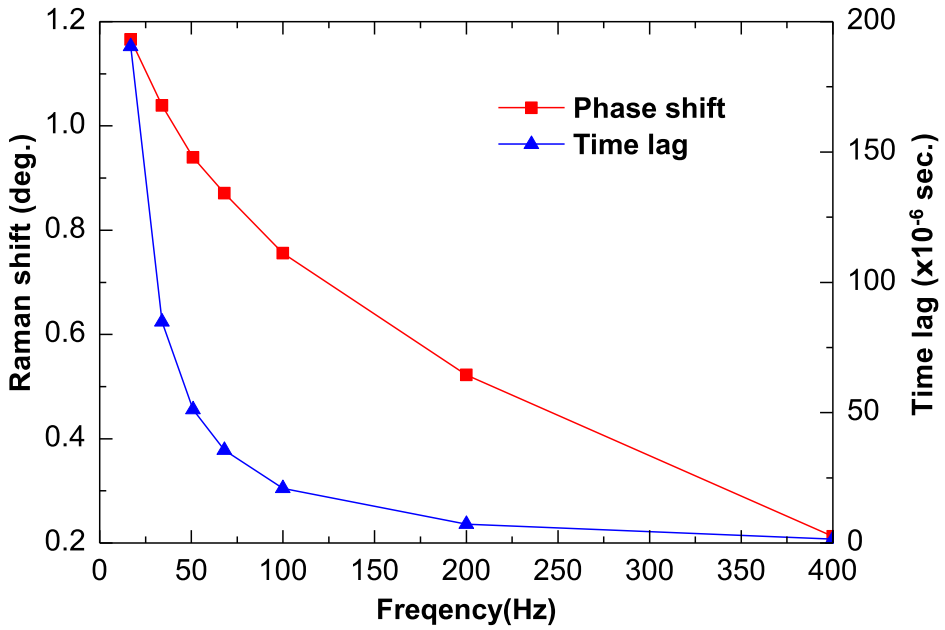

Figure 2.7 The calibrated phase shift ϕ_{cal} of reflected laser beam and time lag of the system.

2.3.2 Measurement results for MgH_2

The Au layer is used to absorb the laser power and generate the temperature gradient that can

propagate into the V-doped Mg hydrides, and emit thermal radiation for detection. The optical absorption length of Au for the laser with the wavelength λ = 809 nm is 13.2 nm [143]. Considering the roughness of the V-doped Mg hydrides sample surface shown in Figure 2.5(c, d), we coat a 200 nm thick Au film on the top surface instead of a thinner layer. In order to make sure the coating is thick enough to absorb the laser beam completely and avoid the laser going through the Au layer, after the measurements with the 200 nm Au coating, another 200 nm thick Au film is coated on the sample, and the thermal radiation is measured again. These two measurements are compared to verify that the infrared laser is completely absorbed by the Au film.

After the experimental setup is calibrated, the phase shift of the thermal radiation is measured in a low frequency range of 17 – 400 Hz. The reason we choose low frequency range is that under a high frequency, the thermal diffusion depth would not exceed the roughness size of the sample. This will impost greater difficulty on data analysis. The phase shift ϕ_t between the thermal radiation and the modulated laser beam is the difference of the measured phase shift of thermal radiation ϕ_{mea} and the calibrated phase shift ϕ_{cal} at the corresponding frequencies, $\phi_t = \phi_{mea} - \phi_{cal}$. The filled symbols in Figure 2.8 show the typical phase shift ϕ_t at different laser modulation frequencies f for 200 nm and 400 nm Au coatings, respectively. For both cases, the $\phi_t - f$ relationship follows the same trend: ϕ_t increases rapidly when f changes from 17 to 100 Hz modulation frequency, it reaches a maximum at f = 200 Hz, and then slowly decreases at higher frequencies. These results can be fitted by a multilayer heat transfer model developed by Hu *et al.* [5]. In our experiments, the multilayer model includes

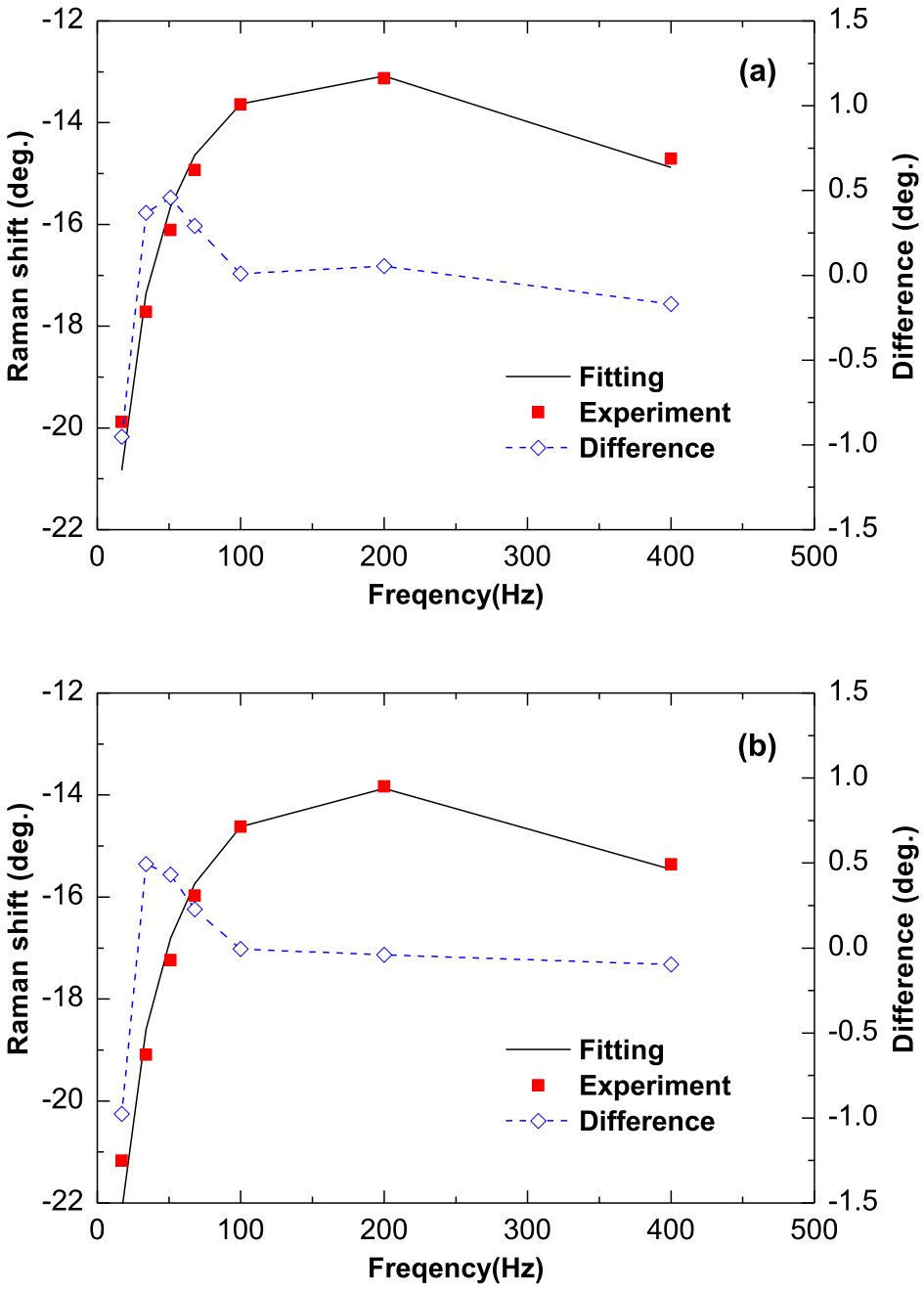

Figure 2.8 The phase shift ϕ_t of the thermal radiation from the Au coating surface of Sample # 1 with 200 nm (a) and 400 nm (b) thick Au film versus different modulation frequencies *f*.

four layers, the air at the top of the Au film, the Au film, the V-doped Mg hydrides layer, and

the Si substrate. We take the TiH_2 layer of a 1 μm thick film and 0.5 μm thick nanorod array as part of the MgH_2 layer (the reason neglecting the thermal transport effect of this layer will be discussed later). With the knowledge of the properties of air, Au, Si substrate, as well as the thickness of an equivalent MgH_2 layer, 15.5 μm, different values for thermal conductivity and density of the hydrogenated V-doped Mg nanostructures in the model are tried to obtain the best fitting. The tried values giving the best fit of the experimental data are taken as the values of the properties.

The solid curves in Figure 2.8 show the best fittings for Sample #1 with 200 nm and 400 nm Au coatings, respectively. For the 200 nm Au coated sample, the obtained effective thermal conductivity k_{eff} is 1.94 W/(m·K); and the density ρ of V-doped MgH_2 is 916 kg/m^3. For the 400 nm Au coating coated sample, k_{eff} = 2.17 W/(m·K) and ρ = 940 kg/m^3. For both cases, the fitting results agree with the experimental data quite well: the difference between the fitting and the experimental data fluctuates in the range of ±0.5°, while the largest difference is only −1°, which is an acceptable uncertainty in the experiment.

The measured effective thermal conductivity k_{eff} and density ρ of three different pieces of V-doped Mg hydrides samples are summarized in Table 2.1. For the sample with 200 nm and 400 nm thick Au coatings, the obtained k_{eff} and ρ values always agree well with each other. Thus, it is safe to conclude that the 200 nm Au coating is thick enough to absorb the incident laser beam and prevent the laser from going through the Au layer. For different samples, the ρ varies from 878 to 1031 kg/m^3, which are smaller than the bulk density of MgH_2, 1450

Table 2.1 Measurement results of different samples.

Sample #	1		2		3	
Au thickness (nm)	200	400	200	400	200	400
ρ (kg/m^3)	916	940	878	952	1018	1031
k_{eff} [W/(m·K)]	1.94	2.17	2.00	2.12	1.60	2.02
φ (%)	36.8	35.2	39.4	34.3	29.8	28.9
k_{bulk} [W/(m·K)]	3.63	3.94	3.95	3.78	2.62	3.25

kg/m^3 [80]. This low density is caused by the porosity of the sample. The measured k_{eff} varies in the range of 1.60 – 2.17 W/(m·K). The large variations in both ρ and k_{eff} from sample to sample could be caused by the nonuniformity of the V-doped Mg hydride nanostructured sample, as shown in Figure 2.5(c, d). To confirm this hypothesis, we have performed five measurements on different locations of Sample #3 with a 400 nm Au coating. These five points are located at the center and the four corners of the sample, and the obtained k_{eff} and ρ are summarized in Table 2.2. Clearly both k_{eff} and ρ depend strongly on the locations: k_{eff}

Table 2.2 Measurement results at five different spots of Sample #3 with 400 nm thick gold film.

Measurement point	1	2	3	4	5
ρ (kg/m^3)	1031	1216	917	1212	1320
k_{eff} [W/(m·K)]	2.02	1.50	1.16	2.40	2.00
φ (%)	28.9	16.1	36.8	16.4	9.0
k_{bulk} [W/(m·K)]	3.25	1.93	2.17	3.11	2.30

varies from 1.16 to 2.40 W/(m·K), and ρ changes from 917 to 1320 kg/m^3. Those variations are comparable to the sample-to-sample variations, and they may come from three factors: the measurement uncertainty, the non-uniform morphology of the V-doped Mg hydride sample, and the different thicknesses at different spots. The porosity will strongly affect the measurement results as will be discussed later. A close look at Figure 2.5(c, d) reveals that the hydrogenated V-doped Mg is not uniform across the entire thickness. One can discern from Figure 2.5(d) that the shade of color of the cross-sectional view SEM image varies from place to place, indicating that the porosity or density of the materials is not homogeneous. Both the top view and cross-sectional view SEM images shown in Figure 2.5(c, d) demonstrate that the surface of the hydrogenated sample consists of micro-sized grains that are not uniformly distributed, which causes the thickness variation.

The measured effective thermal conductivity k_{eff} is in the range of 1.16 – 2.40 W/(m·K), which is considerably different from those reported in literature. Stapßburger [144] found the temporal and local average effective thermal conductivity of MgH_2 to be 7.0 – 9.5 W/(m·K) for the dehydrogenation process at T = 543 – 643 K. Kallweit [145] used a transient technique and obtained k_{eff} = 6 – 7 W/(m·K) for T = 553 K and k_{eff} = 7 – 8 W/(m·K) for T = 593 for MgH_2 under isothermal conditions. Kapischke and Hapke [80] applied a transient measurement method and obtained an effective thermal conductivity of 3 – 9 W/(m·K)for the dehydrogenation process in an MgH_2 bed at T = 573 – 673 K and H_2 pressure up to 5 MPa. They also used an oscillating heating method to obtain the effective thermal conductivity of fine-grained MgH_2 in a non-permeated packed bed under different hydrogen-to-metal ratio

during the hydrogenation process in the temperature range of 523 – 653 K [78]. They found that k_{eff} = 2 – 8 W/(m·K), and close to the completion of hydrogenation, k_{eff} = 1.8 – 2.4 W/(m·K). In our experiment, the V-doped Mg samples are fully hydrogenated before the thermal transport measurement on one hand; on the other hand, our thermal measurement temperature is 298 K, which is lower than those by Kapischke and Hapke. Considering the fact that at low temperature, due to the decreasing conductivity of the solid particle grid [146] or in the other name, the increasing electrical resistivity [147], the effective thermal conductivity decreases slightly when temperature increases, our measurements qualitatively agree with the measurements in [78]. Other measurements results are mostly obtained during the hydrogenation process. Due to partial hydrogenation, the remaining Mg clusters in the structure will play a significant role in determination of the effective thermal conductivity. Thus, it is understandable that the k_{eff} measured during the hydrogenation process is much larger than those we measured. Furthermore, the nanostructures in our samples will also reduce the thermal conductivity due to increased phonon scattering.

2.3.3 The effect of porosity on thermal conductivity

The effective thermal conductivity reported above is affected by many factors, such as the porosity, the microstructure, and small amount of V hydride in the MgH_2. Among them, the porosity plays a critical role. The effective thermal conductivity k_{eff} of a porous material is determined by the porosity φ (the volume porosity factor) and bulk thermal conductivity k_{bulk} through Maxwell's correlation [148]

$$\frac{k_{eff}}{k_{bulk}} = 1 + \frac{3(\gamma - 1)\varphi}{(\gamma + 2) - (\gamma - 1)\varphi}, \tag{2.1}$$

where γ is the ratio of thermal conductivity of the pore material (air) to that of the nanostructure material (MgH_2). Since the thermal conductivity of air, 0.026 W/(m·K), is significantly smaller than that of MgH_2 (see above discussions), we can assume that $\gamma = 0$. The porosity φ can be calculated as

$$\varphi = 1 - \frac{(\rho c_p)_{eff}}{(\rho c_p)_{bulk}}, \tag{2.2}$$

where $(\rho c_p)_{eff}$ and $(\rho c_p)_{bulk}$ are the measured effective volumetric specific heat and bulk volumetric specific heat, respectively. For a composite system with n types of materials, $(\rho c_p)_{bulk}$ can be computed as

$$(\rho c_p)_{bulk} = \sum_{i}^{n} \phi_i \rho_i c_{p,i}, \tag{2.3}$$

where ϕ_i is the volume fraction of component i. In equation 2.3, the hydrogenated V-doped Mg sample can be treated as a composite of MgH_2, $VH_{0.81}$ and TiH_2. Since the layers of the TiH_2 film and nanorod array does not mix with the doped MgH_2, and their thickness (1.5 μm) are much smaller than that of the doped MgH_2 layer (14 μm), we can neglect the effects of the TiH_2 layers. It is known that the atomic fractions of the Mg and V elements in the sample are 95.4% and 4.6%. After hydrogenation, the atomic fractions of MgH_2 and $VH_{0.81}$ are also 95.4% and 4.6%. Consequently, we can also neglect the effect of $VH_{0.81}$, that means we take the composite film as pure MgH_2 for first order estimation to estimate the bulk ρc_p. Such approximation will introduce very little uncertainty due to the low concentration of $VH_{0.81}$. The bulk density and specific heat of MgH_2 are 1450 kg/m^3 and 1440 J/(kg·K), respectively; and the volumetric specific heat/$(\rho c_p)_{bulk}$ of the hydrogenated V-doped Mg nanostructures calculated according to equation 2.3 is 2088 kJ/(m^3·K) at 298 K. The effective volumetric

specific heat $(\rho c_p)_{eff}$ of the hydrogenated V-doped Mg nanostructures is calculated based on the measured density ρ and specific heat [here we use 1440 J/(kg·K)], the values are in the range of 1264 – 1901 kJ/(m^3·K), which is smaller than that of bulk composite MgH_2 and $VH_{0.81}$. According to equation 2.2, the porosity φ of the composite film is predicted to be in the range of 9.0 – 39.4%, which indicates that the porosity varies a lot from sample to sample. Even at different spots on the same sample, the porosity changes dramatically. This nonuniformity could mainly come from the sample hydrogenation/dehydrogenation cycling process. The deposition could not be perfect to form an evenly-distributed crystal array of Mg and V. What is more is that the hydrogenation process could not be uniform, either. The extent of hydrogenation would also affect the distribution of cavities. With the knowledge of volume porosity factors and the effective thermal conductivity, the thermal conductivity of bulk composite films without porosity is derived and listed in the last rows of tables 2.1 and 2.2. The bulk thermal conductivity varies from 1.96 to 3.99 W/(m·K). Such large variation could result from the structure of the MgH_2 itself.

In order to estimate the effect of the TiH_2 layer, the thermal resistance of the TiH_2 layer is compared with that of the layer of the V-doped Mg hydrides. For the TiH_2 film layer, its thermal resistance is l_1/k, where l_1 is the thickness of the film, and k is the bulk thermal conductivity. Since there is no data available for the thermal conductivity of TiH_2 at room temperature, we use the thermal conductivity of $TiH_{1.97}$ instead, 28.4 W/(m·K) [149]. For the TiH_2 nanorod layer, we just take the bulk thermal conductivity multiplied by a coefficient as the thermal conductivity of the nanorods, i.e. βk (β = 0.1 – 0.5 is for volumetric

concentration of the nanorods). The thermal resistance of the TiH_2 nanorod layer is $l_2/(\beta k)$, where l_2 is the length along the axial direction of the nanorods. Consequently, the thermal resistance of the TiH_2 layer is $7.0 - 21.1 \times 10^{-8}$ K/(m^2·W), while the thermal resistance of the layer of V-doped Mg hydrides is $6.46 - 13.4 \times 10^{-6}$ K/(m^2·W), which is approximately two orders of magnitude larger than that of the TiH_2 layer. Therefore, the TiH_2 layer has a negligible effect on the final fitting results. Another thing we must bear in mind is the radiation between the TiH_2 nanorods, which will obviously strengthen heat transfer, thereby decreasing the thermal resistance of the TiH_2 layer. This will make our above conclusion safer.

2.3.4 Comparison of measured density and porosity with electron micrograph observation

In SEM observation, the porosity φ is estimated according to $\varphi = 1 - m/\rho/V$, where V is the volume of the sample as $V = Ah$, A is the projected substrate area, and h is the sample height, which is estimated to be 8.4 μm (for Mg) and 14 μm (for MgH_2) using SEM observations, as shown in figures 1(b) and (d). m and ρ are respectively the mass and bulk density of Mg in the as-deposited sample or the mass and bulk density of MgH_2 in the hydrogenated sample. According to the sample fabrication process, the total mass of Mg on 78 pieces of 0.5″ × 0.5″ substrates is $m_{Mg} \approx 137$ mg, measured by an electronic balance. After 21 cycles of hydrogenation/dehydrogenation, a complete hydrogenation state is reached, which has been verified by neutron scattering experiments. The total mass of MgH_2 can be estimated while ignoring the dopant V, $m_{MgH_2} = m_{Mg} \times (M_{Mg} + 2M_H)/M_{Mg} \approx 148$ mg, where M_{Mg} and M_H are the atomic weights of Mg and H elements, respectively. Thus, the density of the sample is

derived as $\rho_{sample} = m_{MgH_2}/V_{sample} \approx 841$ kg/m^3, which is close to those measured by the photothermal experiments: 878 – 1320 kg/m^3. Therefore, the density estimation based on the SEM observation provides a good reference and validates the measurements by the photothermal experiments. For the bulk material, $\rho_{Mg} = 1740$ kg/m^3 and $\rho_{MgH_2} = 1450$ kg/m^3. Consequently, the porosity can be estimated to be $\varphi \approx 25\%$ for the as-deposited sample and $\varphi \approx 42\%$ for the hydrogenated sample. The porosity φ (for MgH_2) calculated from photothermal experiments is 9.0 – 39.4%, whose upper limit is close to the SEM observation.

2.4 Conclusion

In this chapter, the thermal conductivity and density of hydrogenated V-doped Mg nanostructures were investigated using the photothermal technique. In addition, the thermal conductivity of bulk MgH_2 was also evaluated based on the measured effective values. Our experimental results showed that the effective thermal conductivity of the V-doped Mg hydride nanostructures was in the range of 1.16 – 2.40 W/(m·K), the bulk thermal conductivity was in the range of 1.93 – 3.95 W/(m·K), and the density falls in the range of 878 – 1320 kg/m^3. The density results by the photothermal measurement agree well with those estimated from SEM analysis. Because of the surface roughness and nonuniformity of the nanostructures, the effective thermal conductivity and density vary at different testing points and different samples.

CHAPTER 3. SIMULATION OF NEAR-FIELD THERMAL TRANSPORT IN NANOTIP UNDER LASER IRRADIATION

In this chapter, high-fidelity and full field study is conducted to study the thermal evolution and thermal distribution in a SPM tip under laser irradiation. The electric field distribution and enhancement is calculated in the tip-substrate system by using the FEM. The dependence of field distribution around tip and within tip on incident laser polarization direction, tip-substrate distance, tip apex radius and tip cone angle are studied systematically. According to the electric field distribution within the tip, which would act as a heating source to heat up the tip, the temperature distribution inside the tip is calculated. The influence of geometric factors on the temperature distribution is also reported.

3.1 Basic of Modeling

The modeling is performed by using High Frequency Structure Simulator (HFSS V12.1 Ansys, Inc.), a full-wave high-frequency 3D finite element modeler of Maxwell's equations. A conical tungsten tip whose foremost end is terminated by a hemisphere and silicon substrate system as shown in Figure 3.1(a) is investigated in this work. Maxwell's equations are solved across a defined rectangular computational domain with dimensions *Lx* (650 – 1500 nm), *Ly* (650 – 1500 nm), *Lz* (550 – 3000 nm) containing the tip, substrate, and vacuum filled surroundings. Absorbing (radiation) boundaries which balloon the boundaries infinitely far away from the structure is applied for the domain. The whole domain is split into tetrahedral elements with their length less than $\lambda/4$ (λ: laser wavelength). The mesh is adaptively refined where high field gradient occurs during simulation.

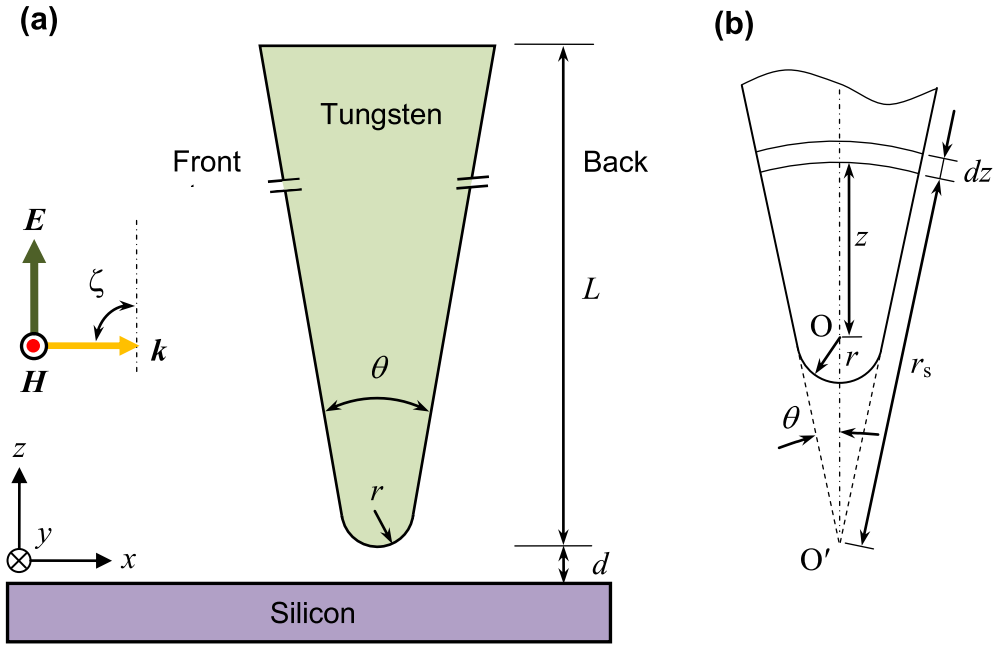

Figure 3.1 (a) Schematic of tip-substrate system studied in this work, (b) geometric structure of the tip. ζ is the incident angle, and it is 90° unless otherwise stated. The polarization angle ϕ is defined as the angle between the electric field vector and the plane of incidence.

Let us consider the scattering of electromagnetic waves by nanoscale geometries (sharp tip for instance here) whose dimensions are small compared with the wavelength λ of the wave undergoing scattering. When this condition holds, the electromagnetic field near the sharp end of the tip may be supposed uniform. Therefore, a plan wave is used in the simulation. The incident angle ζ (the angle between the wave vector $\boldsymbol{k}$ and the tip axis or the normal of the substrate) is 90° for most cases unless otherwise stated. And the electric field amplitude of the wave is set to 1 V/m. Thus, the electric field amplitude of the scattered light is equal to the field enhancement value, which is defined as the ratio of scattered to incident field

amplitude. The polarization angle ϕ is defined as the angle between the electric field vector and the plane of incidence. For most situations, $\phi = 0$, as shown in Figure 3.1(a), except for studying the polarization effects of incident light. The wavelength of incident light is 532 nm. At the corresponding frequency, the permittivities of tungsten and silicon are, $\varepsilon_W = 4.71 + 18.93i$, and $\varepsilon_{Si} = 17.24 + 0.024i$, respectively [143]. The electric conductivities of tungsten and silicon are 5.93×10^5 S/m and 1.34×10^5 S/m, respectively. The real part of permittivity of tungsten is positive (the frequency used in the simulation is larger than plasma frequency ω_p), therefore the surface of the tip does not support propagating surface plasmon, which arises from the collective oscillation of free electrons driven by the incident optical field. On the other hand, the field enhancement still appears because of the resonant tip-substrate system, but much less than that for Ag or Au tips at the same frequency.

The tip shape is described by three parameters: cone angle θ, apex radius r, and length L [as shown in Figure 3.1(a)]. The electric field distribution in the tip-substrate system has been calculated for a range of tip lengths (300 – 2400 nm), and the results show that the field distribution in the system keeps constant in the tip length range (less than 10% difference), which is akin to the conclusion reached by FDTD simulation for $L > \lambda$ [97,150]. Consequently, the length of tips in all models is set as 600 nm, which is a good approximation for commercial tips as long as 15 μm. Different cone angles and apex radii are chosen to investigate the geometric effects on the electric field enhancement, or intensity enhancement that is defined as the squared ratio of scattered to incident field amplitudes multiplied by the ratio of refractive indexes of the media. Simulations have been performed

on a platform consisting of 2.53 GHz Core 2 Duo Processor of Intel with 4 GB RAM.

3.2 Optical Field Distribution Within and Outside the Tip

3.2.1 Optical field distribution

In order to observe how the electromagnetic wave propagates in the tip-substrate system, the streamlines of Poynting vectors are shown in the *x*-*z* cross-section in Figure 3.2. In electromagnetic waves, the energy flow is described by the Poynting vector $\boldsymbol{S} = \boldsymbol{E} \times \boldsymbol{H}$, where $\boldsymbol{E}$ ($\boldsymbol{H}$) represents electric (magnetic) field. In this case, the light is incident along the +*x* direction, and the polarization direction is parallel to the *z*-axis. The tip is perpendicularly located 5 nm above the silicon substrate. In a propagating sinusoidal electromagnetic plane

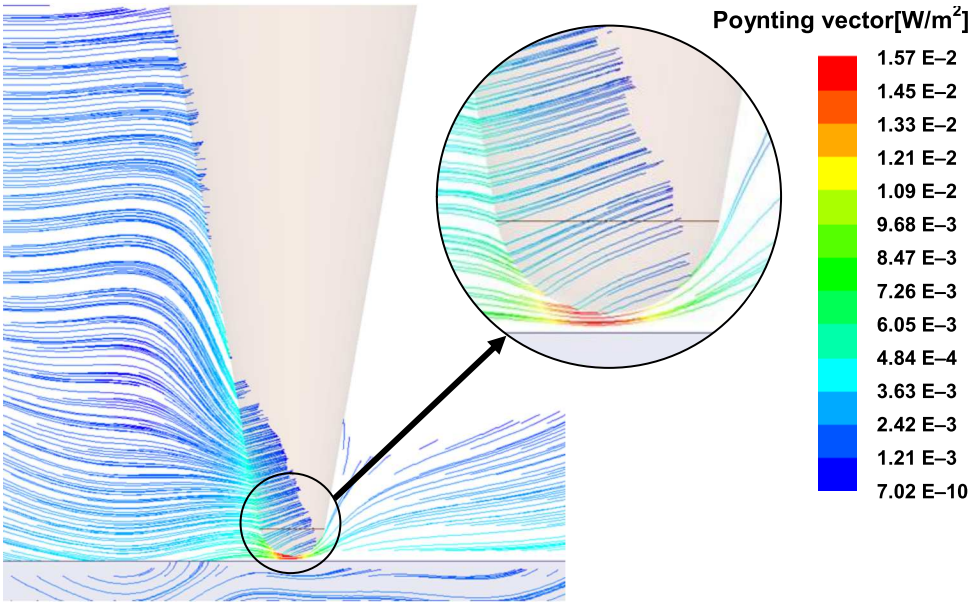

Figure 3.2 Streamlines of Poynting vectors in the *x*-*z* plane (laser is incident from left side). In a propagating sinusoidal electromagnetic plane wave of a fixed frequency, the Poynting vector, presenting the energy flux (in W/m^2), always points to the direction of energy propagation. Simulation configuration: $d = 5$ nm, $r = 30$ nm, $\theta = 20°$ and $\phi = 0°$.

wave of a fixed frequency, the Poynting vector, presenting the energy flux (in W/m^2), oscillates and always points to the direction of energy propagation. As a result, the streamline of Poynting vectors can give some information about the wave factors $\boldsymbol{k}$, or the propagation of the laser beam. When the electromagnetic wave is far away from the tip, the propagation direction is not affected by it, almost perpendicular to the tip axis. When an electromagnetic wave interacts with the conical metal tip, the direction of the electromagnetic wave redirects according to the geometric surface. The direction of the propagation converges toward the tip apex, and to through the gap between the tip and substrate. The laser acts more like fluid, and the tip-substrate like a throttling set. The electromagnetic wave is squeezed in the vicinity of the tip apex. Furthermore, higher energy flow appears in this area as the red streamline shown Figure 3.2. The scattering of electromagnetic waves around the tip is accompanied by absorption. While most of the electromagnetic wave detours around the tip apex to get through the metal barrier, nevertheless, a small portion of the electromagnetic wave plunges into the metal tip, and propagates in the tip following the attenuating rule. That is the reason why the phenomenon of electric field enhancement happens under the tip apex. Also when the electromagnetic field enters the tip, it will bend up a little bit rather than propagate in the x direction due to refraction.

Figure 3.3 shows how the electric field is distributed in the tip-substrate system. From Figure 3.3(a) and (b), it is noticed that strong electric field gradient occurs in the tip-substrate gap; and resonance happens here. The highest field enhancement factor (in this work, all field enhancement bellow refers to the highest field enhancement factor) as high as 15 appears normally beneath the tip apex. Symmetric electric field distribution is observed from the

front as in Figure 3.3(a). However, side view [in Figure 3.3(b)] has a different story: the electric field gradient on the front (upwind) side is stronger than on the back (downwind) side, and the gradient line contour of electric field seems to be blown away along the laser incident direction. The same conclusion is also drawn from top view in Figure 3.3(c): the

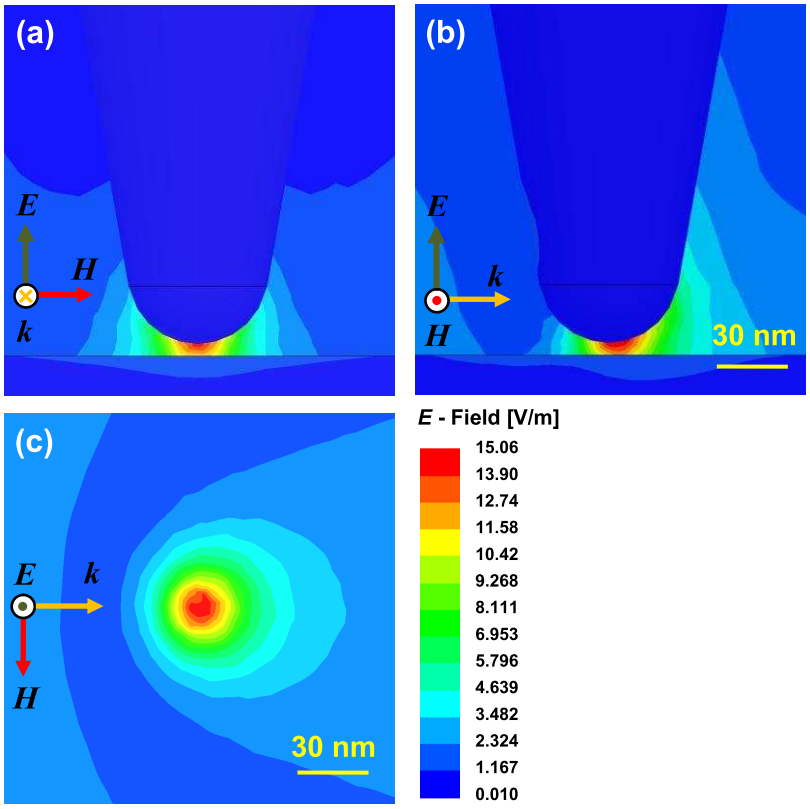

Figure 3.3 Electric field distribution around the tip apex for (a) front view in *y*-*z* plane and (b) side view in the *x*-*z* plane, and (c) Top view of the cross-section under the tip apex. The simulation conditions are the same as those for Figure 3.2.

contour is dense on the front side and sparse on the back side. As regard to the electric field inside the tip, compared to that in the gap zone, it is quite low, for the small amount of laser that propagates into the metal would be absorbed promptly along the propagation direction. On the other hand, the laser beam has plunged into in the silicon substrate within a small

zone beneath the tip, which is the source of Raman signal.

In the next step, we study the electric field distribution inside the tip as shown in Figure 3.4. Observed from upper part of the tip in Figure 3.4(a) and (b), the electromagnetic field impinges into the metal tip from all directions, and then is attenuated toward the tip core. As expected, the electric field inside the tip on the front (upwind) side is much stronger than that

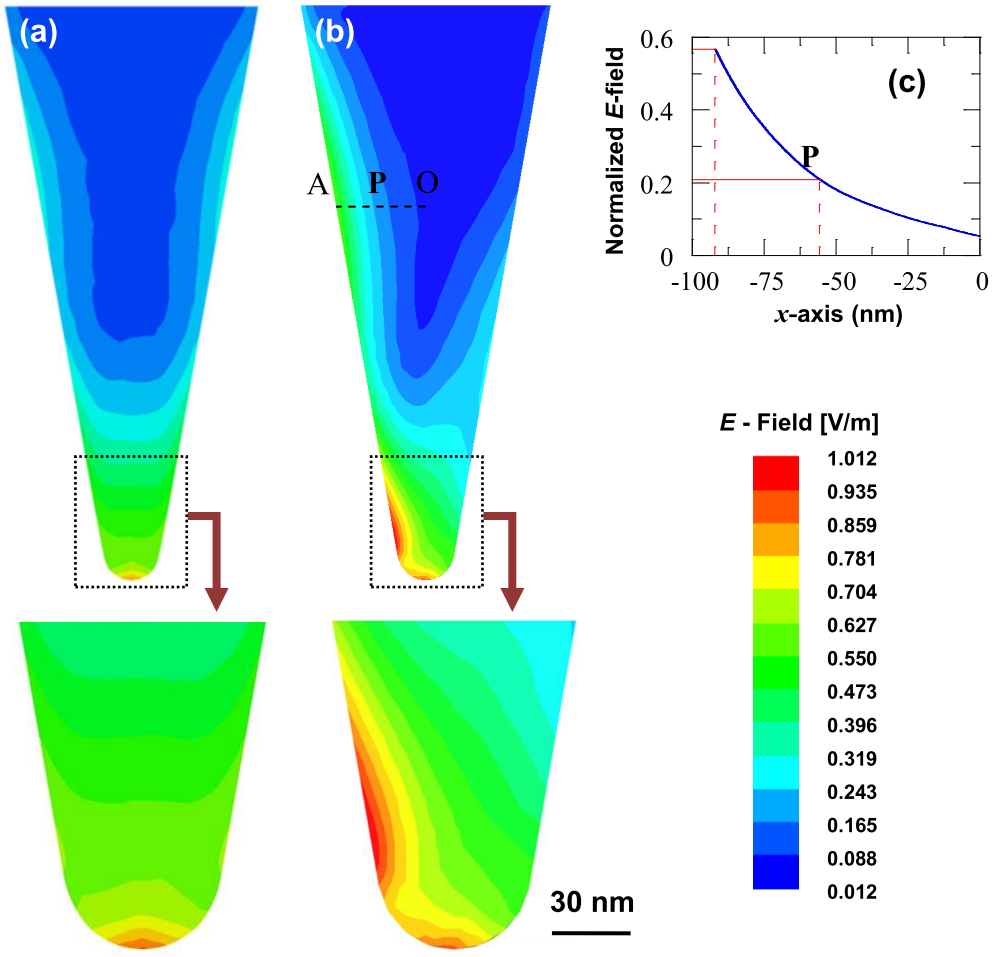

Figure 3.4 Electric field distribution inside the tip for (a) front view of *y*-*z* cross-section and (b) side view of *x*-*z* cross-section, and (c) along line AO. In figure (c) P is the point where the amplitude of electric field drops to e^{-1} of that on the surface, and AP is called skin depth. The simulation conditions are the same as those for Figure 3.2.

on the back (downwind) side as shown in Figure 3.4(b). In Figure 3.4(c), the electric field amplitude drops exponentially as the electromagnetic wave transmits into the core of the tip. As the amplitude drops to e^{-1} of that on the surface, the length from the surface to P is called skin depth δ, which is 36.5 nm, a little larger than the theoretical value 31.1 nm ($\delta = \lambda/2\pi\kappa$). Considering the electromagnetic wave inside the tip is the superposition of the electromagnetic wave transmitted from all surrounding directions other than only from the $-x$ direction, the appearance of position P is postponed toward the core of the tip. Meanwhile, the bending up of the electromagnetic wave direction after it enters the tip surface as shown in Figure 3.2 is also a reason why the skin depth calculated in the x direction is larger than the theoretical value. Exam the electric field distribution in the sharp part of the tip in Figure 3.4(b), we find the strongest electric field is as high as 1.01 V/m, even stronger than that of the incident laser. However, this does not violate the optical law, for the amplitude outside the tip is much higher than the input laser, no wonder the amplitude inside is higher than 1 V/m.

3.2.2 Laser polarization direction

The field enhancement depends strongly on the incident field polarization. Novotny *et al.* have shown the electrical field component along tip axis gives rise to the field enhancement [37,38]; Martin & Girard concluded the vertical field component plays a dominating role [36]. Similar conclusions have been reported by Zayats [151], Downes [31], and Wang *et al.* [97]. In Figure 3.5, data for the relationship between field enhancement around apex and polarization direction is depicted by circles. Obviously, the field enhancement declines as the polarization direction angle ϕ increases. When $\phi > 85°$, no field enhancement under the tip

apex exists (i.e. the enhancement factor is less than 1). This is consistent with the results reported that incident light with polarization perpendicular to the tip axis results in no field enhancement [36-38].

However, Royer [103] demonstrated that for the component parallel to the tip axis the enhancement factor is about 10 times larger than that obtained for the component perpendicular to the tip axis. If only taking into account the projection of the incident electric field on the z-axis, i.e. z-component, then the modified field enhancement, which is equal to the ratio of electric field intensity under tip apex to the z-component of the incident electric field $\boldsymbol{E}/\boldsymbol{E}_{z,\mathrm{in}}$, is independent of the polarization direction. This is clearly depicted by triangles in Figure 3.5: a flat line appears as ϕ varies. So it is conclusive that the field enhancement depends on $\cos\phi$, and the perpendicular component of the incident electric field has no

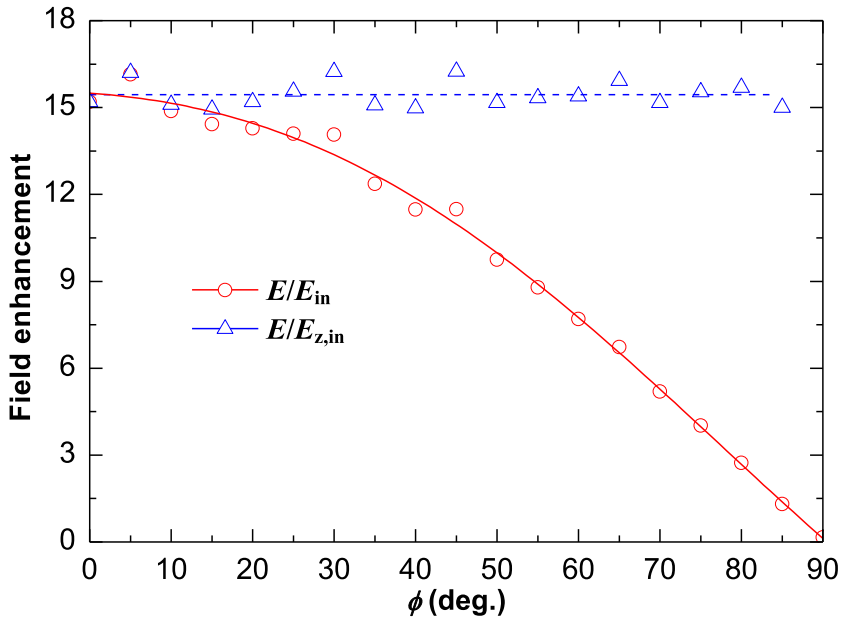

Figure 3.5 Field enhancement for different polarization angles. In these cases, d = 5 nm, r = 30 nm and θ = 20°.

contribution to the field enhancement. Similarly, the intensity enhancement depends on the square of $\cos\phi$.

3.2.3 Effect of tip geometry

Since the tip and substrate are coupled, the tip-substrate distance has substantial influence on the performance of the system, like the atomic force and tunneling current are phenomenally sensitive to the tip-substrate distance in SPM systems. Also, the resonant situation is strongly dependent on the tip-substrate distance. Demming *et al.* figured out an inversely proportional relationship between field enhancement and the tip-substrate separation distance [90]. Madrazo *et al.* also demonstrated a monotonic increase behavior as the tungsten probe approaches the interface [152]. In Figure 3.6 we study the influence of the tip-substrate distance on the field enhancement. For r = 30 nm, polarization in the z direction, when d =

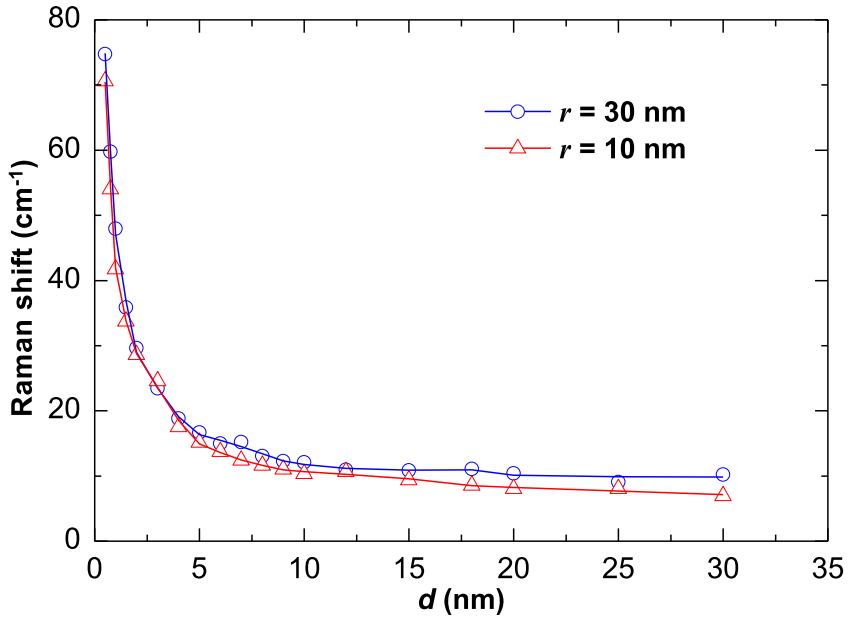

Figure 3.6 Dependence of the field enhancement on tip-substrate distance. In these cases, $\theta = 20°$, and $\phi = 0°$.

0.5 nm, extremely strong field gradient is observed beneath the tip apex, where the field enhancement is as high as 71.6. As the tip-substrate distance increases, the field enhancement factor declines exponentially; when the distance reaches 5 nm, the field enhancement dramatically drops to 15.2. When $d > 5$ nm, the field enhancement decreases mildly. With $d = 20$ nm, field enhancement is only 8.1. As $d \rightarrow \infty$, i.e. there is no substrate under the tip, the field enhancement factor is as low as 3.7. For $r = 10$ nm, same trend is observed when the tip-substrate distance increases. And the field enhancement is slightly smaller than that for $r = 30$ nm.

Another interesting phenomenon is that the peak electric field position has a shift away from the tip-axis surface on the tip surface as the tip-substrate distance increases, similar results have been reported by Wang *et al.*, that a field peak shift away from the tip-axis was observed at large laser incidence angles [97]. Figure 3.7 shows the electric field distributions along the intersection line of the tip apex surface and *x*-*z* plane for different tip-substrate distances. When $d \leq 5$ nm, the peak position appears normally under the tip axis; the more the tip approaches the substrate, the more symmetrical the field appears on both sides of the tip apex along the *x* direction. When $d > 5$ nm, the peak position shifts away with a small distance (15 – 30 nm for these specific simulations) from the tip axis in the $+x$ direction (away from the laser incident direction); meanwhile, the field magnitude on the right of the tip axis is much larger than that on the left. Figure 3.8 clearly shows the peak position shifts to the right when the tip-substrate distance increases. If this phenomenon has been detected during laser-assisted nanopatterning experimental, the nanopattern under the tip also would

be offset with a distance of 15 – 30 nm. Further experimental proof is needed for such phenomenon.

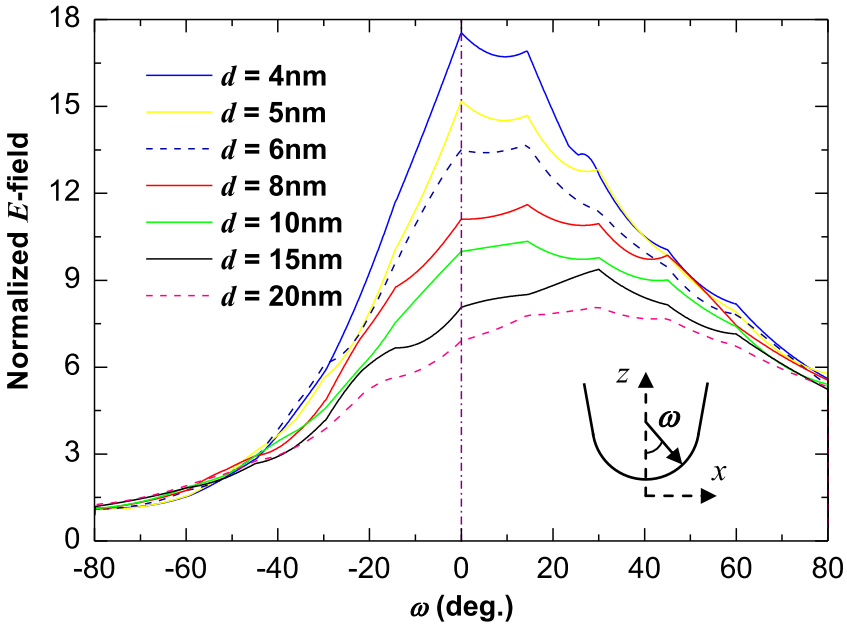

Figure 3.7 Electric field distribution along the tip surface in the *x*-*z* plane for different tip-substrate distances. ω is the lateral angular displacement. For these simulations, θ = 20°, r = 30 nm, ϕ = 0°, are used.

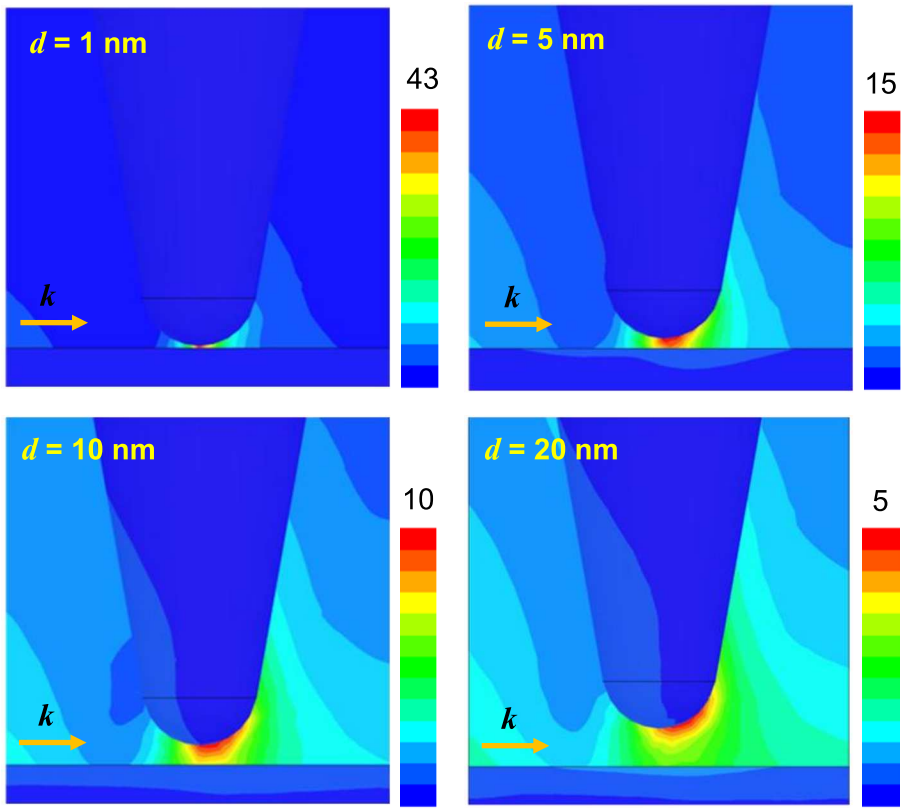

Figure 3.8 Field enhancement under the tip apex for different tip-substrate distances. The simulation conditions are the same as those for Figure 3.7.

Figure 3.9 shows the field enhancement under the tip apex for various radii and cone angles. The effect of tip radius on the field enhancement are present in Figure 3.9(a) for $\theta = 20°$, $d =$ 5 nm and $\phi = 0°$. When the apex radius decreases from 35 nm to 8 nm, the field enhancement goes up from 15.0 to 17.2. When the apex radius decreases further to 5 nm, the field enhancement goes down to 15.3. These calculations provide an insight regarding to the field enhancement by tips with different apex radius: tips small apex radius generate stronger field enhancement, this is akin to the static "lightning rod" effect, that charge accumulation at sharp end in metal objects results in strong fields [93]. However, the small of the apex radius

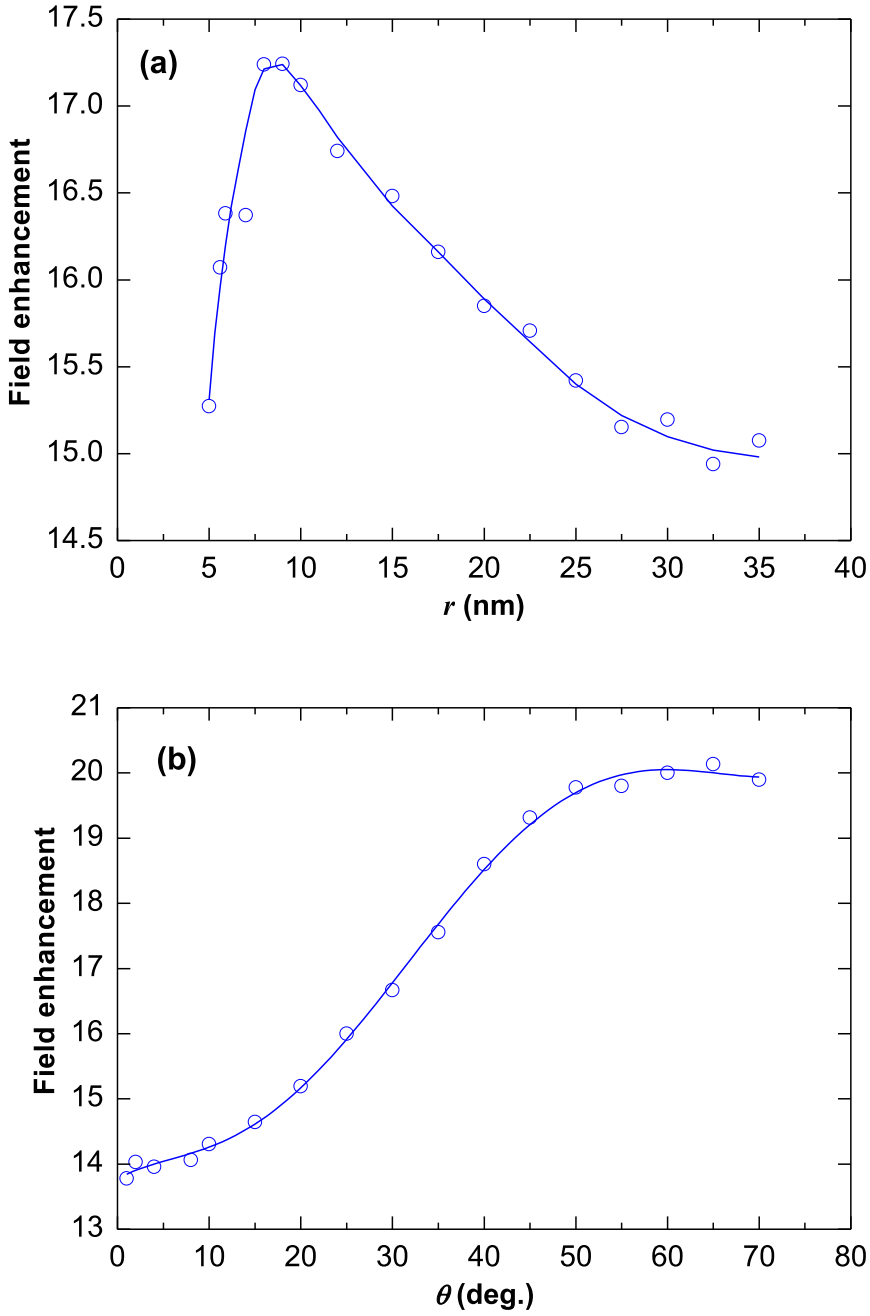

Figure 3.9 The effects of (a) apex radius and (b) cone angle on field enhancement. Simulation conditions are (a): $\theta = 20°$, $d = 5$ nm, $\phi = 0°$, and (b): $r = 30$ nm, $d = 5$ nm, $\phi = 0°$, respectively.

plane wave will penetrate through the foremost end, because of the finite skin depth at optical

is not the entire story. When the apex radius is too small, more excitation plane wave more of the excitation frequency (36.5 nm at 532 nm excitation, as discussed in previous section). Thereby, the field enhancement will drop down. The relationship between cone angle and field enhancement is shown in Figure 3.9(b). As the cone angle θ increases from 0 to 50°, the field enhancement under the apex increases from 14.2 to 20.0. When θ is larger 50°, the peak field enhancement experiences a plateau until $\theta = 70°$.

Figure 3.10 shows how the field enhancement around the tip apex vicinity changes with different incident angles. Generally speaking, larger incident angle can induce stronger field enhancement. The optimal incident angle is approximately 75°. The result is consistent with most of the reported values. Lu *et al.* [89] proved from simulation that the strongest field

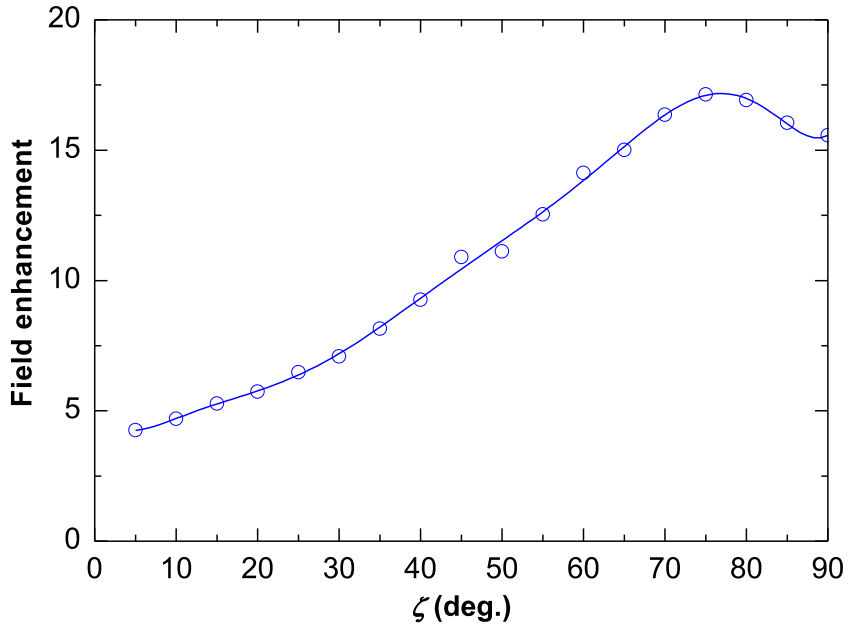

Figure 3.10 Incident angle dependence of the field enhancement around tip apex vicinity. In these cases, $d = 5$ nm, $r = 30$ nm, and $\theta = 20°$.

enhancement happens when the incident laser is perpendicular to the tip axis. Other optimal incident angles like 80° [138,153], 73° [154], 60° [36] have been used in experiments. However, simulation from Wang *et al.* [97] demonstrated the incident angle of 30° is optimal.

3.3 Tip Heating by the Incident Laser

3.3.1 Laser heating mechanism

In electromagnetic waves, the energy flow is described by the Poynting vector:

$$\boldsymbol{S} = \boldsymbol{E} \times \boldsymbol{H}, \tag{3.1}$$

where $\boldsymbol{E}$ ($\boldsymbol{H}$) represents electric (magnetic) field. Substituting $\boldsymbol{H}$ into $\boldsymbol{E}$ according to Maxwell's equations, the Poynting vector gives the intensity (i.e. energy flow per unit area in W/m^2) of the incident light [155],

$$I = S = 0.5 c \varepsilon_0 n E^2, \tag{3.2}$$

where I is the intensity of incident light in W/m^2, c (3×10^8 m/s) is the light speed in free space, ε_0 is vacuum permittivity, n refractive index of medium. The heat generation rate per unit volume is $\dot{q} = I\alpha$ where $\alpha = 4\pi\kappa/\lambda$, termed absorption coefficient, κ is extinction coefficient and λ the wavelength in free space.

The incident laser beam is assumed to be spatially uniform, corresponding to a plane wave in HFSS simulation, and has a temporal distribution as

$$I = I_0 \exp\left(-\frac{(t - t_0)^2}{t_g^2} \right), \tag{3.3}$$

where I_0 is a laser beam intensity constant, t_0 the peak time (= 20 ns), and t_g (= 6 ns) is a time

constant. The profile of incident laser intensity is shown in Figure 3.11. The full-width at

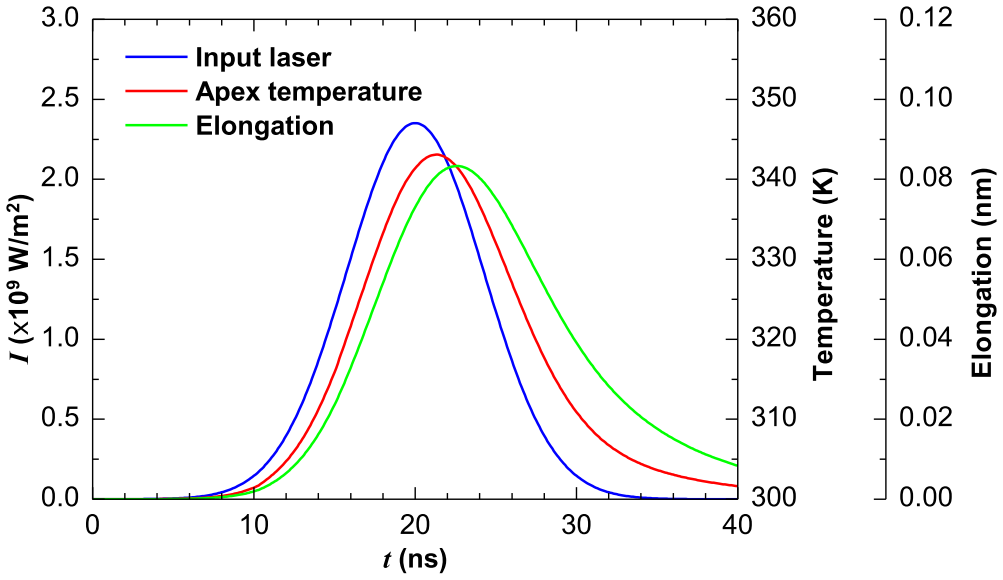

Figure 3.11 The incident laser pulse profile, tip apex temperature and tip elongation over time under the illumination of incident laser. The peak temperature which is 343.08 K is behind the peak of the laser pulse by 1.3 ns, and the largest elongation, 0.83 nm, is 2.6 ns behind. Simulation conditions: $\theta = 20°$, $r = 30$ nm, $d = 5$ nm, $\phi = 0°$ and $q'' = 2.5$ mJ/cm^2.

half-maximum (FWHM) of the laser pulse is 10 ns centered at $t = 20$ ns. In our work, only a single laser pulse is considered, i.e. the total simulation time is 40 ns. In order to simplify the simulation, the pulse energy per unit area of the pulse q'' is set prudently to induce a moderate tip temperature rise less than 50 K. Consequently, the tip (tungsten) thermal conductivity and specific heat variation against temperature is less than 5%, and this small change can be neglected. Meanwhile, the reflectance, permittivity and electric conductivity of tungsten can also be taken as constant, assuring we can use the field distribution inside the tip calculated at 300 K under other temperatures without causing too much variation.

In our study, the pulse energy per unit area of the incident laser is written as q'', with which I_0 in equation 3.3 can be obtained. The intensity $I(t)$ of the incident laser at time t is calculated according to equation 3.3. Then substitute $I(t)$ into equation 3.2 to obtain the incident electric field magnitude $E_{inc}(t)$ in vacuum. Since the electric field distribution inside the tip has been calculated in the former sections with unity incident electric field intensity, and obviously the linear relationship is valid between the incident electric field and the one inside the tip. The electric field distribution within the tip: $E_{tip}(x,y,z,t)$ under the condition that the energy density of the incident laser pulse is q'' can be obtained by scaling the previously calculated results. With $E_{tip}(x,y,z,t)$ and equations 3.2 and 3.3, the laser intensity absorbed in the tip $I_{tip}(x,y,z,t)$ as well as heat generation rate per unit volume $\dot{q}_{tip}(x,y,z,t)$ can be calculated, which plays as heat source inside the tungsten tip.

With the knowledge of heat source distribution within the tip, the temperature distribution would be available. Commercial computational software ANSYS FLUENT (V12.0.1 Ansys, Inc.) is used to simulate the temperature distribution within the tip. The length of the tip is 2 μm, and heat source is distributed at the small end of 600 nm length following laser illumination situation calculated by HFSS. Since the heat transmitted through the vicinity air by convection and heat transferred by radiation to environment can be neglected for high thermal conductivity materials (the thermal conductivity of tungsten is 174 W/(m·K) at 300 K), it is reasonable to set the peripheral and hemispherical end surface as adiabatic. The large top end surface of the tip is set 300 K. The initial temperature of the tip is 300 K.

3.3.2 Temperature evolution and distribution inside the tip

According to all our simulations, the highest temperature point is located at the tip apex during the laser illumination. Hence, the apex temperature can be used as a parameter for monitoring during simulation and for comparison. In this study, the incident laser energy is set as 2.5 mJ/cm^2. Figure 3.11 shows the incident laser intensity profile and the development of apex temperature over time under the illumination of incident laser. Because the heat conduction in the tungsten tip is very quick due to its high thermal conductivity, the profile of apex temperature is akin to the incident laser profile. The maximal temperature increase is 43.1 K, and appears 1.3 ns behind the laser pulse peak. Such delay is induced by heat conduction in the tip.

In Figure 3.12 four *x*-*z* cross-sectional views of temperature distribution at different times are shown. In Figure 3.12(a), t = 10 ns, only a third of the sharp end has been influenced by the incident laser heating, and the temperature distribution is noticeably asymmetric to the tip axis. The temperature is higher in the front or laser incident side. The nonuniform temperature distribution would induce asymmetrical expansion, which has been confirmed in simulation results [99] and observed in experiments [138]. At 20 ns, the temperature gradient develops far away from the tip apex, and asymmetric temperature distribution still exists to some extent. At 30 ns, the temperature distribution is more evenly distributed along the tip axis direction; asymmetry only exists at the sharp end. At the end of laser heating (40 ns), the temperature distribution is fully developed, and asymmetry disappears. If the whole tip is divided into numerous concentric layers, or spherical crowns, as demonstrated in Figure

3.1(b), it's obvious that each concentric spherical crown can be approximately treated as

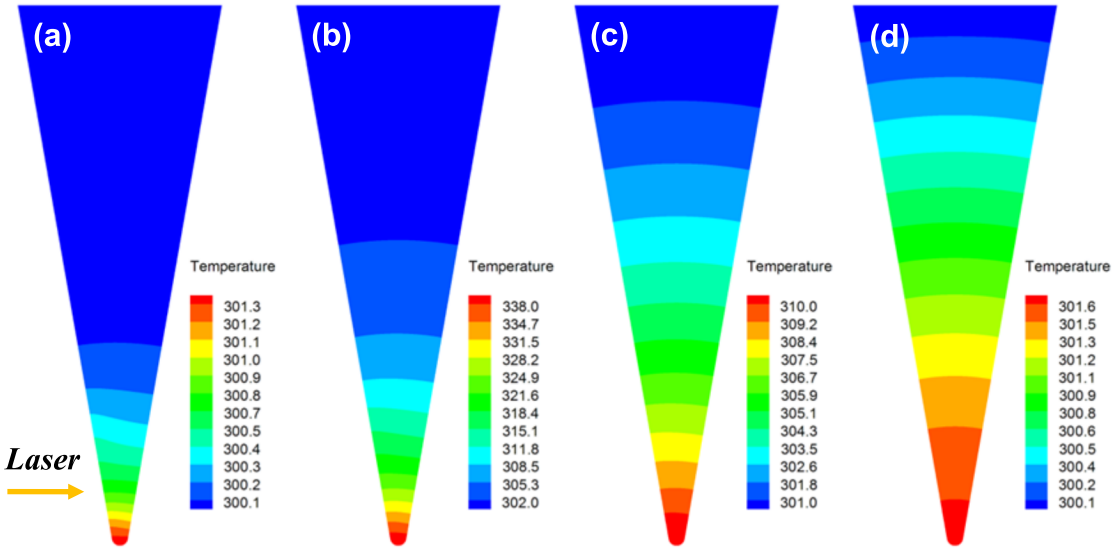

Figure 3.12 *x-z* cross-sectional view of the temperature distribution at (a) *t* = 10 ns, (b) *t* = 20 ns, (c) *t* = 30 ns, and (d) *t* = 40 ns. The simulation conditions are the same as those for Figure 3.9.

isothermal layer, which is the same as in Ref. [99,132] during cooling process, especially for the zone far away from tip apex or for temperature fully developed. Furthermore, the temperature in the axis is used to represent the temperature of the corresponding concentric spherical crown. Consequently, the temperature distribution along the tip axis can fundamentally reflect the temperature distribution within the whole tip.

Thermal expansion of SPM tips induced by lateral laser heating has been reported in many literatures [95,97,124,130,151,152,156]. Thermal expansion from less than 0.01 nm [131], several nanometers [95,132], and to as long as 15 nm has been observed [125]. As the thermal expansion of the tip is not the focus of this work, we only do the analysis for one heating condition to look into the tip physical behavior. Neglecting the weak non-uniformity

of the temperature distribution in the tip radial direction, the tip elongation (δL) can be calculated as $\delta L = \int_0^L \alpha(T - T_0)dl$. T_0 is the initial temperature and α the linear thermal expansion coefficient of the tip (4.5 × 10^{-6} K^{-1} for tungsten). The thermal elongation is calculated and shown in Figure 3.11. The largest thermal elongation is 0.83 nm, and is 2.6 ns behind the peak of the input laser pulse, or 1.3 ns behind the peak apex temperature. Thermal expansion delay was also reported in pulsed laser illumination [99]. Generally speaking, the thermal expansion is directly related to the temperature distribution along the tip axis, and it is in phase with the integrated temperature increase along the tip axis. The latter, as expected, is lag in phase to the tip apex temperature. Comparing the three curves in Figure 3.11, though the temperature and thermal elongation are lag in phase with respect to the input laser, their responses are still quick enough to follow the change of the input laser in one pulse. This quick time response of the thermal expansion differs from that reported by La Rosa *et al.* [122]. In their work, the tip is irradiated with a relatively long laser pulse (10^{-3} second or longer), and the tip thermal expansion features a two-time-constant behavior. The short time (initial) behavior reflects the quick thermal energy accumulation near the tip apex region, and the long time behavior is largely attributed to the thermal transport along the tip.

The temperature distribution profiles along the tip axis at different times during laser heating are shown in Figure 3.13. The *z*-axis presents the distance to the tip apex. The lines with filled symbols represent the temperature increasing process or heating process, while all the other lines describe the temperature dropping process or cooling process. It is noted that the temperature changes dramatically at the sharp end, and mildly at the blunt end for all the

lines. Additionally, the temperature in the blunt end lags behind that in the sharp end. After *t* = 30 ns, the temperature profiles are almost linear, corresponding to the homogeneous distributed color bands in Figure 3.12(c) and (d).

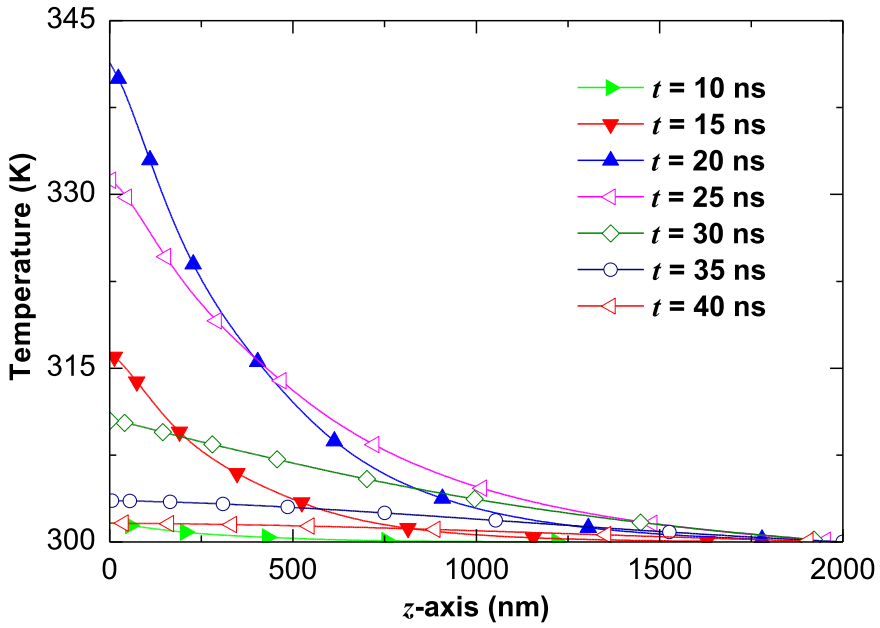

Figure 3.13 Temperature distribution along the axis of the tip at different times during laser heating. The z axis is the distance to the tip apex. The simulation conditions are the same as those for Figure 3.11.

3.3.3 Effect of laser polarization and tip geometry on heating

In order to investigate the laser absorption within the tip, the mean laser intensity enhancement (square of field enhancement multiplying ratio of refractive indexes of tungsten and air) is observed in the process of simulation. Since the temperature of tip apex is directly influenced by the heat source in the apex zone, which in turn is determined by the laser intensity, the mean laser intensity near the tip apex is extracted to correlate with the peak apex temperature. The decline in peak apex temperature and mean laser intensity near tip

apex versus polarization direction angle is shown in Figure 3.14. In this study, the incident

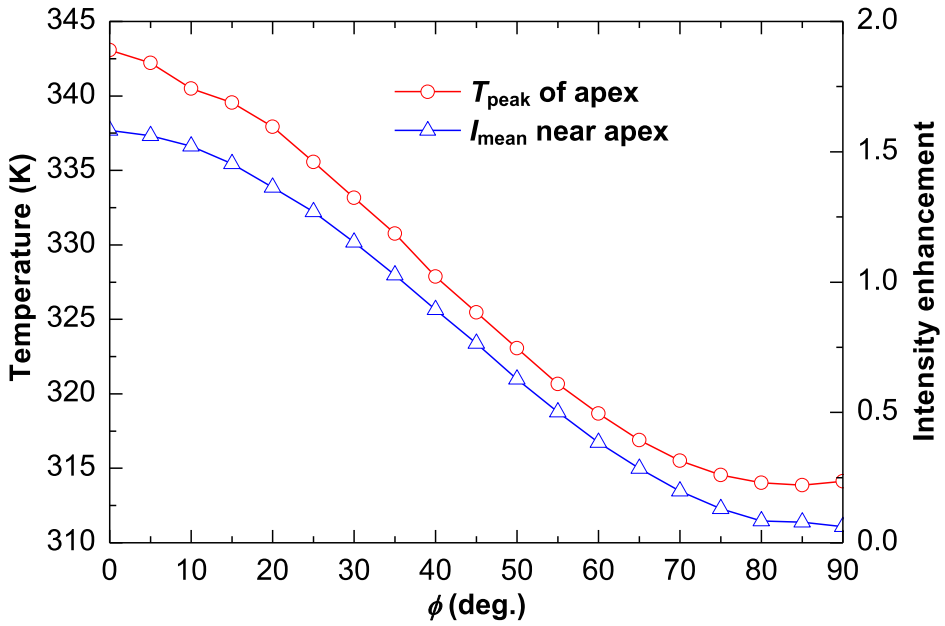

Figure 3.14 Peak apex temperature and mean laser intensity near apex inside the tip versus polarization angles. Simulation conditions: $\theta = 20°$, $r = 30$ nm, $d = 5$ nm, and $q'' = 2.5$ mJ/cm^2.

laser energy is chosen at 2.5 mJ/cm^2. As the ϕ increases, the laser intensity near tip apex goes down gradually, that means the heat source declines with the increasing ϕ, which directly affects the peak apex temperature. The electric field or laser intensity within the tip also has the same dependence trend on polarization direction as the peak enhancement factors beneath the apex as discussed in Section 3.2.2. The mean laser intensity goes down as the polarization angle θ increases. This directly results in the monotonously descending of peak apex temperature as θ becomes larger.

Besides heat source, another factor which would affect temperature distribution within tips is

the geometrical shape. The tip geometry directly determines its thermal resistance. For the tip, its thermal resistance R_t can be expressed approximately as (neglecting the apex region) $\sin\theta \cdot [1/r - 1/(r + L\cdot\sin(\theta/2))]/[2\pi k\cdot (1 - \cos(\theta/2))]$ or $[1/r - 1/(r + L\cdot\sin(\theta/2))]/[2\pi k\cdot\tan(\theta/4)]$. It is easy to verify that the derivative of R_t on r is negative. Consequently, the thermal resistance decreases monotonically with the increasing tip radius r. Considering the fact that $1/r \gg 1/[r + L\cdot\tan(\theta/2)]$, it is obvious that when the cone angle becomes larger, the thermal resistance will go down quickly.

The dependences of peak apex temperature on the apex radius and cone angle are shown in Figure 3.15(a) and (b) for incident laser pulse energy of 2.0 mJ/cm^2 and 0.5 mJ/cm^2. The laser intensity enhancement near tip apex is also depicted. As r increases, the thermal resistance decreases, so heat is more easily dissipated in the radial direction, meanwhile, the laser intensity near the tip apex declines monotonously; both these factors would reduce the peak apex temperature, as presented in (a). In Figure 3.15(b), for r = 30 nm, the peak apex temperature decreases as the cone angle increases from 0° to 70°, which is similar to the results reported for aluminum-coated fiber tips [111,121]. However, the mean laser intensity features a different trend: it increases almost with θ linearly until θ = 50°, then keeps constant, only slightly declining when θ > 60°. When θ < 10°, the cone angle is the dominating factor that influences the temperature inside the tip, explain why the peak apex temperature drops abruptly down from 347.9 K to 314.1 K even though the mean laser intensity near the tip apex increases. As θ increases from 10° to 50°, the peak temperature decreases mildly due to compensation of the increasing mean laser intensity near the tip apex.

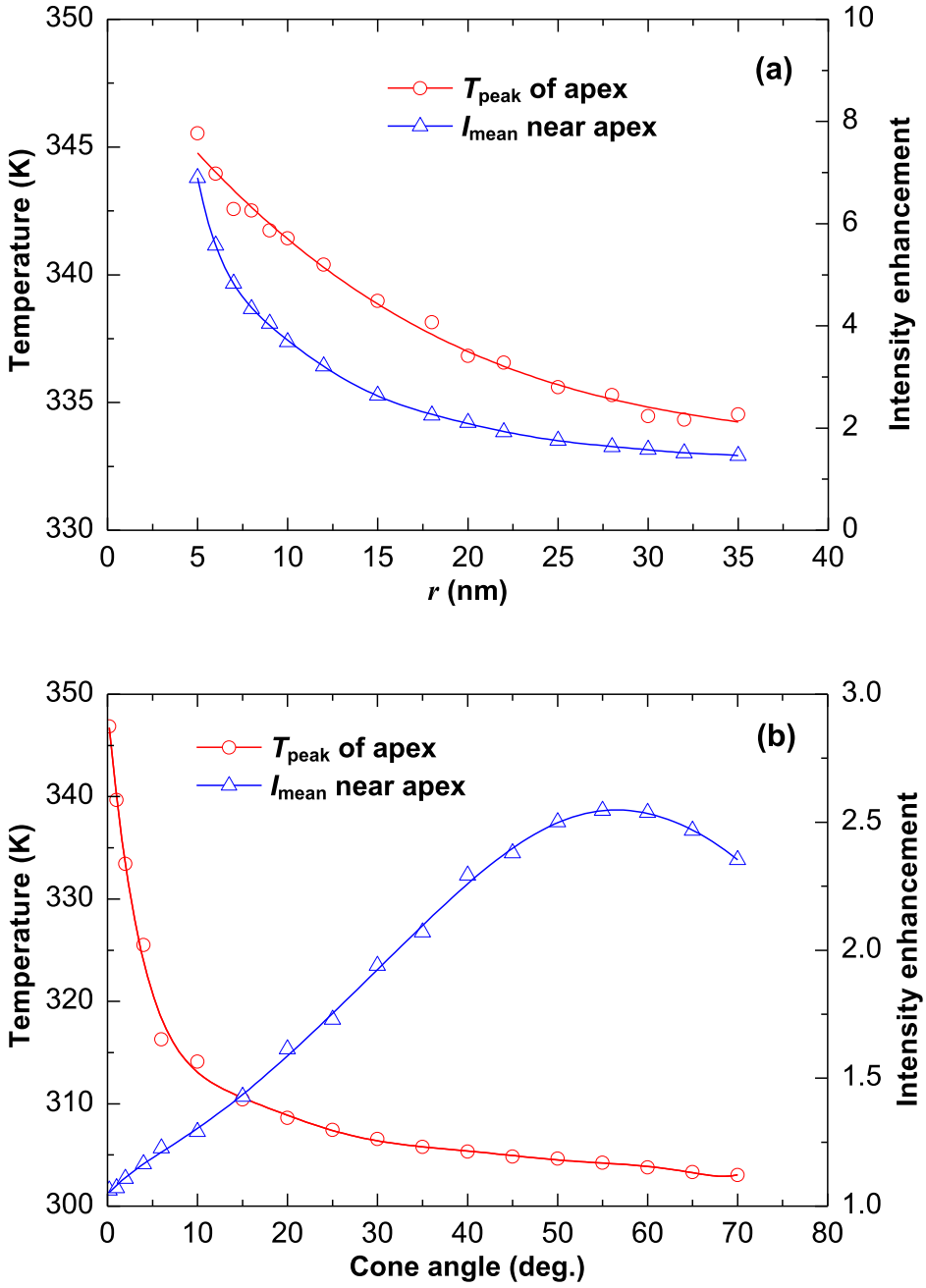

Figure 3.15 Peak temperature of apex and mean laser intensity near apex inside the tip versus (a) apex radius and (b) cone angle. Simulation conditions of (a): $\theta = 20°$, $d = 5$ nm, $\phi = 0°$, and $q'' = 2.0$ mJ/cm^2. Simulation conditions of (b): $r = 30$ nm, $d = 5$ nm, $\phi = 0°$, and $q'' = 0.5$ mJ/cm^2.

As θ increases further, similar to the phenomenon in Figure 3.15(a), both peak apex temperature and mean laser intensity near tip apex decreases. Another factor which cannot be ignored is the surface-area-to-volume ratio: γ, where the surface area is the projection area along the laser propagation direction. Since the laser energy is absorbed on the tip surface and propagates toward the core, the larger γ, the high temperature the tip would reach. For the conical tip, γ is approximately $3/\pi\cdot(2\eta + L)/(3\eta^2 + 3\eta L + L^2)$, where $\eta = r/\sin(\theta/2)$ The derivative of γ with respect to η is negative. When r increases, η will increase and γ will decrease. The decline of the peak apex temperature against the tip radius is the combined effect of γ, heat source and thermal resistance as shown in Figure 3.15(a). On the other hand, when θ increases, η decreases, and γ will increase. As a result, the temperature decline is offset somehow by the effect of γ and heat source, as shown in Figure 3.15(b).

In order to analyze the thermal effect of the substrate on the tip, the thermal contact resistance between them needs to be calculated. Take the tungsten tip with $r = 30$ nm, $\theta = 20°$, and $L = 16$ μm (typical length for commercial tip) for an example, its thermal resistance is $R_{tip} = 3.452 \times 10^5$ K/W. In general, the thermal resistance (per unit area) between hard interfaces in simple mechanical contact is in the order of 10^{-5} $m^2\cdot$K/W or higher. Therefore the thermal contact resistance between the tip and the substrate is estimated to be 10^{11} K/W if the tip is assumed having a flat top of 10 nm diameter. The real value could be even larger. This very high thermal contact resistance allows very little heat transfer between the tip and the substrate under vacuum condition. Therefore, the temperature distribution and evolution in the tip reported in this work does not consider the heat transfer effect of the substrate.

In our modeling, the tip radius is small, from 35 nm down to 5 nm. For tungsten at 300 K, its thermal conductivity is 174 W/(m·K), which is mostly contributed by electrons. Using approximated electron specific heat in the order of 2.1×10^4 J/(m^3·K) and electron speed ~10^4 m/s, and considering the strong energy exchange between electrons and lattice, the appearing mean free path of free electrons in tungsten is about 20 nm. Since the tip apex radius is smaller or comparable to this mean free path, it is expected in the apex region, the thermal conductivity of tungsten will be reduced accordingly. In the tip apex region, the characteristic thermal transport time (t_c) in the direction normal to the tip apex can be approximated as r^2/α where r is the tip radius and α is thermal diffusivity (6.83×10^{-5} m^2/s for bulk tungsten at 300 K). For a tip of 30 nm radius, the thermal conductivity in the tip region will have moderate reduction, and t_c is less than 1 ns. For smaller tips, even the thermal conductivity reduction is larger, considering the tip size has the second order effect on t_c, the local t_c will be even smaller. This explains why there is very little temperature gradient in the tip apex region as shown in Figure 3.12. Therefore, the thermal conductivity reduction in the tip apex region has negligible effect on the thermal transport studied in this work. On the other hand, situations will change if the tip is under ultrafast laser (picosecond or femtosecond) irradiation where the laser heating time is comparable to or smaller than the characteristic thermal transport time in the tip region.

3.4 Conclusion

In this chapter, the electromagnetic field was simulated in a tungsten SPM tip and silicon substrate system under laser irradiation. The electric field distribution around tip apex and

inside the tips had been analyzed. When the laser interacts with the metal tip, it is bent around the tip and concentrated under the apex, where extremely high field enhancement appeared. Field enhancement is mainly determined by the geometry of the tip-substrate system as well as their electrodynamic properties. As the tip-substrate distance increased, the peak field enhancement decreased exponentially. A shift of field peak position away from the tip-axis had been observed. This phenomenon vanished as the tip approaches the substrate. If the polarization direction of the laser is not parallel to the tip axis, only the component along the tip axis has contribution to the electric field enhancement under the tip apex. The optimum tip apex radius for field enhancement is about 9 nm when the cone angle is 20°. For a tip with fixed radius of 30 nm, field enhancement increased as the cone angle increased but was less than 50°. For cone angle in the range of 50° – 70°, the field enhancement kept pretty much constant. It decreased when the cone angle went beyond 70°. A small fraction of light had penetrated into the tip and dropped dramatically near the surface. The resulting temperature distribution was affected by two kinds of factors: heat source due to laser absorption, and the geometric shape of the tip. The peak apex temperature was used as a comparison parameter. As the polarization angle or apex radius increased, the peak apex temperature decreased. The peak apex temperature declined as the cone angle increased, even though the heat source provider — laser intensity inside the tip increased, revealing the strong effect of the cone angle on thermal transport.

CHAPTER 4. THERMAL RESPONSE OF SI NANO-TIP TO LASER IRRADIATION

Laser heated AFM tip can act as both thermal probe and thermal heating source in nanoscale thermal heating process. We report a study of laser heating of an ordinary AFM silicon tip under laser irradiation. The elevated temperature of the tip can be got from the relationship between Raman shift vs. temperature. The influences of focal position and energy flux level on the Raman shift have been discussed intensively. We substantiate our Raman measurement by theoretically modeling the electric field distribution as well as the heating processing through finite element method and a one-dimensional model, respectively.

4.1 Raman shift vs. Temperature

In the previous chapter, the thermal response of tungsten AFM tips under laser irradiation was systematically investigated as discussed in the previsous chapter. Temperature increases were calculated in the Tungsten tip. Due to the small dimension of the tip, it is hard to test the temperature locally during experiments through traditional temperature test methods. However, as the developing of Raman technology in nanoscale, as a non-contact temperature measure method, it is widely used to measure temperature at nanoscale. To our knowledge, experimental work for measuring heated tips due to laser absorption was mainly done through Raman spectroscopy [113,116,127]. Also, resonance frequency shift method was introduced to investigate the temperature of both AFM tip and cantilever under lateral laser illumination [113]. This latter one, though less accurate (actually, the measure temperature from resonance frequency shift method is the average temperature of the heated AFM tip and the cantilever), is amenable for practically all standard AFMs. In this chapter, Raman

thermometry is used to investigate the temperature rise of silicon AFM tip induced by the near-field laser heating. This method has been used successfully in our lab to measure a sub-10 nm scale on Si substrate temperature under a laser illuminated tip [51].

Raman thermometry as a non-contact temperature measurement method is extensively used for studying thermal transport in micro/nano structures, like CNTs [3,157], molecular junctions [158], GaAs nanowires [159], Silicon nanowires [160-163] and nanogranular silicon [164]. In Raman thermometry, as the temperature increases, the width broadens, and the peak position shifts toward lower frequency [161,165,166]. Both characteristics have been used to determine local temperature. The temperature can also be determined by Stokes/anti-Stokes intensity ratio which depends on temperature through the Bose-Einstein occupation number $I_{\text{anti-Stokes}}/I_{\text{Stokes}} \propto \exp(-\hbar\omega/k_{\text{B}}T)$ [116,127,158,165,167,168], if both of the Stokes and anti-Stokes peaks are available. Selection of these methods has been discussed elsewhere [51]. The material used in our experiment is Si, which can provide sharp peak signal. However, the intensity of the Raman signal is relatively low when only a small portion of the tip apex stays in the laser beam. As a result, the Raman shift method is chosen in the experiments.

The temperature dependent Raman shift for silicon material (including bulk material, nanowires and nanoparticles) has been studied thoroughly in the last 40 years [162,165,167-170]. The data for the relationship between Raman shift and temperature is available for Si. Consequently, we Si AFM tips other than tungsten tips are used in the experiment in this chapter. Balkanski *et al.* [167] presented a theoretical model of Raman frequency vs.

measured temperature from 5 to 1400 K, using three- and four-phonon processes. It can be inferred that linear regress is closely satisfied from room temperature to 600K. Table 4.1 shows the linear relationship between the Raman shift and temperature for both bulk silicon and silicon nanowires reported by many groups. Although the relationships between the temperature and Raman shift for bulk Si and Si nanowire are the same [170] or of little discrepancies [162], the dependence of Raman shift on temperature is highly different. McCarthy *et al*. [116] observed redshift between the Raman shift from bulk Si and Si tip, due to the geometry of the sharp tip. Tarun *et al*. [127] also reported a Raman shift vs. temperature curve for lateral laser heating Si tips, and the data is a little larger than that obtained by McCarthy *et al*. [116].

Table 4.1. Some experimental determinations about temperature dependence Raman spectra of Si.

Researcher	Temperature range (K)	Si morphology	Slope (cm^{-1}/K)
Yue *et al.* [51]	300 – 503	Bulk	–0.022
Hubert *et al.* [164]	295 – 900	Bulk	–0.0247
Doerk *et al.* [170]	293 – 593	Bulk Nanowire	–0.022
Khachadorian *et al.* [162]	272 – 700	Bulk	–0.0229
	272 – 873	Nanowire	–0.0236

In laser-assisted tip-based experiments, the highly focused laser beam size, usually as small

as several micrometers [113], is comparable to the size of the tips, so focusing is of great importance. It is hard to control the interaction between the laser and tip during experimental work. To our best knowledge, little experimental investigations have been reported on how the extremely focused laser beam irradiates different spots of the relatively long AFM tip, which can provide guidance for experimental work. In this work, experimental examination is done to observe the how the thermal response changes when the laser illuminates the different spot of the tip with different laser power.

4.2 Experimental Setup

Figure 4.1(a) sketches the schematic of the experimental setup. The experimental Raman microscope system consists of confocal Raman spectrometer (Voyage^{TM}, B&W Tek, Inc.) and microscope (Olympus BX51). The spectral resolution of the Raman system is $1 - 2$ cm^{-1}. An ordinary AFM silicon tip which is mounted on a 3-dimentional piezo-actuated nano-stage is allocated under the focal spot of the laser beam from the Raman spectrometer. The tip axis is horizontal and along the *y*-axis of the nano-stage. The cantilever is along the *x*-axis; and the laser is incident vertically along the *z*-axis. The movement range of the nano-stage is 20 μm (with some combination with a 1-dimensional piezo-acturated nano-stage, the range in the *y*-axis direction is 40 μm), with a resolution of 20 nm in each direction. The whole system is placed in air.

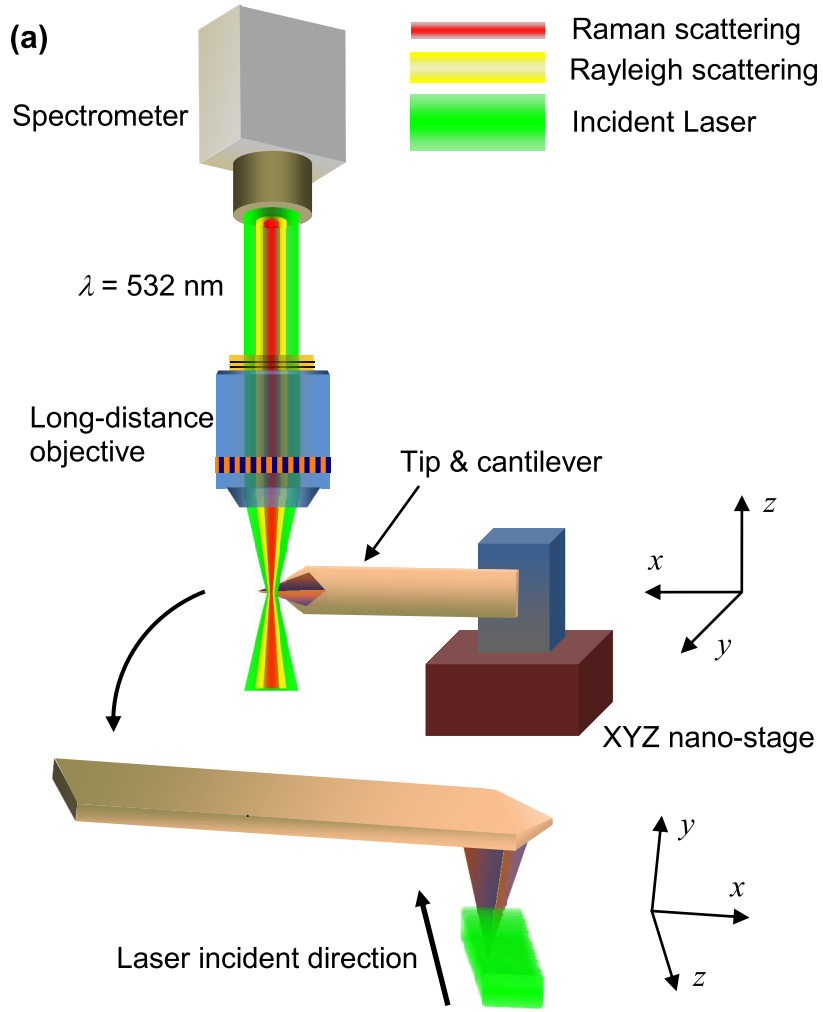

Figure 4.1 (a) Schematic of experimental setup (not to scale). An ordinary AFM silicon tip which is set on a 3-dimentional piezo-actuated nano-stage is allocated on the focal spot of the laser beam from a Raman spectrometer. The tip axis is horizontal and along *y*-axis. The cantilever is along the *x*-axis. The laser is incident vertically from *z*-axis. The range of the nano-stage is 20 μm, with resolution of 20 nm. (b) Configuration of the laser beam at the focal spot when the laser illuminates the side surface of tip. The spot size of the incident laser is 10.0 μm along the major axis (*x*-axis), and 2.8 μm along the minor axis (*y*-axis). The laser beam is polarized with the strongest intensity along the *x*′-axis is twice of that along the *y*′-axis, where the *x*′- or *y*′-axis has an 45° angle with respect to the major axis or minor axis, (c) Laser spot moving directions with respect to the tip during experiment.

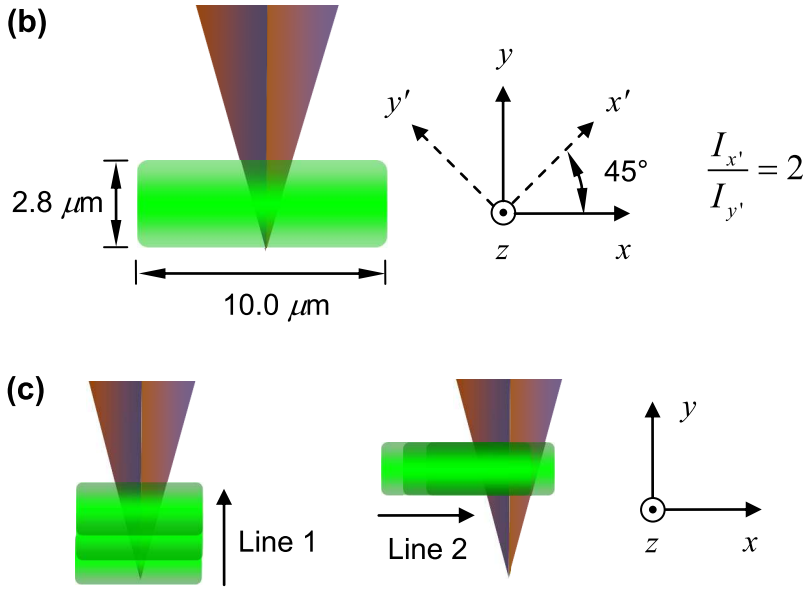

Figure 4.1 Continued

The laser beam is focused through a 20× microscope objective (NA = 0.40, WD = 12.0 mm). The beam size is 2.8 × 10.0 μm^2 at the focal spot as shown in Figure 4.1(b). The laser beam is partially polarized along the x' and y' directions as shown in Figure 4.1(b). The nano-stage is aligned to make sure that the laser is incident from the z-direction, the main axis of the laser spot is along the x-direction, and the minor axis is along the y-direction. Consequently, the tip axis is perpendicular to major axis of the laser spot. In such a case, the tip axis has an angle of 45° with respect to direction in which the polarized laser has the strongest intensity.

The laser with wavelength of 532 nm is used as both Raman probe and heat source. The optical trace is also shown in Figure 4.1. The incident laser from the Raman spectrometer is focused on the tip under the objective lens. The excited Raman scattering signal and Rayleigh scattering signal are collected by the same objective in the backscattering mode: it

sends the scattered radiation backwards to the spectrometer. To investigate the heating effect caused by laser, the tip is illuminated with different laser power of 4, 7, 12,7 and 15.9 mW, corresponding to energy fluxes of 5.6×10^8, 4.5×10^8, 2.5×10^8 and 6×10^8 W/m^2, respectively. All Raman spectra are measured using an integration time of 10 s, unless otherwise stated.

Single crystal silicon (antimony doped) tip (CSG10, K-Tek nanotechnology) is used in the experiment. Figure 4.2 shows the SEM image of the AFM tip. It clearly shows that the shape

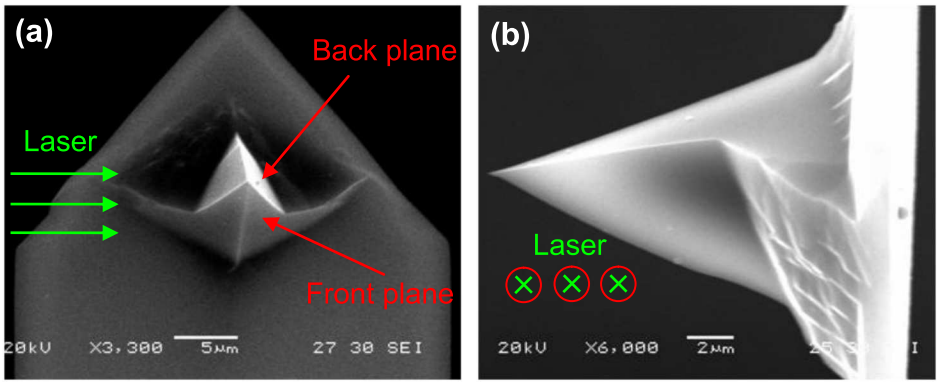

Figure 4.2. (a) top-view and (b) side-view SEM images of the AFM tetragonal pyramid tip. The thickness of the cantilever is 2.67 μm, and the height of the tip is 15.37 μm. The front plane angle 10°, the back plane is 30°, side angle is 36° (the front/back plane angle is the angle of projection of the front/back plane from side-view, and the side plane angle is the angel of the projection of front/back plane from front/back-view). The last 500 nm from tip apex is conical with cone angle of 10°. The apex radius is 10 nm.

of tip is tetragonal pyramid. The thickness of the cantilever is 2.67 μm, and the height of the tip is 15.37 μm. The front plane angle is 10°, the back plane is 30°, and side angle is 36°. The last 500 nm from tip apex is conical with a cone angle of 10°. The apex radius is 10 nm.

According to the dimensions of the tip, the laser spot can approximately fully cover the tip through apex to the base in the direction perpendicular to the tip axis. However, compared to the tip length, the laser width can only partially cover the tip, as shown in Figure 4.1(b).

4.3 Experimental Results and Discussions

In order to analyze the thermal response of the tip under laser illumination by Raman shift method, the temperature dependence of the Raman shift of Si tip is needed. Even plenty of results of the relationship between the temperature and Raman shift have been reported for bulk Si as well as Si nanowires introduced above, these results would not suitable for the Si tip due to discrepant geometries. Balkanski *et al*. [167] gave a theoretical calculation equation of the peak position $\omega(T)$ vs. temperature for bulk Si as

$$\omega(T) = \omega_0 + C\left(1+\frac{2}{e^x-1}\right) + D\left(1+\frac{3}{e^y-1}+\frac{3}{(e^y-1)^2}\right), \tag{4.1}$$

where ω_0 is Raman frequency at 0 K with a value of 528 cm^{-1}, C and D are anharmonic constants corresponding to three- and four-phonon processes with the values of –2.96 cm^{-1}, and –0.174 cm^{-1}, respectively. While $x = \hbar\omega_0/2k_BT$, and $y = \hbar\omega_0/3k_BT$, where $\hbar$ is reduced Planck's constant, k_B Boltzmann constant. To make it suitable for heated AFM tip, McCarthy *et al*. [116] revised this anharmonic model by doubling of four-phonon nonlinear effects (i. e. D = –0.348 cm^{-1}), and proved it fits the relationship between Raman shift and temperature of laser-heated Si AFM tips. The temperature was measured from anti-Stokes/Stokes. Tarun *et al*. [127] also measured the Raman shift and temperature of Si tip heated by lateral incident laser and found the result can be approximately fitted by the model used by McCarthy *et al*. [116], though the experimental results are a little higher. The curves for both theoretical

models are shown in Figure 4.3. To make these curves suitable for the experiments data here,

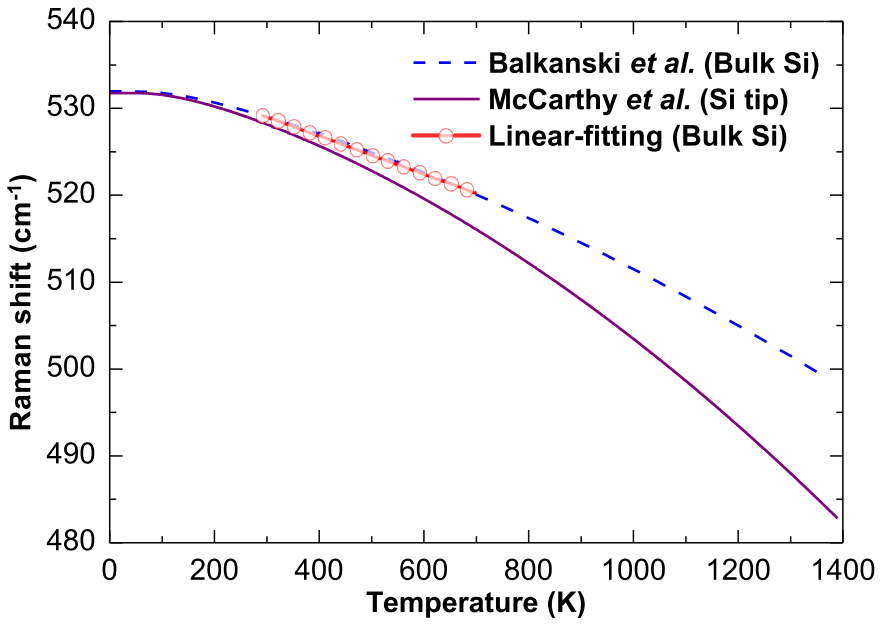

Figure 4.3 Temperature dependence of the Raman shift for bulk Si (dashed line and red circles) and Si AFM tip (solid line), obtained from the calculations of Balkanski [167] **and McCarthy** [116]**, and linear fitting with a slope of –0.022 cm^{-1}/K. The dashed curve represents the model using both three- and four-phonon processes. The solid curve is revised based on the Balkansik's model by doubling of four-phonon nonlinear effects, making it suitable for tip geometry. To make curves suitable for the experiments data here, the initial values of the theoretical models is reset compared to the original ones.**

the initial values of the theoretical models is reset compared to the original ones, i. e. ω_0 = 535 cm^{-1}. This value is determined by making the curve calculated by Balkanski *et al*. [167] go through the point (298 K, 529.05 cm^{-1}), measured on bulk Si at room temperature. For comparison, the linear fitting between temperature and Raman shift from bulk silicon with slope of –0.022 cm^{-1}/K is also shown in Figure 4.3. It indicates that the line for the linear relationship from room temperature though 700 K for bulk Si is almost overlapped with the

Balkanski's anharmonic model.

The temperature rises of the AFM tip are measured by the Raman shift and the temperature is obtained through the theoretical calculation introduced by McCarthy *et al*. [116]. The results are fully reproducible, over five replications of each measurement were performed, and one representative result (curve) is chosen for each, as presented from Figure 4.4 to Figure 4.7. From Figure 4.5 to Figure 4.7, the temperature axis is calibrated according to the relationship between the Raman shift and temperature in Figure 4.3, and as a result, it is not linear.

In analysis of Raman spectrum, due to the resolution limit of the Raman spectrometer, the peak position is determined by Gaussian function fitting, which is consistent with our calibration [51]. Figure 4.4 shows selected spectra for situations that the laser beam laterally irradiates AFM tip and cantilever [as shown in Figure 4.2(b)], and vertically irradiates on bulk Si, respectively. In order to keep the height of the spectrum for the Si substrate comparable to others, 5 seconds of integration time other than 10 seconds is used in the Raman measurement. The Raman shifts are 514.20, 518.70 and 529.05 cm^{-1}, respectively for the 3 peaks. We attribute the change of the spectral changes to laser heating. The corresponding temperature of the Si substrate is considered as room temperature, 298 K. The temperatures of the tip and cantilever are 749 K and 626 K, respectively.

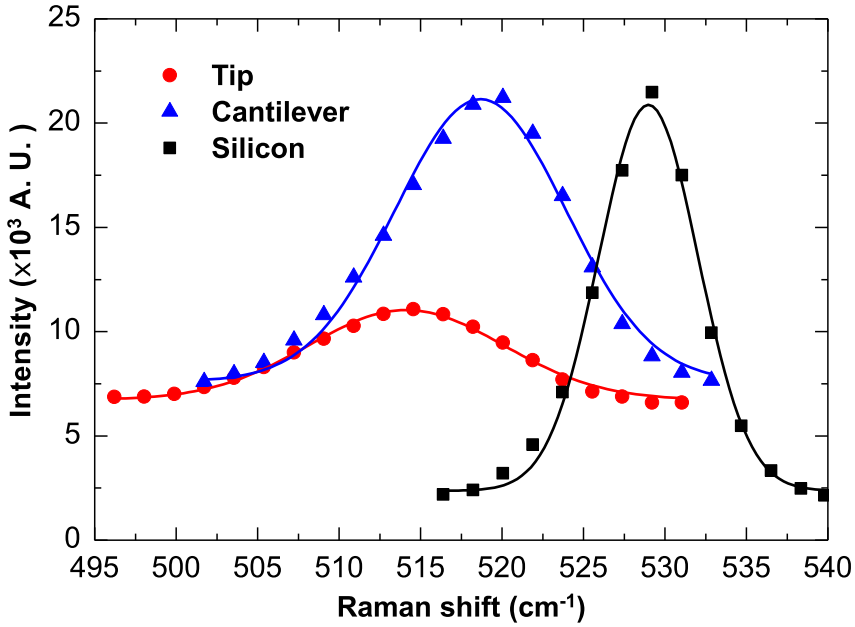

Figure 4.4 Raman shift when the laser illuminates the side surface of tip, side surface of cantilever, and bulk silicon, respectively. In order to keep the height of the spectrum for the Si substrate comparable with others, 5 seconds integration time other than 10 seconds is used in the Raman measurement.

In our experiment, the focusing has significant effect on the experimental results, as the dimension of the laser beam at the focal spot and that of the tip are comparable. In Figure 4.5, the laser beam illuminates the center of the lateral surface of the tip, as shown in the joint point of Line 1 and Line 2 in Figure 4.1(c). The 3-dimensional nano-stage is adjusted along the z-axis to change the position of the tip around the focal spot. The total travel distance is about 17 μm, covering the focal spot (z = 0 μm). The focusing situation is monitored by the diffraction image under the tip, to ensure a reliable and reproductable focusing alignment. When the tip moves upwards (below the focal spot) approaching the focal spot, erect image can be observed under the tip. As the tip moves upwards, the image zooms out. When the tip

is in the range of ±2 μm of the focal spot, image disappears, because the laser beam is blocked by the tip. As the tip moves upwards further, reversed image appears.

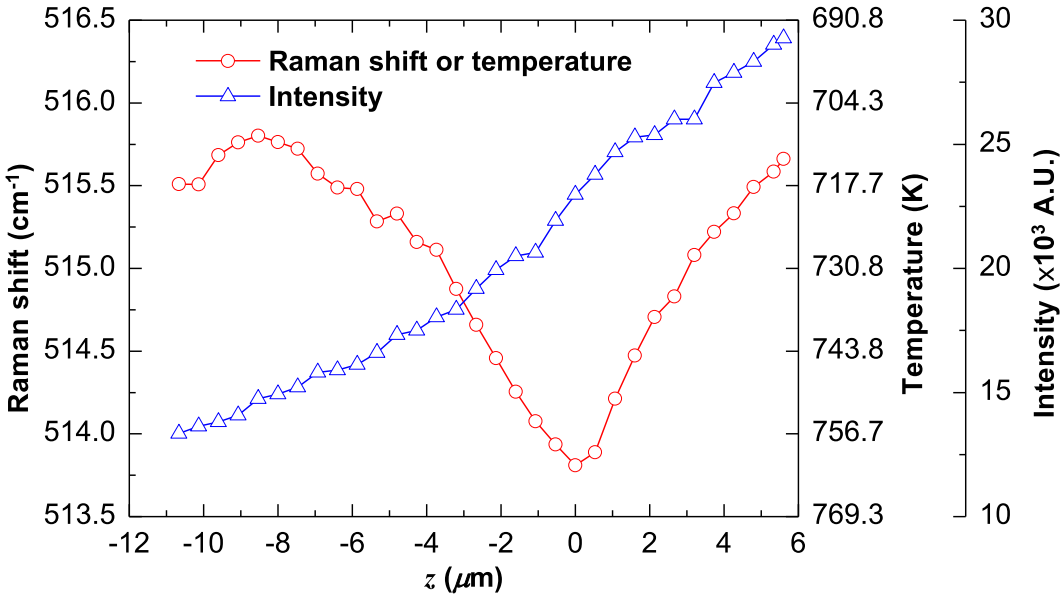

Figure 4.5 Raman shift and Raman intensity when the laser beam scans along the *z*-axis. The tip moves upwards in the vicinity of focal spot.

During the travel of the tip, when the tip is over 8.5 μm lower than the focal spot (z < –8.5 μm), the Raman shift increases as the tip approaching the focal spot, correspondingly, the temperature decreases. In this process, the further the tip is away from the tip, the larger area of the tip is covered by the laser beam. Consequently, more energy is absorbed by the tip, which in turn results in more temperature rise. When the tip is less than 8.5 μm below the focal spot (–8.5 μm < z < 0 μm), the Raman shift decreases (temperature increases) as the tip is closer to the focal spot. When the tip gets over the focal spot (z > 0 μm), the Raman shift increases (temperature decreases) as the tip is away from the focal spot. When the tip moves

upward, it is closer to the objective lens, as a result, the collection angle is larger, and more Raman signal is gathered.

Figure 4.6 shows how the Raman signal intensity and Raman shift (temperature) changes

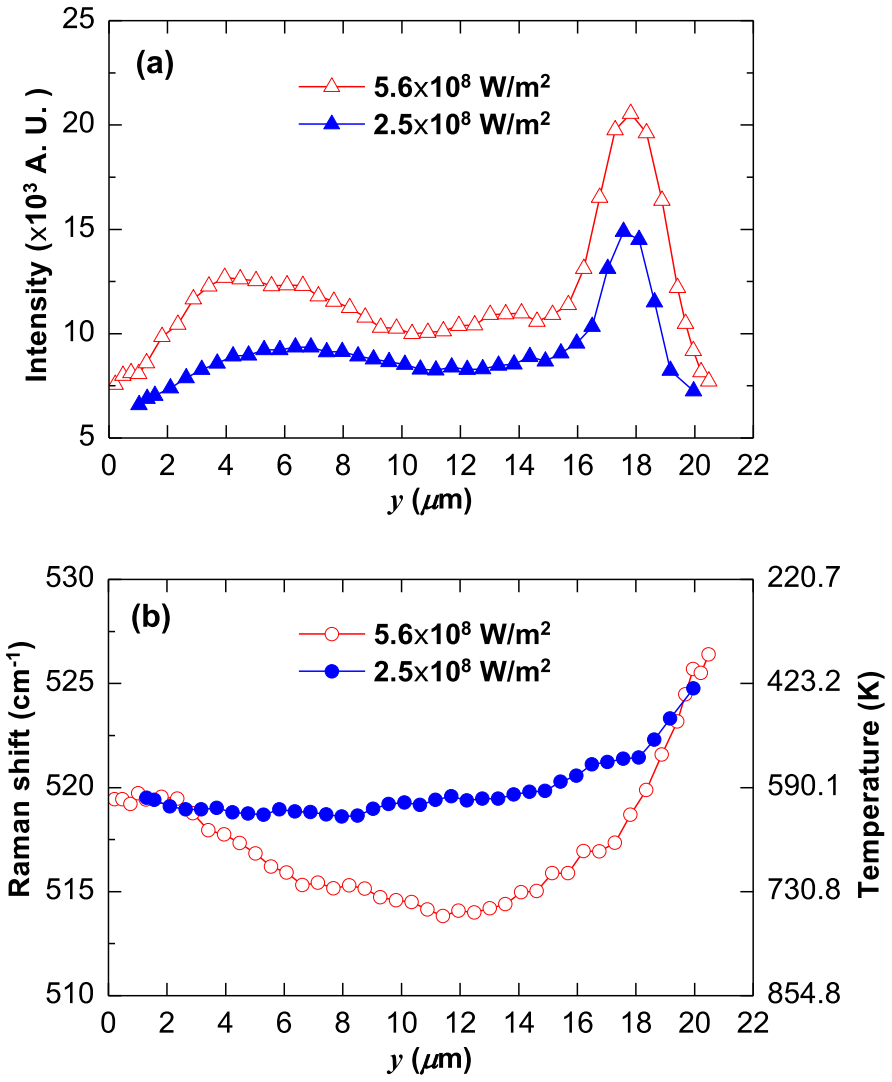

Figure 4.6 (a) Raman intensity and (b) Raman shift along Line 1 [as shown in Figure 4.2(b), in *y*-axis direction] under energy fluxes of 5.6 × 10^8 and 2.5 × 10^8 W/m^2, respectively. The tip moves along the tip axis at the focal spot.

while the illuminating laser beam moves along the tip axis [parallel to Line 1 in Figure

4.1(c)]. First, the situation for energy flux of incident laser is 5.6×10^8 W/m^2 is considered. When the laser spot begins to contact with the tip apex, Raman signal emerges. At first, however, only a small part of the laser illuminates the tip, the Raman signal intensity is very low, and the Raman shift is too weak for proper fitting to find the peak position. When the tip entered into the laser beam for about 1.6 μm, at $y = 0$ μm in Figure 4.6, an obvious Raman peak is observed. The Raman shift is approximately 519.5 cm^{-1}, and the temperature is 603 K, as shown in Figure 4.6(b) depicted by red open circles. Since the width of the laser spot along the tip axis is 2.8 μm, it can be judged that over half of the laser beam irradiates the tip apex and generates the obvious Raman peak signal.

As the laser moves further towards the base of the tip, i.e. from $y = 0$ μm to $y \approx 15.5$ μm, the Raman shift decreases gradually from 519.5 cm^{-1} to 514.0 cm^{-1} when 0 μm $< y <$ 11.5 μm, and increases to 515.0 cm^{-1} when 11.5 μm $< y <$ 14 μm, indicating the temperature increases from 603 K to 754 K, then declines to 728 K. This is the trade-off between the increasing of laser absorbing area and the increasing heat conduction to the base of the tip even the cantilever. When the laser beam scans along the tip axis, the larger area of the tip is under laser illumination, the more electromagnetic energy is absorbed to convert into heat. On the other hand, the closer the laser is to base of the tip, the easier the heat is conducted away into the cantilever, which can be considered a heat sink. Meanwhile, as the laser is away from the tip apex, the field enhancement effect becomes weaker, the laser intensity around the tip, which in turn will decide the laser absorption inside silicon tip, will inevitably decline.

The curve of Raman signal intensity is affected by both size of the laser-tip interaction area and the heating situation. As the area of the laser illumination increases, the Raman signal intensity increases, as shown for $y < 4$ μm in Figure 4.6(a). On the other hand, when 4 μm < $y < 10.5$ μm, the Raman signal intensity decreased so obviously. When the temperature increases, the state density of phonons will increases, consequently, the phonons will have a higher energy. This will induce a reduction of intensity of Stokes scattering [161]. On the other hand, the intensity of Stokes Raman peak is proportional to $n(\omega) + 1$, where $n(\omega) = [\exp(-\hbar\omega/k_B T) - 1]^{-1}$ is Bose-Einstein distribution function, or called thermal occupation number [171]. Under this condition, the intensity of the Stokes Raman scattering drops when the temperature rises. This effect has also been observed in silicon substrates under illuminated AFM tip our previous work [51], and silicon nanowoires [161]. For 10.5 μm < $y < 14$ μm, under the combined effects of decreasing field enhancement effect, increasing illumination area and increasing heat conduction, the Raman intensity keeps increasing slowly.

When $y > 14$ μm, the laser beam irradiates on the cantilever. The arch of the curve for the Raman intensity in Figure 4.6(a) can clearly show interaction between laser and the cantilever. The thickness of the cantilever is 2.67 μm, and the dimension of the laser is 2.8 μm, on the left side of the peak position (14 < $y < 18$ μm), the laser is still partially in contact with base of the tip. Due to fact that the intensity signal from the tip is much lower than that from the cantilever, the signal partially from the tip does not affect of the symmetry of the intensity signal. Nevertheless, the story is different for the Raman shift. While the laser beam

goes across over the side face of the cantilever, the Raman shift increases.

When the energy flux takes 2.5×10^8 W/m^2, the trend of the curve for Raman intensity is the same as but lies consistently below that under energy flux of 5.6×10^8 W/m^2. And the Raman shift keeps consistently higher or temperature keeps consistently lower for low energy flux, except when the laser irradiates the tip apex and the cantilever as shown on both ends of the curves in Figure 4.6(b), where the Raman shit is not sensitive to the energy flux. When the laser irradiates the foremost end of the tip ($y < 3$ μm), only a small area of the tip is exposed to the laser beam. The heat in the tip apex is readily transported to the blunt end of the tip. Although the energy flux increases from 2.5×10^8 W/m^2 to 5.6×10^8 W/m^2, the temperature is kept constant at approximately 600 K. When the laser irradiates the cantilever, the heat is readily dissipated along the cantilever, consequently, increasing the energy fluxes does raise the temperature of the cantilever when the laser is just on the center of the cantilever ($y \approx 18$ μm), the Raman shift is smaller and the temperature is higher for higher energy flux. However, when the laser irradiates the edge of the cantilever (opposite side of the tip apex), only a small area of the cantilever is covered by the laser, as a result, the absorbed heat is transferred quickly, the Raman shift or temperature is much less sensitive to energy flux. This phenomenon is similar to the situation when the laser irradiates bulk Si, which will be analyzed in the following. Overall, the change of the Raman shift/temperature is mild for low energy flux. It experiences an almost plateau for $y < 8.5$ μm, and increases/decreases gradually for $y > 8.5$ μm.

To investigate the local heating effect by the laser irradiation, Raman scattering was

performed with different laser power. Figure 4.7 shows the Raman signal, Raman shift and

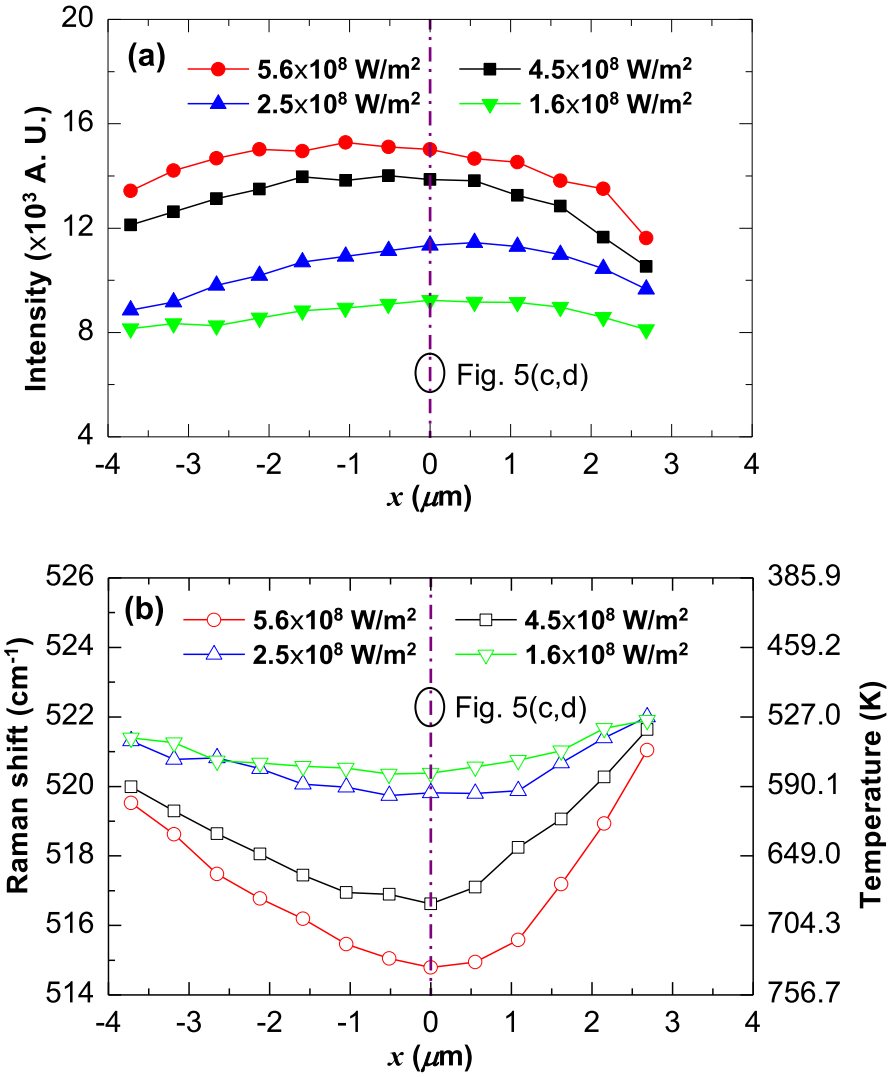

Figure 4.7 (a) Raman intensity and (b) Raman shift along Line 2 [as shown in Figure 4.1(b), in the *x* direction] under energy fluxes of 5.6 × 10^8, 4.5 × 10^8, 2.5 × 10^8 and 1.6 × 10^8 W/m^2, respectively. The tip moves perpendicularly to tip axis. (c) Raman shift and Raman intensity vs. energy flux. The Raman shift of bulk silicon is also shown in the figure (green open squares). (d) Raman peak under different energy fluxes.

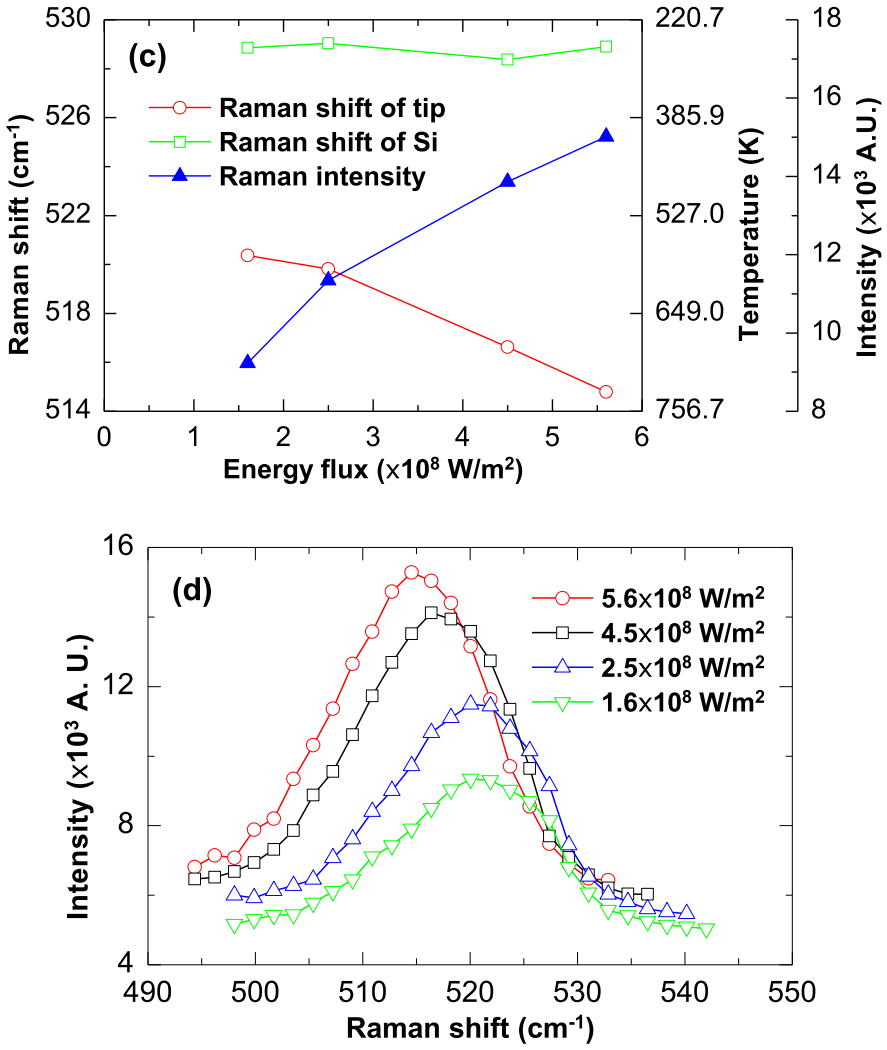

Figure 4.7 Continued

temperature when the laser beam scans perpendicularly to the tip axis across the middle of the tip [Line 2 as shown in Figure 4.1(c)] under energy fluxes of 5.6×10^8, 4.5×10^8, 2.5×10^8 and 1.6×10^8 W/m^2, respectively. The width of the tip along Line 2 is approximately 7 μm. To ensure high quality signal, the data for the laser beam irradiating the edge of the tip are neglected.

The Raman signal intensity is shown in Figure 4.7(a). Within expectation, the Raman

intensity is stronger for higher energy fluxes, and the intensity is stronger in the center compared with that in both sides, even though not clearly sensitive to the position. Figure 4.7(b) indicates that higher energy flux gives rise to lower Raman shift signal, and induces higher temperature rise. For each curve corresponding to a certain energy flux, when the laser moves away from the center to either side, the Raman shift/frequency increases, and the temperature of the tip decreases. In order to investigate the influence of the energy fluxes on the signals when the laser illuminates the same spot under different energy fluxes, the signals from the center spot of the lateral surface on the tip [the joint point of Line 1 and Line 2 in Figure 4.1(c), corresponding to $x = 0$ μm in Figure 4.7(a, b)] is presented, as shown in Figure 4.7(c). The Raman signal intensity increases as the energy flux goes up. As expected, when the energy flux of the incident laser increases, more energy will be absorbed, the temperature of the tip also increases, which is also reflected by the decreasing Raman shift as depicted by the red open circles. The same trend for Raman shift was also observed on AFM tips [113,116], silicon nanowires [160,163] and nanogranular silicon films [168]. The Raman shift of bulk silicon is also shown for comparison in Figure 4.7(c) (green open squares). The energy fluxes in the range of $1.6 \sim 5.6 \times 10^8$ W/m^2 on the tip has significantly modified the Raman spectra of the tip, however has no effect on bulk silicon, even the density is as high as 4×10^9 W/m^2 [160] or 13.73×10^9 W/m^2 [163]. The decrease of Raman shift, or temperature rise as the input energy increases is attributed to low thermal conductivity of silicon in nanostructure [128] and the small scattering volume, as the cantilever is the only effectively way for the heat to be transferred away. For bulk silicon, the heat generated due to laser absorption is quickly dissipated in three dimensions, and room temperature is maintained during Raman measurements. However, it is worth mentioning that when the input energy is

rather low, saying 3×10^4 W/m^2, the situation would be different, the increasing power of incident laser has no significant effect on the Raman shift when the laser is incident on silicon nanowires [161]. Owing to low quality of the Raman peak under low energy fluxes, saying, $< 1.6 \times 10^8$ W/m^2, no experimental data is available within this energy fluxes range.

The Raman spectra corresponding to Figure 4.7(c) are shown in Figure 4.7(d). Obviously, the Raman shift/frequency decreases, the temperature increases and the Raman signal intensity increases as the energy flux increases. It has been analyzed in Figure 4.6 that the rising temperature/decreasing of Raman shift will reduce the Raman scattering intensity. Thus, it can be inferred that the increasing intensity due to the increasing energy flux has already been partially offset by the effect induced by rising temperature.

4.4 Theoretical Analysis

In order to analyze the mechanism of temperature rise in the silicon tip, numerical calculation of the electromagnetic field enhancement is conducted. The phenomenon of electromagnetic field enhancement around a sharp tip has been theoretically studied over years. In this work, the finite element method (FEM) [31,99-104] which has its merits in solving complex geometries is employed to calculate the electric field distribution around as well as inside the tip.

The modeling is performed by using High Frequency Structure Simulator. A conical Si tip whose sharp end is tangent to a hemisphere is investigated in this work. Though the geometry of the tip used in the experiment is tetragonal pyramid, however, at least the last 500 nm

from the apex is conical. Therefore, the conical tip model (length L = 600 nm, cone angle θ = 10°, apex radius r = 10 nm) is adopted. Maxwell's equations are solved across a defined rectangular computational domain with dimensions of 750 nm × 750 nm × 850 nm: containing the tip and vacuum around the tip. Absorbing (radiation) boundaries which balloon the boundaries infinitely far away from the structure is applied for the domain. A plane wave polarized along the tip apex is incident horizontally (perpendicular to the tip axis); and the electric field amplitude of the wave is set to 1 V/m. More details about the simulation can be found in chapter 3.

Figure 4.8 shows how the electric field is distributed around/inside the tip. It is obvious that the electric field is enhanced and confined around the tip. The strongest electric field with a magnitude of 5.19 V/m appears just under the apex. For the electric field inside the tip, due to high absorption of laser for Si, the maximum field enhancement is as high as 2.14, which is higher than that in tungsten tip, which is about 1 according to the previous simulation in chapter 3. In Figure 3.4(b), it clearly demonstrates that the electric field in the center is stronger than that close to the surface, in contrast to the field distribution inside the tungsten tip (as shown in Figure 3.4). For metal, the skin depth is relatively short than dielectric materials. For example, the skin depth of tungsten and silicon at λ = 532 nm are δ_W = 31.1 nm ($\delta = \lambda/2\pi\kappa$, κ is the extinction coefficient), and δ_{Si} = 1.64 μm, respectively. For the tungsten tip, the skin depth is far less than the dimension of the tip except at the apex. Consequently, the laser is only absorbed near the surface of the tip. And attenuation from the surface is observed. Adversely, the skin depth of Si is much larger than the width of the tip, the laser has penetrated through the tip. Moreover, the laser in the Si tip will reflect back and

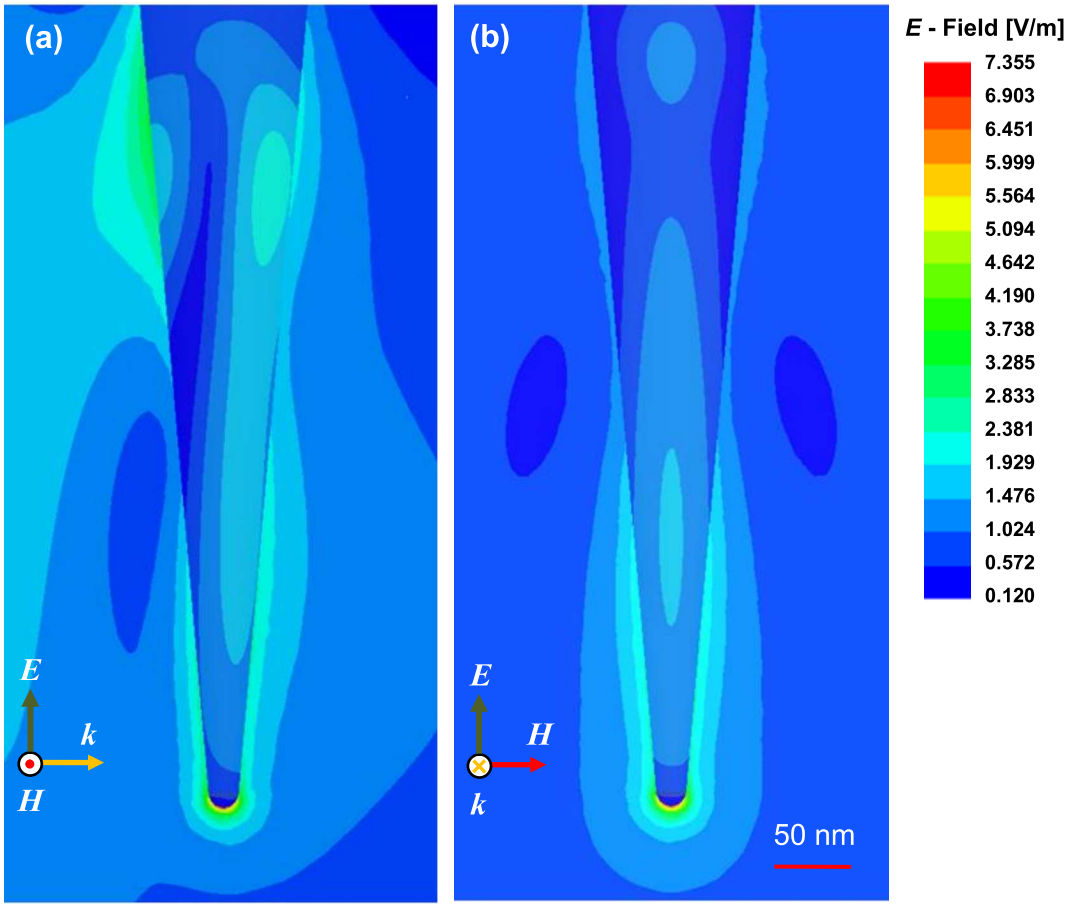

Figure 4.8 Field enhancement around the tip (a) side view (b) front view. The maximum electric field intensity is 2.14 V/m for the incident electric field intensity of 1 V/m. The electric field amplitude of the scattered light is equal to the field enhancement value, which is defined as the ratio of scattered to incident field amplitude.

forth inside the tip when it encounters the surface, the light is trapped in the geometry as in Al coated fiber for aperture NSOM [107,108]. In the apex, though the electric field is high enough outside, the electric field inside is relatively low. Near the apex zone, the surface of the tip exposed to the incident laser is smaller than that of the blunt zone. As a result, the total absorbed laser energy is relatively less in this zone. This explains why the strongest electric field inside the tip is not at the apex.

With the knowledge of the electric field distribution inside the tip, the heat generation rate per unit volume can be calculated from $\dot{q} = I\beta$, where I is the laser intensity inside the tip, and β is the absorption coefficient, which is related to the extinction coefficient, κ, by $\beta = 4\pi\kappa/\lambda$. The laser intensity inside the tip equals the Poynting vector, $I = P = 0.5c\varepsilon_0 nE^2$. Here E is the time-average intensity of the electric field, c is the light speed in free space as 3×10^8 m/s, ε_0 the vacuum permittivity and n (= 4.15) the refractive index of Si.

To analyze the thermal response of the tip under laser irradiation, a one-dimensional heat transfer model is used. As mentioned above, at the sharp end, the tip is a 500 nm conical apex with apex radius 10 nm and transitionally turns into a tetragonal pyramid base. In the heat transfer model, for simplicity, a 600 nm long conical with apex radius of 10 nm is connected to a tetragonal pyramid, no transition is considered. Obviously, the thermal resistance for both ends should be computed separately with the same equation $\int dl/A_c k$, where A_c is the cross-section area, and k is local thermal conductivity, as schematic model of the tip is shown in Figure 4.9. The whole tip is divided into thin layers, each layer is considered isothermal. For the tetragonal pyramid part, if the layer is irradiated by laser, the absorbed energy is $\alpha I A_s$, where A_s is the projection area exposed to laser, I the incident laser intensity, and α absorption ratio. In the conical zone, due to small geometry, near-field heating is considered. The integration $\int_{\text{conical}} \beta I_{\text{tip}} dV$ represents the power absorbed by the tip, where I_{tip} can be expressed in term of electric field inside the tip E, the latter is calculated in HFSS simulation. Considering the Poynting vector can be integrated over the surface of

the conical tip in the HFSS model, and the net result of the integration is just the power absorbed by the tip, thus, it is a convenient alternate. The temperature in the hemispherical apex is considered as uniform in the heat transfer model.

The effects of small geometry and temperature on the thermal conductivity have been considered during the calculation. The thermal conductivity of the tip will be reduced due to its small geometry. Thermal transport is sustained by collisions among energy carries. In silicon, phonons are the dominant energy carriers, despite the presence of certain amount of free charge heat carriers. The thermal conductivity in kinetic theory is given as

$$k = \frac{1}{3} C v l_{\text{eff}}, \tag{4.2}$$

where C is the specific of the phonons, v is the average phonon speed, and l_{eff} effective mean-free path, and it is determined by [172]

$$\frac{1}{l_{\text{eff}}} = \frac{1}{\Lambda_{\infty}} + \frac{1}{d_{\text{c}}}, \tag{4.3}$$

where Λ_{∞} is the temperature-dependent phonon mean free path in bulk materials [173], d_{c} the diameter of the structure, for the tip, d_{c} equals the diameter of the cross-section perpendicular to the tip axis. For simplicity, we choose $Cv = 1.68 \times 10^9$ W/m^2 K, neglecting the contribution of the optical phonons to the specific heat, since the optical phonons have little contribution to heat transfer [173]. Since the temperature-dependent of $k(T)$ is known for bulk Si [174], as a result, the temperature-dependent phonon mean free path for bulk Si is $\Lambda_{\infty}(T) = 3k(T)/Cv$, when $d_{\text{c}} \rightarrow \infty$. Substitute $\Lambda_{\infty}(T)$ into equation (3), then into equation (2), the temperature/geometry dependent thermal conductivity of Si is acquired.

The steady state temperature distribution along tip axis is shown in Figure 4.9. It shows that the temperature at the tip apex is 448 K. The measured temperature at the apex under 5.6 × 10^8 W/m^2 is ~600 K. Our first-order thermal analysis agrees well with the measurement results. The difference between them could be due to the tip geometry variation and reduction of Si tip thermal conductivity. The silicon tip is *n*-doped with antimony at concentration ranging from 1 to 5 × 10^{18} ions/cm^3. The impurities and additional free carriers in doped silicon will reduce the thermal conductivity compared to the value of pure bulk silicon [175] and in films [176-178] correspondingly. A loss in thermal conductivity of 18% due to higher doping (1 × 10^{19} ions/cm^3, *n* or *p*-type) was reported [179]. Therefore, the temperature acquired in the model is underestimated to some extent.

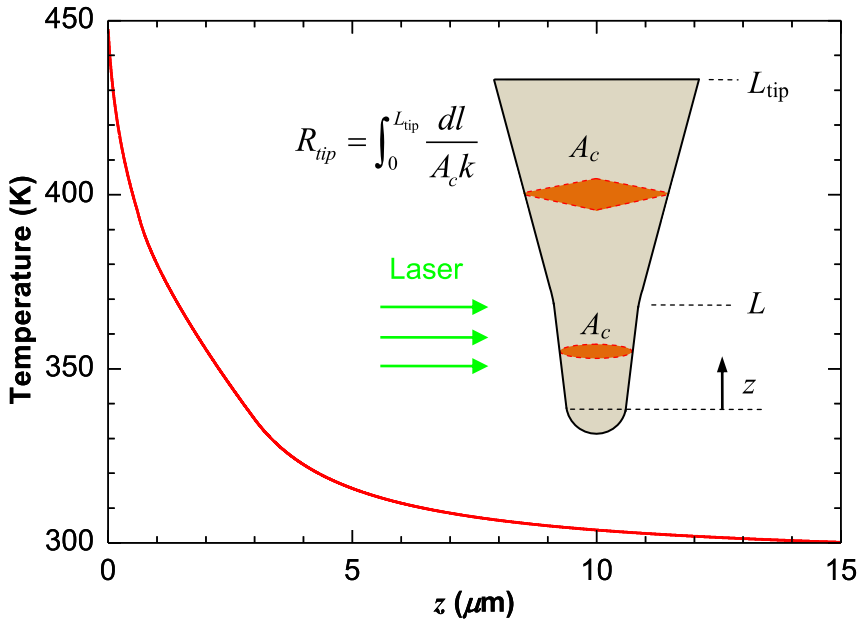

Figure 4.9 Steady state temperature distribution along tip axis. 2.8 μm at the tip apex is irradiated by laser with the intensity of 5.6 × 10^8 W/m^2.

4.5 Conclusion

In this work, the temperature rise of Si AFM tip is measured by Raman shift method. The temperature is calibrated with an anharmonic model involving with three- and four-phonon process. Due to the small dimension of the laser spot and AFM tip, the focus will affect the result significantly during the experiment. Despite the interaction between tip and laser cannot be observed directly, the diffraction image of the tip under laser illumination can be used to monitor the focusing situation. When the tip is moves upward closer to the focusing spot, the Raman shift decreases and the temperature increases; analogously, when the tip moves upward away from the focusing spot, the Raman shift increases, and the temperature decreases. Nevertheless, the Raman intensity increases during the whole process. When the laser moves along the tip axis from tip apex to cantilever, the temperature increases first, then decreases. The highest temperature is as high as 924 K. The incident laser intensity also affects the heating condition. Under stronger laser irradiation, the Raman signal intensity is stronger, the Raman shift trends to be less, and the temperature increases.

In order to investigate the heating mechanism of the near-field heating, the electric field distribution around the tip as well as inside the tip was calculated by finite element method. The highest field enhancement is 5.19 under the tip apex. And the highest field enhancement is 2.86 inside the tip. Due to the absorption of the laser, the temperature of the tip will rise. A one-dimensional heat transfer model is used to calculate the temperature along the tip axis. The highest temperature is 426 K at the hemisphere apex, while the measure temperature is approximately 600 K. Our first-order thermal analysis agrees well with the measurement

results if considering the dopants in the tip will reduce the thermal conductivity to some extent.

CHAPTER 5. CONCLUSIONS

5.1 Summary and Conclusions

The photothermal technique was used to measure the thermal properties of microscale. The samples were in the form of thin film. The thickness of the film can be from several micrometers to several millimeters. The samples we measured in chapter 2 are highly aligned nanorods array. The thermal properties measured by photothermal method are the average value within the spot size (0.7 mm × 1.4 mm). When the film thickness decreases further to the order of nanometers, the large scale (the order of millimeter) averaged properties cannot give us the local information, in other words, the large scale properties is not valid for nanostructures. Consequently, the thermal properties of nanostructures are out of the reach of the photothermal method. That is why we proposed the SPTM.

In the SPTM technology, near-field nanoscale surface heating will be very important for nanoscale structural defect characterization. The local optical field enhancement can be obviously increased if surface plasmons are generated, which is easy to occur with silver, gold or copper. Correspondingly, the greatest enhancements are observed in the nanostructures made from these materials [29]. It has been widely documented that AFM tips coated with a metal will feature much stronger enhanced optical field. Therefore, the AFM tips used in our experiment will be coated with Au to improve the enhanced optical field. According to the finite element simulation, the field enhancement is over 200 in the gap between tip and in the Si substrate the field enhancement is also over 150 in the silicon substrate when the laser irradiates the Au coated Si tip [51]. In chapter 3, extensive numerical

modeling has been conducted to study the enhanced optical field in the AFM tip-substrate system, and the relationship between the laser polarization direction, geometry (cone angle, apex radius) and enhanced optical field. It was found that AFM tip of small cone angle (though the enhancement is not maximized) and small tip radius is favorable for generating a more focused optical field.

Experimental work shows that when the laser with power 5.6×10^8 W/m^2 illuminates the apex of Si AFM tip, the temperature is as high as 600 K (300 K temperature rise). However, when the laser spot moves along the tip axis to the blunt end, the temperature first increases, then decreases. The highest temperature appears approximately in the middle part other than at the apex. Since the laser spot width along the tip axis is approximately 2.8 μm, it only cover a small portion of the tip along the tip axis direction. It can be referred that, with larger laser spot or higher laser power, higher temperature would be induced at the tip apex. Up to 1400 K has been observed in Si tip apex by tuning up the incident laser power, and the hot tip can be used as nanoscale knife to cut CNTs [127].

5.2 Establishing the SPTM System

When the tip-substrate system is irradiated by laser, the tip apex as well as the spot on the substrate normally under the tip will be heated up. Then heat transfer in the substrate and the tip, as shown in Figure 5.1. There is a large thermal contact resistance between the tip apex and the substrate surface, as analyzed in chapter 3. Such thermal contact resistance significantly slows down the heat transfer between the substrate and the AFM tip. Consequently, the heat is transferred away from the tip-substrate interface on both sides, and

heat transfer will consist of two parts: heat transfer in the sub-surface region of the substrate, and heat transfer in the AFM tip.

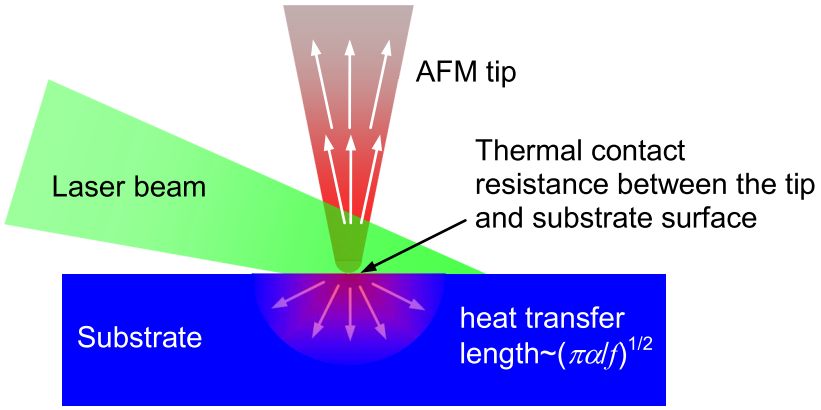

Figure 5.1 Schematic showing the heat transfer in the sample and the tip. There is a big thermal contact resistance between the tip apex and the substrate surface. Such thermal contact resistance significantly slows down the heat transfer between the substrate and the AFM tip.

For the substrate, only a small area (< 10 nm) of the sample will be heated. The characteristic size of the heat-affected zone will be about $(\pi\alpha/f)^{1/2}$, where f is the laser modulation frequency, and α is the local thermal diffusivity (as shown in Figure 5.1). This feature size usually is much larger than the laser heating spot. For instance, even for low thermal conductivity materials with ~10^{-7} m^2/s, for a modulation frequency of 100 kHz, the feature size of heat transfer is about 1 μm, which is much larger than the laser heating spot. Such typical heat transfer length makes the continuum approach still applicable for predicting the local heat transfer.

Figure 5.2 shows the schematic design of the SPTM techonology. The technology itself

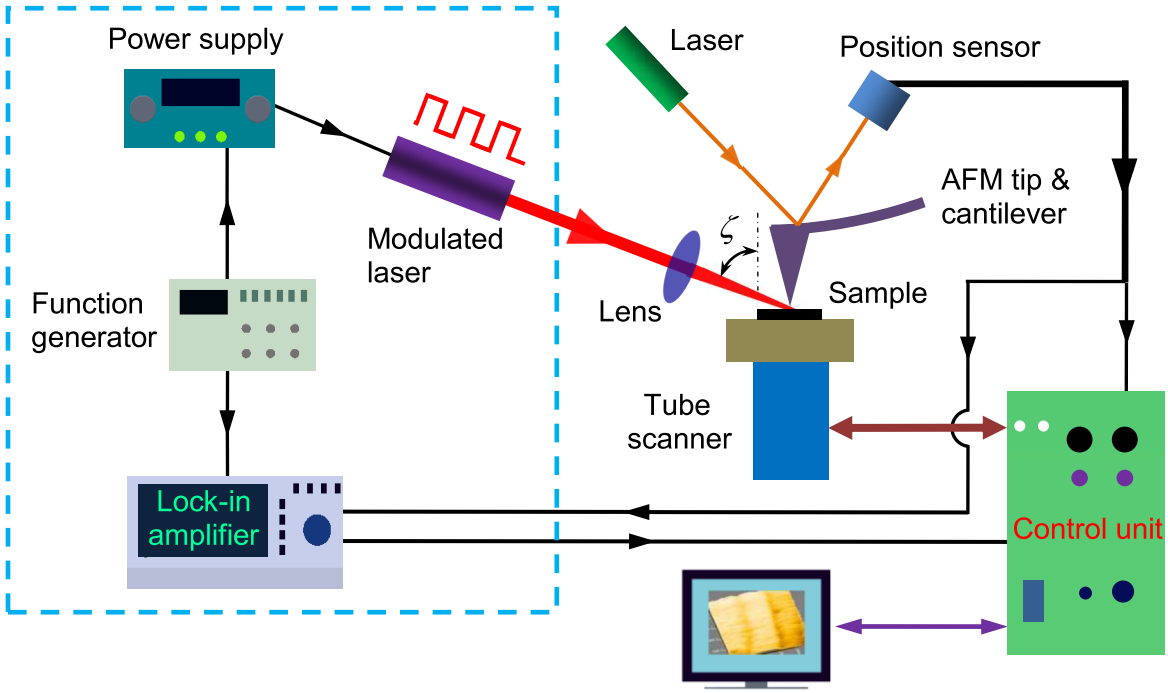

Figure 5.2 Schematic of the experimental setup for the SPTM system. The right-hand side is a conventional SPM system. The left-hand side (encircled by dashed line) is the optical delivery and phase-shift calculation sub-system. The deflection signal is extracted to the lock-in amplifier, referring to the signal from the function generator, phase shift is calculated in the lock-in amplifier, then input into the SPM control unit to generate the phase contrast figures. The incident laser with wavelength of 532 nm is incident at a large incident angle ζ to filter the laser direction heating of the sample as well as to gain stronger optical field under the tip apex.

mainly consists of two sub-systems: 1) optical delivery sub-system for surface nanoscale heating and 2) optical sensing sub-system to measure the periodically varying surface displacement. In the optical delivery sub-system, a special linearly polarized diode laser (wavelength: 532 nm) will be used as the exciting source. The laser beam will be focused to the AFM tip while keeping the laser beam as parallel as possible to the sample surface. The incident angle ζ of the laser beam will be adjusted to between 70 – 90°, to make sure that the

laser beam will not be blocked by the sample as well as gain stronger optical field. This is intended to eliminate the unnecessary heating of the sample by the non-focused laser beam. The laser beam will be modulated to be a square wave by directly connecting the synchronization signal from the function generator to the laser power supply. The laser modulation frequency can be varied from 10 Hz to 100 kHz to achieve depth profiling for sub-surface defect characterization.

In the optical sensing sub-system, upon near-field laser heating, the sample surface will have a periodically varying displacement, which will be sensed by the AFM tip in the contact mode. The AFM tip is scanning in constant-height method, that means the feedback is shut off, and the piezo tube scanner will not move in the *z*-direction during the scanning. The deflection signal (normal force) — the output of the position sensor will be branched to a lock-in amplifier, which is used to measure the amplitude as well as phase shift of the surface displacement. The amplitude in the lock-in amplifier can be used as a reference for laser focusing under the modulated laser mode. However, for continuous external laser, the laser (built-in laser of SPM) spot in position sensor can be referred. The phase shift is calculated while referring to the signal from the function generator. After calculation, the phase shift signal of the lock-in amplifier is input into the SPM controller, then to computer together with the deflection, lateral force, and feedback signals (although the feedback is not transmitted to the piezo tube scanner, it can be used to generate figures in computer). It is expected that a phase contrast figure, which will reflect the thermal diffusivity of the local sample will be engendered from the phase shift signal, akin to the phase contrast reported in s-SNOM [46,180-185], in which the phase shift between the incident laser and the elastically

reflected scattered light is calculated. Other similar design which including a piezoelectric transducer glued to tube scanner, was proposed [186,187]. When the transducer is excited by external signal, phase image can be engendered with the deflection signal.

In operation of SPTM introduced above, the AFM is under constant-height mode, no feedback is transmitted to the piezo scanner, which only scans in *x*- and *y*- direction. However, the constant force mode can also be operated in the SPTM system when the external laser is continuous. Scanning the same surface or line twice with the external laser on or off, comparing the two figures, the difference between them can reflect the different thermal expansion due to near-field heating of the sample.

In our experiment, the entire sample chamber of the SPM (MicroNano D3000 SPM) will be filled with helium or argon gas. This ambient gas environment will prevent local oxidation at the region under the AFM tip and reduce the moisture level on the sample surface, thereby reducing the effect of water bridge between the sample and the AFM tip.

5.3 Contributions and Recommendations for Future Work

The theoretical and experimental work on temperature rise of AFM tip under laser illumination provides insight for the tip-laser interaction. The thermal expansion of the tip can be calculated correspondingly. According to the tip-enhanced Raman scattering experiment [51], the thermal expansion of the Si substrate can also be estimated as following. Over 200 K temperature rise has been observed in a sub-10nm scale on Si substrate under the laser illuminated tip, with 785 nm incident laser at a power of 1.2×10^7 W/m^2. With the

thermal expansion of 2.6×10^{-6} K^{-1}, the thermal expansion or surface rise of surface would be 0.5 nm, if the feature size of heat transfer is about 1 μm is used. This is an ideal situation. In fact, only a 10 nm scale can be heated as high as 200 K. The temperature outside this range would be dropped quickly. As a result, the thermal expansion would be reduced correspondingly. However, if the higher incident laser power is used, saying, 5.6×10^{8} W/m^2 at 532 nm (the same with the experimental conditions in chapter 4), according to the simulation, the field enhancement will not change much if the wavelength changes from 785 nm to 532 nm. The absorption rate also will reduce less than 10%, however, the power increase is 47 times. It is expected that the temperature rise of the substrate will be larger more than 200 K or the scale of the heated area will be larger. And the thermal expansion will larger. If lower thermal conductivity material like SiO_2 is used, extremely high temperature can be acquired, which in turn will induce larger thermal expansion to some extent. Once the discrepancies of thermal expansion is larger than several nanometers from spot to spot, is can be detected by the AFM.

REFERENCES

[1] Tanaka N, Susa M and Nagata K 1991 *Materials Transaction, JIM* **32** 429-37

[2] Guo J, Wang X and Wang T 2007 *J. Appl. Phys.* **101** 063537-1-7

[3] Yue Y, Eres G, Wang X and Guo L 2009 *Appl. Phys. A* **97** 19-23

[4] Wang X, Hu H and Xu X 2001 *J. Heat Transfer* **123** 138-44

[5] Hu H, Wang X and Xu X 1999 *J. Appl. Phys.* **86** 3953-8

[6] Almond D P and Patel P M 1996 *Photothermal Science and Techniques* 1st ed. (London: Chapman & Hall)

[7] Haji-Sheikh A, Hong Y S, You S M and Beck J V 1998 *J. Heat Transfer* **120** 568-76

[8] Kemp T, Srinivas T A S, Fettig R and Ruppel W 1995 *Rev. Sci. Instrum.* **66** 176-81

[9] Pessoa O J, Cesar C L, Patel N A, Vargas H, Ghizoni C C and Miranda L C M 1986 *J. Appl. Phys.* **59** 1316-18

[10] Rosencwaig A and Gersho A 1976 *J. Appl. Phys.* **47** 64-9

[11] Rosencwaig A 1978 *J. Appl. Phys.* **49** 2905-10

[12] Yu X Y, Zhang L and Chen G 1996 *Rev. Sci. Instrum.* **67** 2312-6

[13] Wang X, Zhong Z and Xu J 2005 *J. Appl. Phys.* **97** 064302

[14] Xu Y, Zhang Y, Suhir E and Wang X 2006 *J. Appl. Phys.* **100** 074302

[15] Guo L, Wang J, Lin Z, Gacek S and Wang X 2009 *J. Appl. Phys.* **106** 123526

[16] Wang T, Wang X, Zhang Y, Liu L, Xu L, Liu Y, Zhang L, Luo Z and Cen K 2008 *J. Appl. Phys.* **104** 013528

[17] Binnig G and Rohrer H 1982 *Helv. Phys. Acta* **55** 726-735

[18] Lewis A, Isaacson M, Harootunian A and Murry A 1984 *Ultramicroscopy* **13** 227-31

[19] Pohl D W, Denk W and Lanz M 1984 *Appl. Phys. Lett.* **44** 651-3

[20] Sánchez E, Novotny L and Xie X S 1999 *Phys. Rev. Lett.* **82** 4014-7

[21] Zenhausern F, Martin Y and Wickramasinghe H K 1995 *Science* **269** 1083-5

[22] Zse S M 1981 *Physics of Semiconductor Devices* (New York: Wiley)

[23] Kawata S and Inouye Y 1995 *Ultramicroscopy* **57** 313-7

[24] Esteban R, Vogelgesang R and Kern K 2009 *Opt. Express* **17** 2518-29

[25] Fleischmann M, Hendra P J and McQuillan A J 1974 *Chem. Physi. Lett.* **26** 163-6

[26] Jeanmaire D L and Duyne R P van 1977 *J. Electroanal. Chem.* **84** 1-20

[27] Campion A and Kambhampati P 1998 *Chem. Soci. rev.* **27** 241-50

[28] Kneipp K 2007 *Phys. Today* **60** 40-6

[29] Anderson M S 2000 *Appl. Phys. Lett.* **76** 3130-2

[30] Bailo E and Deckert V 2008 *Chem. Soci. rev.* **37** 921-30

[31] Downes A, Salter D and Elfick A 2006 *J. Phys. Chem. B* **110** 6692-8

[32] Geshev P I, Fischer U and Fuchs H 2010 *Phys. Rev. B* **81** 125441-1-16

[33] Hallen H D, La Rosa A H and Jahncke C L 1995 *Phys. Status Solidi a* **152** 257-68

[34] Jahncke C L, Paesler M A and Hallen H D 1995 *Appl. Phys. Lett.* **67** 2483-5

[35] Zeisel D, Deckert V, Zenobi R and Vo-dinh T 1998 *Chem. Physi. Lett.* **283** 381-5

[36] Martin O J F and Girard C 1997 *Appl. Phys. Lett.* **70** 705-7

[37] Novotny L, Bian R X and Xie X S 1997 *Phys. Rev. Lett.* **79** 645-8

[38] Novotny L, Sánchez E J and Xie X S 1998 *Ultramicroscopy* **71** 21-9

[39] Gorbunov A A and Pompe W 1994 *Phys. Status Solidi a* **145** 333-8

[40] Policar C, Waern J B, Plamont M-A, Clède S, Mayet C, Prazeres R, Ortega J-M, Vessières A and Dazzi A 2011 *Angewandte Chemie (International ed. in English)* **50** 860-4

[41] Mayet C, Dazzi A, Prazeres R, Ortega J-M and Jaillard D 2010 *The Analyst* **135** 2540-5

[42] Prater C, Kjoller K, Cook D, Shetty R, Meyers G, Reinhardt C and Felts J 2010 *Microscopy and Analysis* **24** 5-8

[43] Knoll B and Keilmann F 1999 *Nature* **399** 7-10

[44] Hillenbrand R, Knoll B and Keilmann F 2001 *J. microscopy* **202** 77-83

[45] Ocelic N and Hillenbrand R 2004 *Nature materials* **3** 606-9

[46] Brehm M, Taubner T, Hillenbrand R and Keilmann F 2006 *Nano letters* **6** 1307-10

[47] Williams C C and Wickramasinghe H K 1986 *Appl. Phys. Lett.* **10598** 1587-9

[48] Oesterschulze E, Stopka M and Kassing R 1994 *Microelectron. Eng.* **24** 107-12

[49] Oesterschulze E, Stopka M, Ackermann L, Scholz W and Werner S 1996 *J. Vac. Sci. Technol. B* **14** 832-7

[50] Oesterschulze E and Stopka M 1996 *J. Vac. Sci. Technol. A* **14** 1172-7

[51] Yue Y, Chen X and Wang X 2011 *ACS Nano* **5** 4466–4475

[52] Hahnet E and Kallweit J 1998 *Int. J. Hydrog. Energy* **23** 107-14

[53] Trudeau M L 1999 *MRS Bulletin* **24** 23-6

[54] Sakintuna B, Lamaridarkrim F and Hirscher M 2007 *Int. J. Hydrog. Energy* **32** 1121-40

[55] Kelkar T, Kanhere D and Pal S 2008 *Comp. Mat. Sci.* **42** 510-6

[56] Kelekar R, Giffard H, Kelly S T and Clemens B M 2007 *J. Appl. Phys.* **101** 114311

[57] Pozzo M and Alfè D 2009 *Int. J. Hydrog. Energy* **34** 1922-30

[58] Huot J 1999 *J. Alloys Compounds* **293-295** 495-500

[59] Zaluska A, Zaluski L and Ström-Olsen J O 2001 *Appl. Phys. A* **72** 157-65

[60] Shang C X, Bououdina M, Song Y and Guo Z X 2004 *Int. J. Hydrog. Energy* **29** 73-80

[61] Song Y, Guo Z and Yang R 2004 *phys. Rev. B* **69** 094205

[62] Song Y, Zhang W and Yang R 2009 *Int. J. Hydrog. Energy* **34** 1389-98

[63] Tsuda M, Dino W, Kasai H, Nakanishi H and Aikawa H 2006 *Thin Solid Films* **509** 157-9

[64] Liang G 2004 *J. Alloys Compounds* **370** 123-8

[65] Liang G, Huot J, Boily S, Van Neste A and Schulz R 1999 *J. Alloys Compounds* **292** 247-52

[66] Schulz R, Liang G and Huot J 2001 A R Dinesen, editors. *Proc. 22nd Risø int. symp. on material science* (Roskilde, Denmark: Risø National Laboratory) p 141-53

[67] Bobet J, Aymonier C, Mesguich D, Cansell F, Asano K and Akiba E 2007 *J. Alloys Compounds* **429** 250-4

[68] Schmidt H, Jonschker G, Goedicke S and Mennig M 2000 *J. Sol-Gel Sci. Technol.* **19** 39-51

[69] Léon A, Knystautas E, Huot J, Lorusso S, Koch C and Schulz R 2003 *J. Alloys Compounds* **356-357** 530-5

[70] Gedanken A 2007 *Ultrason. sonochem.* **14** 418-30

[71] Zhitomirsky I 2006 *J. Mater. Sci.* **41** 8186-95

[72] Wang Y, Sasaki M, Goto T and Hirai T 1990 *J. Mater. Sci.* **25** 4607-13

[73] Armelao L, Barreca D, Bottaro G, Gasparotto A, Gross S, Maragno C and Tondello E 2006 *Coordi. Chem. Rev.* **250** 1294-314

[74] He Y, Zhao Y and Wu J 2008 *Appl. Phys. Lett.* **92** 063107

[75] He Y, Zhao Y, Huang L, Wang H and Composto R J 2008 *Appl. Phys. Lett.* **93** 163114

[76] He Y and Zhao Y 2009 *Phys. Chem. Chem. Phys.* **11** 255-8

[77] He Y and Zhao Y 2009 *Nanotechnology* **20** 204008

[78] Kapischke J 1998 *Exp. Therm. Fluid Sci.* **17** 347-55

[79] Groll M 1993 *J. Heat Recovery Syst. CHP* **13** 341-6

[80] Kapischke J and Hapke J 1994 *Exp. Therm. Fluid Sci.* **9** 337-44

[81] Førde T, Næss E and Yartys V a 2009 *Int. J. Hydrog. Energy* **34** 5121-30

[82] Griesinger A, Spindler K and Hahne E 1999 *Int. J. Heat Mass Transfer* **42** 4363-74

[83] Sun D-W and Deng S-J 1990 *Int. J. Hydrog. Energy* **15** 331-6

[84] Nakagawa T, Inomata A, Aoki H and Miura T 2000 *Int. J. Hydrog. Energy* **25** 339-50

[85] Asakuma Y, Miyauchi S, Yamamoto T, Aoki H and Miura T 2004 *Int. J. Hydrog. Energy* **29** 209-16

[86] Anlage S M, Talanove V V and Schwartz A R 2007 Kalinin S V, Gruverman A, editors. *Scanning Probe Microscopy: Electrical and Electromechanical Phenomena at the Nanoscale* (New York: Springer-Verlag) p 215-253

[87] Born M and Wolf E 1999 *Principles of Optics: Electromagnetic theory of propagation, interference and diffraction of light* 7th ed. (Cambridge, UK: Cambridge University Press)

[88] Martin O J F and Paulus M 2002 *J. microsc.* **205** 147 -52

[89] Lu Y-F, Mai Z-H and Chim W-K 1999 *Jpn. J. Appl. Phys.* **38** 5910-5

[90] Demming F, Jersch J, Dickmann K and Geshev P I 1998 *Appl. Phys. B* **66** 593-8

[91] Martin O J F, Girard C and Dereux A 1995 *Phys. Rev. Lett.* **74** 526-9

[92] Martin Y C, Hamann H F and Wickramasinghe H K 2001 *J. Appl. Phys.* **89** 5774-8

[93] Krug II J T, Sánchez E J and Xie X S 2002 *J. Chem. Phys.* **116** 10895-901

[94] Chimmalgi A, Choi T and Grigoropoulos C P 2002 *ASME Int. Mechanical Engineering Congr. & Exposition* (New Orleans, LA: p 1-5

[95] Chimmalgi A, Grigoropoulos C P and Komvopoulos K 2005 *J. Appl. Phys.* **97** 104319-1-12

[96] Downes A, Salter D and Elfick A 2006 *Opt. Express* **14** 5216-22

[97] Wang Z B, Luk'yanchuk B S, Li L, Crouse P L, Liu Z, Dearden G and Watkins K G 2007 *Appl. Phys. A* **89** 363-8

[98] Sajanlal P R, Subramaniam C, Sasanpour P, Rashidianbc B and Pradeep T 2010 *J. Matter. Chem.* **20** 2108-13

[99] Gerstner V, Thon A and Pfeiffer W 2000 *J. Appl. Phys.* **87** 2574-80

[100] Jin J M 2002 *The Finite Element Method in Electromagnetics* 2nd ed. (New York: Wiley-IEEE Press)

[101] Micic M, Klymyshyn N, Suh Y D and Lu H P 2003 *J. Phys. Chem. B* **107** 1574-84

[102] Shi J, Lu Y, Cherukuri R S, Mendu K K, Doerr D W, Alexander D R, Li L P and Chen X Y 2004 *Appl. Phys. Lett.* **85** 1009-11

[103] Royer P, Barchiesi D, Lerondel G and Bachelot R 2004 *Phil. Trans. R. Soc. A* **362** 821-42

[104] Zhang W, Cui X and Martin O J F 2009 *J. Raman Spectrosc.* **40** 1338-42

[105] Brown R J C, Wang J and Milton M J T 2007 *Journal of Nanomaterials* **2007** 12086-96

[106] Khoury C G, Norton S J and Vo-dinh T 2009 *ACS Nano* **3** 2776-88

[107] Kurpas V V, Libenson M N and Martsinovsky G A 1995 *Proc. SPIE* **2384** 128-35

[108] Kavaldjiev D I, Toledo-Crow R and Vaez-Iravani M 1995 *Appl. Phys. Lett.* **67** 2771-2773

[109] La Rosa A H, Yakobson B I and Hallen H D 1995 *Appl. Phys. Lett.* **67** 2597-9

[110] Lienau C, Richter A and Elsaesser T 1996 *Appl. Phys. Lett.* **69** 325-7

[111] Stähelin M, Bopp M A, Tarrach G, Meixner A J and Zschokke-Gränacher I 1996 *Appl. Phys. Lett.* **68** 2603-5

[112] Zhang W, Schmid T, Yeo B-S and Zenobi R 2008 *J. Phys. Chem. C* **112** 2104-8

[113] Milner A A, Zhang K, Garmider V and Prior Y 2010 *Appl. Phys. A* **99** 1-8

[114] Mai Z H, Lu Y F, Song W D and Chim W K 2000 *Appl. Surf. Sci.* **154-155** 360-4

[115] Mamin H J and Rugar D 1992 *Appl. Phys. Lett.* **61** 1003-1005

[116] McCarthy B, Zhao Y, Grover R and Sarid D 2005 *Appl. Phys. Lett.* **86** 111914-1-3

[117] Hamann H F, Martin Y C and Wickramasinghe H K 2004 *Appl. Phys. Lett.* **84** 810-2

[118] Kavaldjiev D I, Toledo-Crow R and Vaez-Iravani M 1995 *Appl. Phys. Lett.* **67** 2771-3

[119] La Rosa A H, Yakobson B I and Hallen H D 1995 *Appl. Phys. Lett.* **67** 2597-9

[120] Yakobson B I, La Rosa A, Hallen H D and Paesler M A 1995 *Ultramicroscopy* **61** 179-85

[121] Kurpas V, Libenson M and Martsinovsky G 1995 *Ultramicroscopy* **61** 187-90

[122] La Rosa A H, Biehler B and Sinharay A 2002 *Proc. SPIE* **4777** 420-3

[123] Miskovsky N M, Park S H, Park H, He J and Cutler P H 1993 *J. Vac. Sci. Technol. B* **11** 366-70

[124] Ukraintsev V A and Yates Jr. J T 1996 *J. Appl. Phys.* **80** 2561-71

[125] Huber R, Koch M and Feldmann J 1998 *Appl. Phys. Lett.* **73** 2521-3

[126] Boneberg J, Münzer H-J, Tresp M, Ochmann M and Leiderer P 1998 *Appl. Phys. A* **67** 381-4

[127] Tarun A, Hayazawa N and Kawata S 2010 *Jpn. J. Appl. Phys.* **49** 025003-1-4

[128] Nelson B and King W 2008 *Nanoscale and Microscale Thermophysical Engineering* **12** 98-115

[129] Duvigneau J, Schönherr H and Vancso G J 2010 *ACS Nano* **4** 6932-40

[130] Depasse F, Gomès S, Trannoy N and Grossel P 1997 *J. Phys. D: Appl. Phys.* **30** 3279-85

[131] Grafström S, Kowalski J, Numann R, Probst O and Wörtge M 1991 *J. Vac. Sci. technol. B* **9** 568-72

[132] Grafström S, Schuller P, Kowalski J and Neumann R 1998 *J. Appl. Phys.* **83** 3453-60

[133] Geshev P I, Demming F, Jersch J and Dickmann K 2000 *Appl. Phys. B* **70** 91-7

[134] Geshev P I, Demming F, Jersch J and Dickmann K 2000 *Thin Solid Films* **368** 156-62

[135] Geshev P I, Klein S and Dickmann K 2003 *Appl. Phys. B* **76** 313-7

[136] Probst O and Wörtge M, with R Numann 1991 *J. Vac. Sci. Technol. B* **9** 568-72

[137] Neumann R, with J. Kowalski 1998 *J. Appl. Phys.* **83** 3453-60

[138] Jersch J, Demming F, Fedotov I and Dickmann K 1999 *Appl. Phys. A* **68** 637-41

[139] Lyubinetsky I, Dohnálek Z, Ukraintsev V a and Yates J T 1997 *J. Appl. Phys.* **82** 4115-7

[140] Milner A A, Zhang K, Garmider V and Prior Y 2010 *Appl. Phys. A* **99** 1-8

[141] He Y, Zhang Z, Hoffmann C and Zhao Y 2008 *Adv. Funct. Mater.* **18** 1676-84

[142] He Y P and Zhao Y P 2009 *J. Alloys Compounds* **482** 173-86

[143] Weaver J G and Frederikse H P R 2007 Lide D R, editor. *CRC Handbook of Chemistry and Physics* (Boca Raton, FL: Taylor and Francis) p 116-40 Section 12

[144] Stapβburger K 1992 *Ph. D. Thesis* University of Essen, Germany

[145] Kallweit J 1994 *Ph.D. Thesis* University of Stuttgart, Germany

[146] Suissa E, Jacob I and Hadari Z 1984 *J. Less-Common Met.* **104** 287-95

[147] Klemens P G 1969 Tye R P, editor. *Thermal Conductivity vol 1* (London: Academic) p 173

[148] Maxwell J C 1873 *Electricity and Magnetism* (Oxford: Clarendon)

[149] Tsuchiya B, Nagata S, Shikama T, Konashi K and Yamawaki M 2003 *J. Alloys Compounds* **356/357** 223-6

[150] Roth R M, Panoiu N C, Adams M M, Osgood Jr. R M, Neacsu C C and Raschke M B 2006 *Opt. Express* **14** 2921-31

[151] Zayats A V 1999 *Opt. Commun.* **161** 156-62

[152] Madrazo A, Nieto-Vesperinas M and García N 1996 *Phys. Rev. B* **53** 3654-7

[153] Lu Y F, Luk'yanchuk B S, Song W D and Chong T C, with M.H. Hong 2002 *J. Appl. Phys.* **91** 3268-74

[154] Kirsanov a, Kiselev A, Stepanov A and Polushkin N 2003 *J. Appl. Phys.* **94** 6822

[155] Fox M 2006 *Quantum Optics: An Introduction* (London, UK: Oxford University Press)

[156] Boneberg J, Münzer H-J, Tresp M, Ochmann M and Leiderer P 1998 *Appl. Phys. A* **67** 381-4

[157] Hsu I-K, Kumar R, Bushmaker A, Cronin S B, Pettes M T, Shi L, Brintlinger T, Fuhrer M S and Cumings J 2008 *Appl. Phys. Lett.* **92** 063119-1-3

[158] Ioffe Z, Shamai T, Ophir A, Noy G, Yutsis I, Kfir K, Cheshnovsky O and Selzer Y 2008 *Nat. nanotechnol.* **3** 727-32

[159] Soini M, Zardo I, Uccelli E, Funk S, Koblmüller G, Fontcuberta i Morral A and Abstreiter G 2010 *Applied Physics Letters* **97** 263107

[160] Piscanec S, Cantoro M, Ferrari A, Zapien J, Lifshitz Y, Lee S, Hofmann S and Robertson J 2003 *Physical Review B* **68** 241312-1-4

[161] Su Z, Sha J, Pan G, Liu J, Yang D, Dickinson C and Zhou W 2006 *J. Phys. Chem. B* **110** 1229-34

[162] Khachadorian S, Scheel H, Colli A, Vierck A and Thomsen C 2010 *Phys. Status Solidi B* **247** 3084-8

[163] Niu J, Sha J and Yang D 2006 *Scripta Materialia* **55** 183-186

[164] Burke H H and Herman I P 1993 *Phys. Rev. B* **48** 16-24

[165] Hart T R, Aggarwal R L and Lax B 1970 *Phys. Rev. B* **1** 638-42

[166] Zhang S-L, Ding W, Yan Y, Qu J, Li B, Li L-yu, Yue K T and Yu D 2002 *Appl. Phys. Lett.* **81** 4446-8

[167] Balkanski M, Wallis R F and Haro E 1983 *Phys. Rev. B* **28** 1928-34

[168] Konstantinović M, Bersier S, Wang X, Hayne M, Lievens P, Silverans R and Moshchalkov V 2002 *Phys. Rev. B* **66** 161311-1-4

[169] Tsu R 1982 *Appl. Phys. Lett.* **41** 1016-8

[170] Doerk G, Carraro C and Maboudian R 2009 *Phys. Rev. B* **80** 1-4

[171] Menendez J, Cardona M, Festkorperforschung M P-nck I-titut and I H 1984 *Phys. Rev. B* **29** 2051-9

[172] Ju Y S 2005 *Appl. Phys. Lett.* **87** 153106

[173] Chen G 1998 *Phys. Rev. B* **57** 14958-73

[174] Incropera F P, Dewitt, David P, Bergman T L and Lavine A S 2006 *Fundamentals of Heat and mass Transfer* 6th ed. John Wiley & Sons)

[175] Goodson K E and Cooper P T 1995 Buckius R, editor. *Proc. of the Symposium on Thermal Science and Engineering in Honor of Chancellor Chang-Lin Tien* (Berkeley, California: p 153-9

[176] Asheghi M, Touzelbaev M N, Goodson K E, Leung Y K and Wong S S 1998 *J. Heat Transfer* **120** 30-6

[177] Asheghi M, Kurabayashi K, Kasnavi R and Goodson K E 2002 *J. Appl. Phys.* **91** 5079-88

[178] Liu W and Asheghi M 2005 *J. Appl. Phys.* **98** 123523-1-6

[179] Burzo M G, Komarov P L and Raad P E 2004 *5th Intl. Conf. on Thermal and Mechanical Simulation and Experiments in Microelectronics and Microsystems, EuroSimE 2004* Ieee) p 269-76

[180] Hillenbrand R 2004 *Ultramicroscopy* **100** 421-7

[181] Huber A, Ocelic N, Taubner T and Hillenbrand R 2006 *Nano Lett.* **6** 774-8

[182] Schnell M, Garcia-Etxarri A, Huber A J, Crozier K, Aizpurua J and Hillenbrand R 2009 *Nature photonics* **3** 287-91

[183] Schnell M, Garcia-Etxarri A, Huber A J, Crozier K B, Borisov A, Aizpurua J and Hillenbrand R 2010 *J. Phys. Chem. C* **114** 7341-5

[184] Taubner T, Keilmann F and Hillenbrand R 2004 *Nano Letters* **4** 1669-72

[185] Taubner T, Korobkin D, Urzhumov Y, Shvets G and Hillenbrand R 2006 *Science* **313** 1595

[186] Zeng H, Yu H, Hui S, Chu R, Li G, Luo H and Yin Q 2005 *Solid State Communications* **133** 521-5

[187] Liu X, Kitamura K, Terabe K, Zeng H and Yin Q 2007 *Appl. Phys. Lett.* **91** 232913-1-3

RELATED PUBLICATIONS

Xiangwen Chen, Xinwei Wang (**2011**). Near-field thermal transport in nanotip under laser irradiation. *Nanotechnology*, 22(7): pp.075204-1-11.

Yanan Yue, **Xiangwen Chen**, Xinwei Wang (**2011**). Non-Contact Sub-10 nm Temperature Measurement in Near-field Laser Heating. *ACS Nano*, 5(6): pp 4466-4475.

Xuhui Feng, **Xiangwen Chen**, Xinwei Wang (**2011**). Thermophysical properties of thin film composed of anatase TiO_2 nanofibers. *Acta Materialia*, 59: pp.1934-44.

Xiangwen Chen, Yuping He, Yiping Zhao, Xinwei Wang (**2010**). Thermophysical properties of hydrogenated vanadium-doped magnesium porous nanostructures. *Nanotechnology*, 21(5): pp.055707-1-8.

Xiangwen Chen, Xinwei Wang (**2010**) Near-field heating of nano-tips in laser-assisted SPM surface nanostructuring. *47th Annual Technical Meeting of SES*, Ames, IA, Oct. 2010.